Self-Gated Cardiac MRI for Free-Breathing Simultaneous Cine, T1 Map and LGE Acquisition

---

A

Dissertation

Presented to

the faculty of the School of Engineering and Applied Science

University of Virginia

---

in partial fulfillment

of the requirements for the degree

Doctor of Philosophy

by

Ruixi Zhou

May 2021

APPROVAL SHEET

This

Dissertation

is submitted in partial fulfillment of the requirements
for the degree of

Doctor of Philosophy

Author: Ruixi Zhou

This Dissertation has been read and approved by the examing committee:

Advisor: Michael Salerno

Advisor:

Committee Member: Craig H. Meyer

Committee Member: Frederick H. Epstein

Committee Member: John P. Mugler III

Committee Member: Christopher M. Kramer

Committee Member: Daniel S. Weller

Committee Member:

Accepted for the School of Engineering and Applied Science:

Craig H. Benson, School of Engineering and Applied Science

May 2021

Abstract

Heart failure (HF) is a major and growing public health problem in the United States. Currently, approximately six million Americans live with heart failure. Cardiac magnetic resonance (CMR) imaging provides important diagnostic and prognostic utility in HF. It has become the gold standard for accurately measuring left ventricular ejection fraction (LVEF) using cine imaging, and for characterizing myocardial scarring using late gadolinium enhancement (LGE) images. More recently developed parametric mapping techniques of myocardial native T1 and extracellular volume fraction (ECV) have further extended the unique diagnostic and prognostic information provided by CMR to characterize cardiomyopathy.

In a current clinical practice, a stack of 10-12 2D slices of short-axis cine images are typically acquired with breath-holding (BH) and electrocardiograph (ECG)-gating. In a separate set of acquisitions, T1 maps are typically acquired before and after contrast injection with a Modified Look-Locker-Inversion recovery (MOLLI) technique. MOLLI acquires single-shot images intermittently in diastole during 3 to 5 heartbeats after the inversion recovery (IR) pulses using breath-holding and ECG-gating. Alternatively, the SAturation-recovery single-SHot Acquisition (SASHA) sequence uses saturation recovery (SR) pulses. Ten minutes following contrast administration, a stack of 10-12 short-axis LGE images are acquired to characterize fibrosis. This approach to CMR image acquisition is inefficient and subject to artifacts related to poor ECG-gating and breath-hold. It also requires patient to complete 40+ breath-hold maneuvers during a 40+ minute acquisition. Recently advanced CMR techniques have been proposed to obtain multi-contrast cardiac imaging. Those methods either require ECG synchronization or breath-holds, or separate map for B1 correction. In this dissertation we propose to develop techniques to perform free-breathing (FB) cine, T1 mapping and LGE (post-contrast) imaging in

a single acquisition without the need of ECG synchronization, and validate the proposed techniques in phantoms, normal human subjects and clinical patients including the ones with cardiomyopathy.

Specific Aim #1 is to develop free-breathing cine imaging using spiral acquisition with respiratory correction and cardiac self-gating (SPARCS). (a) Develop an automatic heart detection algorithm and extract respiratory motion around the heart to perform motion correction (MC) on k-space data. (b) Design a continuously acquired golden-angle (GA = 137.51°) spiral pulse sequence and perform a cardiac self-gated and respiratory motion-corrected reconstruction. (c) Evaluate image quality and compare the quantification of LVEF as compared to standard breath-holding and ECG-gating balanced steady state free-precession (bSSFP) cine imaging.

Specific Aim #2 is to develop simultaneous acquisition of cine images, T1 maps and LGE images under free-breathing and cardiac self-gating (CAT-SPARCS). (a) Design a spiral pulse sequence with intermittent IR pulses and relaxation time to obtain cine and T1 maps in a single free-breathing acquisition. (b) Design a continuous IR-based spiral pulse sequence with two excitation flip angles to measure T1 while correcting for B1 effects and slice profile (CAT-SPARCS 2FAs). (c) Develop a free-breathing Bloch-Siegert B1 mapping acquisition and incorporate it to the continuous IR-based spiral acquisition pipeline with one excitation flip angle (1FA+B1).

Specific Aim #3 is to validate the CAT-SPARCS 2FAs and 1FA+B1 techniques in phantom, normal human subjects and clinical patients including the ones with cardiomyopathy. (a) Acquire data using CAT-SPARCS 2FAs and 1FA+B1, and the standard clinical-used T1 maps including MOLLI and SASHA results during experiments. (b) Validate the proposed T1 measurements as compared to MOLLI and SASHA results.

Acknowledgement

I had a wonderful and enriching experience studying at UVA over the past 5 years. Looking back all those great memories, I realized that it would not have been possible to write this dissertation without the help and support of the kind people around me, to only some of whom it is possible to give particular mention here.

I would like to express my sincere gratitude to my supervisor Dr. Michael Salerno, for providing me the honor to join in his lab. Dr. Salerno is one of the most energetic persons I have ever met. I still remember the first time that I met with Dr. Salerno during on-site interview in the spring of 2016, his mastery of knowledge and his passion for research really impressed me. During the past 5 years, he has guided me from learning basic knowledge of MRI and physiology to solving problems during research. When I met problems and stopped making progress on research projects, he always comforted me and taught me to start from the simplest case and eliminate every possible confounding factor step-by-step. Although he is very busy as both a PI and a full-time cardiologist, he is always willing to offer help in many aspects. His expertise, enthusiasm, kindness and reliability have influenced my attitude towards future research and life.

Dr. Craig Meyer deserves lots of gratitude for not only serving as my committee chair but also providing valuable guidance and comments during my PhD. He is a clear thinker and very knowledgeable about the field. I learned a lot from Dr. Meyer's critical thinking and attitude in research. I would also like to thank Dr. Daniel Weller for his massive help on my research. Dr. Weller attended almost every weekly lab meeting and provided considerable precious comments on my projects. His patient guidance and a wealth of knowledge about image reconstruction greatly helped me finish this dissertation. I'm also grateful for Dr. Frederick Epstein, whose invaluable comments helped me shape my research much better. He pointed out the importance of looking at

the research from a big picture and staying abreast of latest advances in the field. His wise insights and rich knowledge will always guide me on my research in the future. Next, I want to appreciate the help and support from Dr. John Mugler. He is well-informed about the field and always respond effectively when I asked him for help. I learnt a lot from his seriousness and enjoyment about scientific research. I would also like to acknowledge and thank Dr. Christopher Kramer for his significant suggestions from a clinical perspective, such as pointing out practical clinical needs and providing feedback of images as an experienced cardiologist. His efficient working skills inspired me to become a well-organized and productive researcher in the future.

I would like to thank the wonderful people in the Salerno lab. Special thanks go to the former member, Dr. Yang Yang, who has been guiding me and providing countless help during my PhD. His solid work in the lab inspired my research and played an irreplaceable role of this dissertation. I also want to acknowledge my amazing lab-mates and friends: Matthew Van Houten, Junyu Wang, Jonathan Pan, Xitong Wang and Niloufar Zakariaei, as well as Haris Jeelani from Dr. Weller's lab. Exchanging ideas and discussing problems with you guys have been an awesome experience. I'm extremely grateful for our clinical coordinators: Caroline Flournoy, Sara Prince and former member Jayne Missel. Without your help, I will never get all those human data presented in this dissertation. I also want to thank Joe Di Maria for helping me purchasing office supplies and providing expert advice on electronic products.

I want to express my gratitude to the fabulous MRI team at UVA. Both former and current advanced imaging fellows including Dr. Roshin Matthew, Dr. Austin Robinson, Dr. Christopher Schumann, Dr. Elona Rrapo Kaso, Dr. Christopher Hanson and Dr. Patricia Rodriguez Lozano, have helped me getting clinical data for my research. I also owe a debt of thanks to our research technician Jamie Weathersbee and Jose M. Reyes, as well as the whole clinical MRI team at UVA,

to help me finish my experiments. I would like to thank the big UVA MRI research group, including but not limited to Dr. Xue Feng, Dr. Steven Allen, Zhixing Wang, Quan Dou, Dr. Changyu Sun, for providing great suggestions and help about my research.

I would also like to thank Dr. Mathews Jacob's research group from University of Iowa. Collaboration with Dr. Mathews Jacob and Dr. Abdul Haseeb Ahmed have been a great experience and I really appreciate their valuable feedback and suggestions.

In additional to the people who gave me direct support in research, I want to express my appreciation to all the friends that I met in Charlottesville. Your consistently encouragement and support help me finish my study in the past 5 years and make it become an indispensable memory of my life.

Lastly, I would like to acknowledge my family, especially my parents, for their support and encouragement during my whole life. My dad is always willing to hear and provide feedback when I share my study and life with him, and my mom consistently cares about every aspect of me. I really appreciate being their only daughter.

Table of Contents

List of Figures

List of Tables

Chapter 1: Introduction

1.1 Heart failure and cardiomyopathy

Heart failure is a clinical condition characterized by shortness of breath, exercise intolerance, fluid retention, and fatigue that results from the heart's inability to pump enough blood to meet the body's oxygen requirements [1]. It remains a major cause of morbidity and mortality affecting 5.7 million patients in the US and is a contributing factor in 1 in 9 deaths [2]. The economic cost for heart failure is staggering and was approximately $30.7 billion in 2012 and is suggested to increase to $69.7 billion by 2030 [3].

This progressive and chronic condition can be caused by various structural or functional cardiac disorders [4]. Cardiomyopathy, which indicates 'the disease of heart muscle (myocardium)', is one of the most common causes of heart failure. Due to numerous factors, there are a number of different types of cardiomyopathy, such as dilated cardiomyopathy, hypertrophic cardiomyopathy, ischemic cardiomyopathy, etc. Therefore, determination of the underlying cause of a patient's heart failure syndrome by assessing the left ventricular ejection fraction (LVEF), tissue characterizations and myocardial scar, have important diagnostic, therapeutic, and prognostic implications.

1.2 Magnetic resonance imaging

Among the current available clinical techniques that used to visualize the heart, cardiac magnetic resonance (CMR) imaging is a widely used technique to provide important diagnostic and prognostic information in cardiac diseases. It stands out owing to its non-invasive, no-radiation, high signal-to-noise ratio (SNR) properties with multiple contrasts. The main advantage of CMR is that it cannot only quantify cardiac function but also perform tissue characterization. During one CMR study, a range of sequences that designate for specific indications will be scanned.

1.2.1 Cine imaging

Cardiac cine imaging is to generate a short movie that can capture the contraction and relaxation of the heart through the cardiac cycle. In clinical settings, cine images provide necessary dynamic information to study cardiac function, valvular function, wall motion and the blood flow through the heart. To quantify the cardiac function, a stack of 10-12 2D slices of short-axis cine images are typically acquired with breath-holding and ECG-gating. Doctors will then use the cine images to draw region of interest (ROI) on the left ventricle at end-diastolic and end-systolic frames for each slice. This is the gold-standard for accurately measuring LVEF [5]:

$$LVEF = \frac{SV}{EDV} = \frac{EDV - ESV}{EDV}, \tag{1.1}$$

where SV is stroke volume, EDV is end-diastolic volume and ESV is end-systolic volume. For example, an LVEF of 60% indicates that for each heartbeat 60% of total blood in the left ventricle is pumped out. Usually, an LVEF value ranges from 55% to 70% will be considered normal.

In practice, in order to fill the k-space with enough data at each frame (image), segmented data acquisition is usually used for cine imaging. It divides each cardiac cycle into the same number of segments (frames), and then combine the data in each segment across multiple cardiac cycles during one breath-hold acquisition.

1.2.2 T1 mapping

Quantitative myocardium longitudinal relaxation (T_1) mapping is a promising CMR technique that provides tissue characterization. Studies [6,7] have been shown that native T_1 mapping are useful to identify abnormalities in the myocardium. Moreover, native and post-contrast T_1 mapping can be performed to quantify extracellular volume (ECV) fraction:

$$ECV = (1 - hematocrit)\frac{\frac{1}{post-contrast\ myo\ T1} - \frac{1}{native\ myo\ T1}}{\frac{1}{post-contrast\ blood\ T1} - \frac{1}{native\ blood\ T1}}, \tag{1.2}$$

ECV can be measured in myocardium ROIs or visualized on ECV maps. It offers readers a quantitative physiological measurement of myocardial tissue remodeling, which further extends the unique diagnostic and prognostic information provided by CMR to characterize cardiomyopathy [8,9].

By using different acquisition strategies to sample the T_1 recovery signal, several T_1 mapping techniques have been proposed [10–12]. The fundamental idea for certain T_1 mapping approaches was come up by Look and Locker in the 1960s [10,13] (Figure 1.1). The idea is to sample multiple points with different inversion times (TIs) after an inversion recovery (IR) pulse along the T_1 recovery curve. This strategy greatly improves the acquisition efficiency in comparison to only sampling one point after each inversion pulse. However, in this case because the T_1 recovery signal have been disrupted by the intermittent RF pulses, this recovery has a shortened apparent T_1 time, which is named as T_1^*. The true T_1 can then be estimated by applying a correction factor in the low flip angle regime.

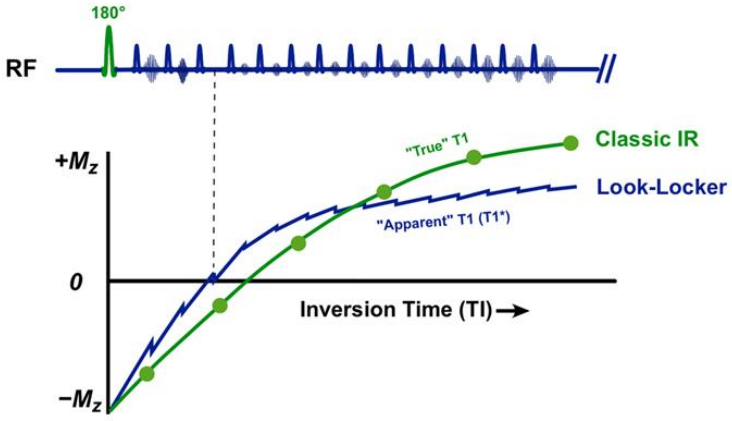

Figure 1.1 Look-Locker T_1 acquisition. (Adapted from http://mriquestions.com/t1-mapping.html)

To facilitate CMR T_1 mapping considering the movement of the heart, a Modified Look-Locker-Inversion recovery (MOLLI) [12] technique has been developed. By adopting electrocardiograph (ECG) to synchronize cardiac motion and using breath-holding instructions to constrain respiratory motion, MOLLI acquires multiple single-shot balanced steady-state free-

precession (bSSFP) images intermittently in diastole during 3 to 5 heartbeats after the inversion recovery pulses (Figure 1.2).

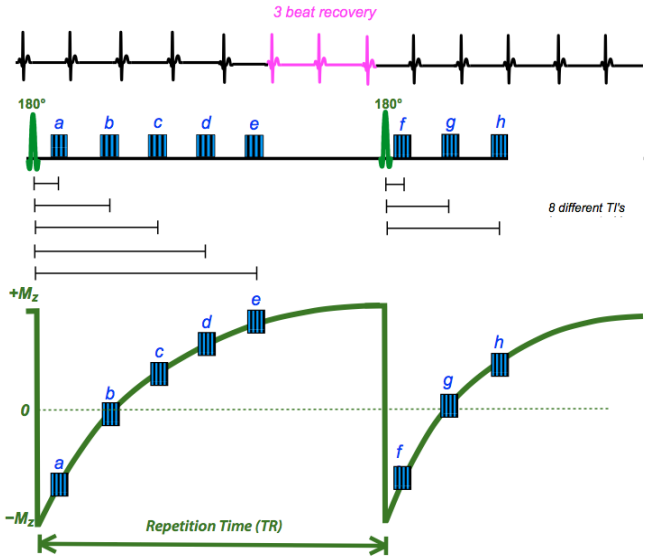

Figure 1.2 MOLLI T_1 acquisition. (Adapted from http://mriquestions.com/t1-mapping.html)

Alternatively, the SAturation-recovery single-SHot Acquisition (SASHA) [14] sequence contains ten single-shot bSSFP images in continuous heartbeats with ECG-gating and breath-holding (Figure 1.3). There is no magnetization preparation applied before the first image, while saturation recovery (SR) pulse is played out before the rest nine images with different SR times.

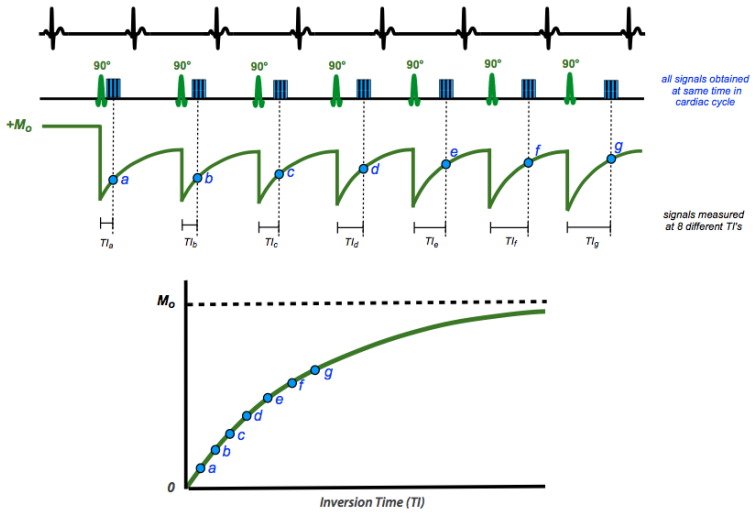

Figure 1.3 SASHA T_1 acquisition. (Adapted from http://mriquestions.com/t1-mapping.html)

1.2.3 Late-gadolinium enhancement imaging

Late-gadolinium enhancement (LGE) images are the gold-standard to identify myocardial scar and focal fibrosis for both ischemic [15] and non-ischemic cardiomyopathy [16]. Typically, 10 minutes after gadolinium contrast injection, LGE imaging will be performed followed by a TI scout. During the 10 minutes waiting time, gadolinium contrast agent will be rapidly washed out in normal myocardium. However, for regions of scar or fibrosis contrast agent will be trapped in the extracellular area, which leads to a shortened T_1. By choosing an optimal TI value that can null the healthy myocardium, scar or fibrosis regions will be differentiated because of the high signal intensity in the LGE images.

1.3 CMR in heart failure and cardiomyopathy

CMR is an important and useful tool over other imaging modalities due to the high resolution, high SNR, lack of radiation, and non-invasive nature with the flexibility of imaging any plane of the heart. Cine images can provide a complete cardiac cycle movie of the heart in different views. Visual inspection on the left and right ventricles, valves as well as wall motion allow doctors to identify cardiac functional abnormalities, such as valve regurgitation, pericardial thickness, etc. By using manual or automatic planimetry on a stack of short axis views covering the whole left ventricle, LVEF can be accurately measured and quantified. This can be used to categorize patients into different types, as heart failure with reduced left ventricular function (HFrEF) and heart failure with preserved left ventricular function (HFpEF), for further treatment considerations such as the use of implantable cardioverter-defibrillator [17].

Furthermore, as MRI exploits the magnetic properties of individual protons within the tissues in a specified magnetic field, CMR enables cardiac tissue characterization, which helps identify and differentiate different kinds of cardiomyopathies. For patients with severe renal

impairment who are not suitable to receive gadolinium-based contrast, pre-contrast quantitative mapping can provide the intrinsic or native tissue information. Myocardial T_1 varies with myocardial changes [18], such as edema, iron overload, protein infiltration, lipid deposition, etc. For example, studies [19–21] have shown an elevation in the native T_1 in amyloidosis comparing to controls and some other cardiac diseases. Moreover, for patients who have known coronary artery disease non-infarcted myocardial T_1 has important prognostic value [22]. When both pre- and post-contrast T_1 mappings are performed, ECV fraction can be calculated with decreased effect of confounding factors from both hardware and software with a measure of hematocrit. It is a more reliable measure of interstitial space across vendor platforms and field strengths. In terms of clinical utility, ECV changes in different direction between two phenotypically similar entities: decreased in athletic remodeling but increased in hypertrophic cardiomyopathy [18]. In addition, ECV is also useful to diagnose amyloid, where its elevations happen even without evidence of LGE [23].

Along with post-contrast quantitative mappings, LGE images, which are typically acquired 10 minutes after contrast injection, add additional significant diagnostic information regarding scarring of the myocardium. In terms of ischemic cardiomyopathy, multiple animal studies [24,25] have shown the presence of LGE in both acute and chronic myocardial infarction. LGE is not only able to identify the irreversible myocardial impairment, but also particularly show the transmural extent and the remaining viable myocardium [26]. Therefore, LGE is a valuable indicator of the extent of viability, which plays an important role for the planning and monitoring of therapies, such as the application of cardiac resynchronization therapy (CRT). In addition, LGE may also be present in non-ischemic cardiomyopathy, for instance, dilated cardiomyopathy or hypertrophic cardiomyopathy [26]. Although the presence of LGE in a coronary distribution can support the

diagnosis of coronary artery disease (CAD), the absence of LGE cannot exclude it [27]. Alternatively, cardiac first-pass stress perfusion imaging, which is acquired during contrast injection, can be an important tool to evaluate patients with known or suspected CAD [28,29].

1.4 K-space sampling

1.4.1 Cartesian sampling

Instead of capturing the original image as a camera does, magnetic resonance imaging acquires data in k-space, which consist of complex values representing spatial frequencies in the image. Each point (k_x, k_y, k_z) in k-space does not relate to individual voxel (x, y, z) in the image, but contains spatial frequency and phase information of the whole image. Typically, the center k-space regions correspond to low frequencies, which include the basic image contrast such as general structure and contours. The peripheries of k-space are responsible for high frequencies, where exist information about edges and details.

The classic way to sample the k-space is to acquire data line by line (from top to bottom, left to right), termed Cartesian sampling. There are several advantages using Cartesian sampling. Firstly, Cartesian sampling ensures that every acquired k-space point lie on a square (or rectangular) evenly spaced grid. Therefore, it's easy and efficient to transform data from k-space to image space just using 2D Fourier transform. Furthermore, when acquiring data at each line, the current hardware techniques allow the scanner to perform oversampling in the direction of the line without affecting the total acquisition time. This oversampling in one direction can prevent the aliasing if the object is larger than field of view (FOV) in that direction. Lastly, it is the easiest to implement Cartesian patterns of traversing k-space.

Nevertheless, Cartesian sampling suffers from low acquisition efficiency because it's quite time-consuming to acquire the complete k-space data line by line. As a result, various acquisition

strategies have been proposed to accelerate Cartesian sampling, such as to skip every x numbers of lines, use a Poisson disc under-sampling pattern [30–32], or use echo-planar imaging (EPI) [33]. Considering that the center of k-space contains important general shape information, it is usually recommended to fully acquire some center k-space lines.

1.4.2 Spiral trajectory sampling

1.4.2.1 Motivation

Today, non-Cartesian sampling strategies, like spiral interleaves, have been proposed to improve the acquisition efficiency, because spiral trajectories can cover a greater extent of k-space each repetition time (TR). The TR for spiral cardiac imaging at 3T can be twice as long as that used for Cartesian or radial imaging, resulting in an increase of the flip angle that can be used, thus providing a SNR advantage. Assuming a T_1 of myocardium of 1200 ms, an increase in the TR from 4 ms to 8 ms would increase the Ernst angle by 40%. Increasing the flip angle results in a corresponding increase in SNR. This increased TR also allows more time for inflow of unsaturated blood as compared to other acquisition strategies. The enhanced inflow effect should result in high SNR for the blood pool and higher blood-myocardial contrast-to-noise ratio (CNR) [34]. In addition, because each spiral interleaf starts from the center of k-space, spiral imaging is also robust to flow and motion artifacts [35]. Furthermore, considering the various design of spiral trajectories such as linear variable density or dual-density, spiral trajectory sampling offers us different kinds of under-sampling strategies that acquire more center k-space data than the edges. Therefore, it is possible to fully sample the center on each spiral interleaf, and self-gating can be performed without any need for additional navigator lines or projections.

1.4.2.2 Implementation considerations

Eddy current effects and/or hardware imperfections will lead to the deviation of the actual k-space trajectory from the theoretical one, especially for non-Cartesian sampling. This can cause the blurring and distortion of the reconstructed image. As it is not practical to measure the real k-space trajectory for every scan, it is essential to implement a robust trajectory correction technique that will work for different scans. In this dissertation, we used the optimal design from Meyer et al. [36] to generate the slew-limited spiral gradient trajectories, and an anisotropic gradient delay model with a simple eddy current model from Tan et al. [37] to estimate the actual k-space trajectory.

Besides, unlike Cartesian sampling, uniform sampling in time using spiral trajectories will result in non-uniform sampling of spatial frequencies. To process those unevenly spaced k-space data, before performing Fourier transform operation to transfer data to image space, the so-called "gridding" step have been proposed to morph the data into a square (or rectangular) grid. This can be achieved by multiplying the density compensation factor (DCF) with the original data and performing a convolution with a gridding kernel. The DCF that is generated by calculating the Voronoi region at each point with a cut-off at high under-sampling regions [38] and Non-Uniform Fast Fourier Transform (NUFFT) [39] were used in this dissertation.

1.4.2.3 Limitations

Even though the spiral trajectory sampling has a number of advantages to traverse k-space, clinical adoption of spiral sequence has been slower than that of Cartesian. This can be explained for several factors. Firstly, Cartesian sampling is especially robust with the presence of hardware imperfections such as eddy currents and time delays, while in most cases spiral trajectory sampling needs to utilize some correction methods to overcome the issues. In addition, the comparative longer TR for spiral might lead to some off-resonance problems, which appear as significant image blurring if not corrected. Furthermore, because spiral trajectory sampling does not have a dedicated

readout direction like Cartesian does, it is not possible to implement an anti-aliasing filter on the readout direction to prevent aliasing artifact.

1.5 Motion compensation

1.5.1 Respiratory motion compensation

A number of methods have been used to enable ECG-gated free breathing cine examinations. Diaphragmatic navigator-echo based methods [40–43] have been used to prospectively reduce respiratory motion, but these techniques require a dedicated navigator setup and adequate navigator quality with a clear liver-lung interface. Furthermore, these techniques are prone to errors resulting from the difference between diaphragmatic motion and cardiac motion. In the meantime, they typically preclude retrospective ECG gating, and the total scan time is prolonged depending on respiratory gating efficiency. Projection navigators acquired during bSSFP acquisitions have been successfully utilized to perform respiratory tracking without the need for a separate diaphragmatic navigator [44], but this approach is still limited by navigator gating efficiency. Recent studies [45–50] have used the acquired data itself to derive the respiratory gating signal. Data were then separated into different respiratory states [48,51,52] and reconstruction was performed using data from a subset of the respiratory states, or by using motion correction to combine data from different respiratory states.

In addition, non-rigid image-based motion correction strategies [53] use retrospective image registration, in which motion information is extracted from the acquired data and then used to correct data during image reconstruction. In general, the performance of these techniques is highly dependent on the quality of the non-rigid registration, which may be sensitive to the changes in SNR and CNR, through-plane motion, or other factors. While multiple methods for non-rigid motion registration have been proposed [54–56], repeated application of non-rigid registration

operators can result in image degradation due to spatial interpolation and can cause geometric distortion of the images. The complexity and potentially long image reconstruction time also limit their general application.

1.5.2 Cardiac motion compensation

Cardiac "self-gated" techniques [57,58] have been proposed to eliminate the need for ECG synchronization by acquiring and processing additional MR signals to derive cardiac cycle timing information, resulting in decreased imaging efficiency. These studies have extracted the cardiac "self-gating" signal from the acquired data during breath-holds [59–61] or free-breathing [51,52,62]. Previously reported cardiac self-gating approaches have used the *k*-space center point [58,63] or center *k*-space line [45,46,59,64] as navigator signals. In addition, those self-gating approaches usually require careful selection of receive coil elements to obtain self-gating signals as each coil has different sensitivity to cardiac motion and respiratory motion. Some techniques [59,65] also used image-based methods to obtain self-gating signals.

1.6 Accelerated imaging

1.6.1 Parallel imaging

Parallel imaging techniques have been widely used in MR field by taking the advantage of spatial information provided by using phased-array receiver coils. The usage of parallel imaging enables under-sampling by a factor of 2 or 3, which greatly reduces the acquisition time. In each parallel imaging acquisition, multi-coil data will be acquired and each channel image is weighted by the spatial sensitivity of the coil. The choice of optimal parallel imaging method depends on several factors. When the coil sensitivities are known and trustable, image-domain SENSE [66] should be the preferred option. If accurate coil sensitivity maps are difficult to obtain, self-calibrating techniques are more optimal: GRAPPA [67], where missing k-space data are synthesized

from neighboring acquired data; SPIRiT [68], where the reconstruction of each point depends on its entire neighborhood. For non-Cartesian SPIRiT [68], which is appropriate for spiral imaging, the reconstruction step can be solved as an optimization problem. To form it in an unconstrained Lagrangian way:

$$\underset{x}{\operatorname{argmin}}\|Dx - y\|^2 + \lambda\|(G - I)x\|^2, \tag{1.3}$$

where y is the acquired k-space data for all coils, and D is the operator to transform data from image, x, to the acquired data, y. G is a series of convolution operators that convolve the whole k-space with the suitable calibration kernels. λ is a trade-off parameter to balance the data acquisition consistency and the calibration consistency.

1.6.2 Compressed sensing techniques

Lustig et al. proposed to apply compressed sensing (CS) to MRI in 2007, based on the fact that MR data is naturally compressible by sparse coding in a transform domain and MRI scanners inherently acquire encoded samples in k-space [69]. The introduction of CS into the MR reconstruction has a huge impact on the fast-imaging field and further enables higher acceleration factor in the acquisition. The main idea of CS is to explore the sparsity of the data. For most cases in MRI, data need to be transformed into a sparse domain, such as spatial finite differences or wavelet coefficients. It is also important to make sure that the aliasing pattern due to under-sampling is incoherent, which makes spiral under-sampling an ideal solution. The CS reconstruction can also be formulated as an optimization problem, written as:

$$\underset{x}{\operatorname{argmin}}\|Dx - y\|^2 + \lambda\|\Psi x\|_1, \tag{1.4}$$

where Ψ represents a sparsifying transform operator.

Low-rank matrix completion extends the idea of CS to matrices, enabling recovery of missing data of a matrix in the condition of low-rank and incoherence [70]. To make use of both

compressed sensing and low-rank matrix completion, Otazo et al. [71] proposed the Low-rank plus Sparse (L+S) matrix decomposition as a convex optimization problem:

$$\min_{L,S} \frac{1}{2}\|E(L+S)-d\|_2^2 + \lambda_L\|L\|_* + \lambda_S\|TS\|_1, \quad (1.5)$$

where E is the encoding operator and d is the acquired data. $\|L\|_*$ is the nuclear norm of the low-rank matrix L. $\|TS\|_1$ is the l_1-norm of the entries of TS, in which S is a sparse matrix and T is a sparsifying transform. This unique decomposition is ideal for MR dynamic imaging, because L can model the temporally correlated background while S can represent the dynamic information that exists on top of the background [71].

While CS enables acceleration of data acquisition by exploiting signal sparsity, prior knowledge about the signal evolution can be utilized to choose an appropriate sparsifying transform to further improve the reconstruction. Dictionary learning (DL) was applied to brain MR image reconstruction by several groups [72,73] to learn the spatial sparsifying directly from the under-sampled *k*-space data, which can be formed as the following optimization problem:

$$\min_{D,\Gamma} \sum_{ij} \left\|R_{ij}x - Da_{ij}\right\|_2^2 \qquad s.t. \left\|a_{ij}\right\|_0 \le T_o \qquad \forall\, i,j. \quad (1.6)$$

In the above expression, x indicates the image. Matrix R_{ij} is the operator to extract x_{ij} from x as $x_{ij} = R_{ij}x$. D represents the image dictionary. a_{ij} is the sparse representation of x_{ij} with respect to D. T_o is the required sparsity level. Γ is used to denote the set $\{a_{ij}\}_{ij}$ of sparse representations. Specifically, for parametric mapping such as T_1 mapping, signal evolutions can be modeled using Bloch simulation. Recently, DL was used in T_1 mapping where a dictionary was formed using Bloch simulation and used as a regularization term in the reconstruction problem [72,74]. The use of dictionary learning improved image quality in T_1 maps compared to the conventional SENSE method [74].

1.7 Multi-contrast imaging

Recently, to accelerate and simplify the MRI exams, multi-contrast imaging has become an interesting and popular topic. The MR fingerprinting (MRF) technique [75,76] utilizes a complex incoherent acquisition strategy and matches the corresponding dictionary curves generated by Bloch simulation to extract T_1 values. This technique depends on sufficient variation between the signal evolutions of tissues with different T_1 values, and is subject to the fidelity of the model accurately modeling the real acquisition. It was first applied to brain MRI [75] to simultaneously obtain proton density, T_1, T_2 maps along with off-resonance distribution. Then, studies have been proposed to apply MRF to cardiac imaging to acquire proton density, T_1 and T_2 maps at the same time with a single breath-hold and ECG gating [76].

Alternatively, Qi et al. [77] have proposed a free-running 3D T_1 and T_2 mapping along with cine images for isotropic spatial resolution. This allowed for free-breathing but still needed ECG to synchronize the cardiac motion. The recently developed CMR multi-tasking technique [78] has shown great potential to obtain cine images and T_1 maps at the same time in a continuous radial acquisition scheme. In this case, every other radial *k*-space data is used as auxiliary data to resolve both cardiac and respiratory motion. One limitation is that when a Look-Locker type acquisition is performed continuously, the recovery time constant T_1^* is a function of both flip angle and T_1. It is thus impossible to distinguish between the effects of flip angle and T_1 relaxation as has been discussed previously by Crawley and Henkelman [79]. Therefore, a B_1^+ map is needed to accurately determine T_1 from the effective T_1^* in such acquisitions. Since a B_1^+ map is often acquired using a separate specialized pulse sequence, there is a potential for mis-registration between the B_1^+ map and the other acquired data, particularly for a cardiac and respiratory self-gated acquisition.

1.8 Dissertation overview

The overall goal of this dissertation is to develop an acquisition strategy that simultaneously acquires cine images, T_1 maps and LGE images when the patient is free-breathing and cardiac self-gating. The dissertation is organized as follows:

Chapter 1 gives a general background of the dissertation.

Chapter 2 presents a simple robust rigid motion compensation strategy using an automatic heart detection algorithm to perform a dynamic 2D cardiac perfusion MRI. The goal of this strategy is to reduce respiratory motion artifacts and improve image quality for the standard k-t acceleration and CS techniques. The strategy was tested both in a numerical phantom and with patients undergoing clinically ordered CMR studies.

Chapter 3 describes SPARCS, a strategy that continuously acquires golden-angle spiral interleaves for cine imaging. The goal of this strategy is to provide an efficient free-breathing and cardiac self-gating cine imaging technique. For 3 T applications, a spoiled gradient echo readout was used. For 1.5 T application, a bSSFP readout was used. This strategy was evaluated with both healthy volunteers and patients undergoing clinically ordered CMR studies.

Chapter 4 provides a technique to acquire cine images and T_1 map in a single free breathing acquisition. Continuous golden-angle rotated spiral trajectories were acquired by including pauses for relaxation before inversion recovery pulses. T_1 maps were generated using the whole recovery curve, while cine images were reconstructed from the part where the signal is approaching steady state. This technique was investigated in human subjects and compared to the breath-hold MOLLI technique and the bSSFP Cartesian cine images most often used in clinical settings.

Chapter 5 details the design of a dual excitation flip angle technique that provides cine images, B_1^+ and slice profile corrected T_1 maps and LGE images from a single continuous acquisition. Without breath-holding or ECG-gating, data were acquired continuously using a

golden-angle gradient-echo spiral pulse sequence, with an inversion RF pulse applied every four seconds. 3° and 15° flip angles were used for readouts after the first four and second four inversions. This strategy was evaluated in a phantom and with 14 human subjects.

Chapter 6 introduces a strategy to acquire free breathing Bloch-Siegert shift B_1^+ map, and a self-gated B_1^+ and slice profile corrected T_1 map. The technique is compared to the dual flip angle approach described in Chapter 5. Both techniques are evaluated in phantom, healthy volunteers and patients undergoing clinically ordered CMR studies, and compared to MOLLI and SASHA techniques.

Chapter 7 summarizes the work of this dissertation's accomplishments and provides some insights for the future directions.

Chapter 2: Respiratory motion correction strategy for first-pass perfusion imaging

2.1 Introduction

Adenosine stress first-pass contrast-enhanced CMR perfusion imaging has been shown to have excellent diagnostic and prognostic utility in evaluating coronary artery disease (CAD) [80–83]. It has a number of advantages over other modalities including lack of ionizing radiation, and comparatively higher spatial and temporal resolution.

Clinically available CMR techniques typically have incomplete slice coverage due to temporal and spatial resolution constraints. Current clinical techniques are limited to acquire 3 to 4 short axis slices per heartbeat with a spatial resolution of 2-3 mm and temporal resolution of 100-180ms [84]. Most clinical techniques use parallel imaging techniques such as SENSE [66] or GRAPPA [67] at low acceleration factors of 2 to 3. These techniques typically fully sample a central region of k-space for auto-calibration of coil sensitivity or GRAPPA kernels which slightly reduces the effective acceleration rate. Alternatively, techniques such as temporal SENSE (TSENSE) [85] and temporal GRAPPA (TGRAPPA) [86] can be used to reduce the temporal footprint by utilizing time averaged data for kernel calibration or sensitivity maps in lieu of acquiring a fully-sampled k-space center during each heartbeat. A number of spatial-temporal accelerated techniques such as k-t BLAST/k-t SENSE [87] and k-t PCA [88] have been developed to address these limitations and have demonstrated excellent clinical performance [89–91]. These techniques rely on the high degree of spatiotemporal correlation within the dynamic dataset to constrain the image reconstruction. Recently, compressed sensing techniques [92] have been applied to myocardial perfusion imaging [93–96]. These techniques use a non-linear reconstruction to recover the images from incoherent

under-sampled data; relying on the fact that the dynamic image data has a sparse representation in some transform domain.

Although the above fast imaging techniques can significantly accelerate image acquisition to mitigate limited temporal and/or spatial resolution, in the presence of respiratory motion, these techniques can suffer from significant degradation of image quality [97,98]. Robust routine clinical application of these techniques can be limited by their sensitivity to respiratory motion-induced artifacts. A number of approaches for respiratory motion corrected reconstruction have been proposed, but they have limitations as described in 1.5.1. In an ECG gated first-pass perfusion image sequence, the heart is in the same cardiac phase in each image, and the predominant variation in cardiac position is due to respiratory motion in the head-foot direction. As such, we proposed a simple robust respiratory motion compensation strategy for *k*-t accelerated and compressed-sensing CMR perfusion imaging to selectively correct respiratory motion of the heart. This is based on linear *k*-space phase shifts derived from rigid motion registration of a heart ROI.

2.2 Methods

2.2.1 Data sampling strategy

Figure 2.1 shows the sampling mask and point spread function (PSF) of 3 different sampling patterns.

A sheared grid sampling strategy (Figure 2.1(a,b)) is usually used for *k*-t PCA reconstruction. In the absence of motion, the coherent aliasing is optimal for parallel imaging reconstruction since there is minimal overlap of aliased image structures. However, in the presence of respiratory motion the high-energy side lobes result in coherent residual aliasing artifacts.

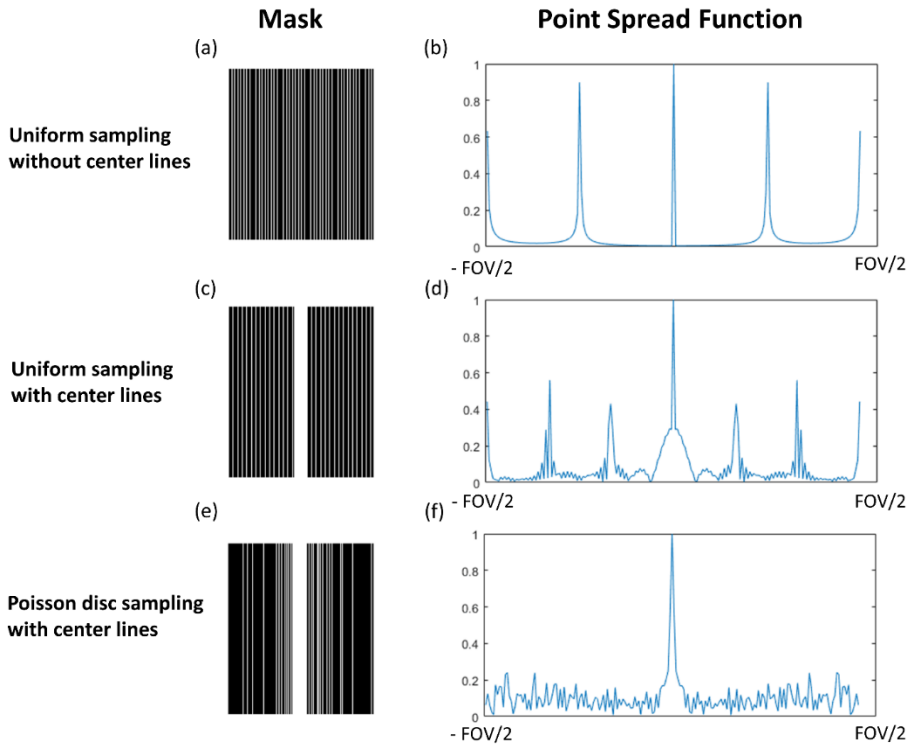

Figure 2.1 Sampling mask and point spread function comparison. 4 times accelerated uniform under-sampling without center lines (a,b), uniform under-sampling with center lines (c,d) and variable density Poisson disc under-sampling (e,f).

In practice, the center of k-space is typically fully sampled in the *k*-t PCA technique to derive the temporal basis functions (Figure 2.1(c,d)). This data can be used to reduce the coherency of aliasing when using an iterative *k*-t PCA approach. It results in broadening of the main lobe of the PSF in exchange for lowering the amplitude of the aliasing side lobes. However, the above 2 uniform under-sampling strategies both generate high energy aliasing peaks of more than 50% of the main lobe.

A variable density Poisson disc under-sampling strategy (Figure 2.1(e,f)) is often used for compressed sensing techniques such as *k*-t SLR, because it meets the CS criteria of incoherent sampling. By using this sampling pattern, there is a broadened main lobe with low-energy incoherent aliasing side lobes with a peak amplitude of less than 20% of the main lobe. This property provides tolerance to motion. Thus, in the presence of respiratory motion, this sampling strategy could also be beneficial for *k*-t PCA reconstruction.

2.2.2 Motion correction strategy

The reconstruction pipeline utilized for our motion-compensated reconstruction strategy is depicted in Figure 2.2.

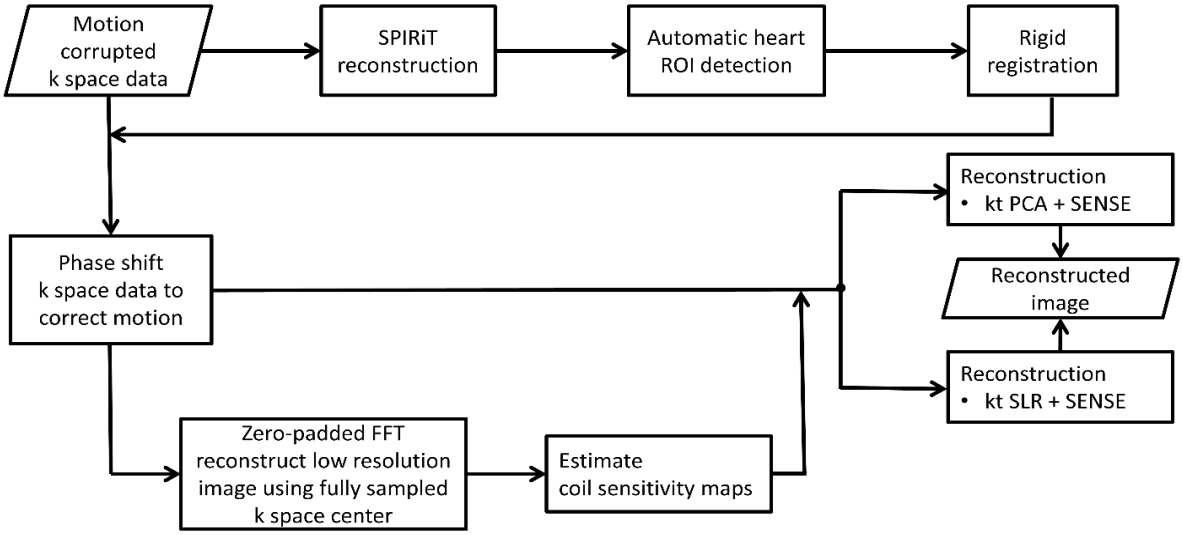

Figure 2.2 Respiratory motion-corrected reconstruction pipeline

Firstly, the data from each frame are independently reconstructed using SPIRiT [68] to obtain images of sufficient quality for rigid registration. This parallel-imaging only approach is used to derive the motion estimates without the temporal blurring that occurs with *k*-t or CS acceleration in the setting of respiratory motion. Next an 80×80 pixel-size ROI containing the heart is automatically detected based on the fact that the ventricular cavities have the largest magnitude of change in signal intensity over the first-pass of the contrast. Thus, the ROI containing the heart can be automatically detected by finding the largest connected region of high standard deviation on a standard deviation map of signal intensity calculated from all of the frames of the dynamic dataset. Next, rigid registration is performed over the square heart ROI to determine the in-plane displacements required to compensate for the bulk changes in the heart position resulting from respiratory motion. While breathing results in non-rigid motion of structures of the chest, the motion of a small rectangular ROI around the heart on an ECG gated short-axis image can be reasonably approximated by in-plane rigid motion in the head-foot and anterior-posterior

directions. Rigid registration was performed by using mutual information as a metric to determine the rigid transformation from the source image to that of the target image [99]. In order to minimize respiratory drift, pairwise rigid registration of images was performed over a 15-frame window, which means the n^{th} frame is registered from $(n-7)^{th}$ to $(n+7)^{th}$ frame. The obtained displacement information is used to derive the appropriate *k*-space linear phase shifts to register the heart throughout the temporal series. These linear phase shifts are then applied to the acquired raw *k*-space data for each frame of the dynamic dataset. Note that this will selectively register the region around the heart and potentially result in suboptimal registration of the structures remote from the heart.

2.2.3 Image reconstruction

Following the image registration as described above, the phase shifted *k*-space data is used to perform standard *k*-t PCA/SENSE or *k*-t SLR/SENSE image reconstruction. Coil sensitivity maps are created using the temporally averaged fully-sampled *k*-space center through a modified Walsh method [100] and used for both reconstruction techniques.

K-t PCA reconstruction

For *k*-t PCA/SENSE algorithm, the center 10 fully sampled phase-encoding lines in *k*-space are used as training data for principal component analysis (PCA) to obtain the temporal basis functions. *K*-t PCA reconstruction is performed using an iterative *k*-t PCA approach as described previously [88].

K-t SLR reconstruction

The *k*-t SLR/SENSE algorithm is performed using iterative singular value thresholding (IST) [101]. For fair comparison to the *k*-t PCA technique, image sparsity was not exploited during image reconstruction.

Non-rigid Motion Correction reconstruction

To evaluate the performance of rigid versus non-rigid motion correction approach, iterative *k*-t PCA and *k*-t SLR were performed using non-rigid registration with a non-linear conjugate gradient solver. Non-rigid *k*-t PCA reconstruction was performed using iterative *k*-t PCA as described above. Non-rigid registration was performed by Advanced Normalization Tools (ANTs) using symmetric normalization including affine and deformable transformation, with mutual information as optimization metric [102]. For non-rigid *k*-t SLR, the low-rank constraint was enforced on the non-rigid motion corrected data. These approaches were chosen to be able to directly compare *k*-t PCA and *k*-t SLR with rigid registration approaches. Images were also reconstructed using *k*-t FOCUSS [103,104] which is a compressed sensing technique that uses a motion-estimation motion-correction strategy. The key-frame was derived from the temporal averaged data.

2.2.4 Numerical phantom validation

In order to evaluate the performance of the different under-sampling patterns (sheared-grid and Poisson-disk, both with 10 fully sampled lines at the *k*-space center) and reconstruction strategies (*k*-t PCA and *k*-t SLR), we utilized an MR-XCAT phantom with realistic respiratory motion [105]. To simulate the image quality of CMR perfusion images, noise was added to the phantom. Raw data with 160 phase encoding lines were simulated.

For the sheared-grid sampling, a variable-density *k*-t sampling which included a 4x accelerated sheared-grid pattern and a fully sampled central 10 phase encoding lines was used. For the variable density Poisson disc sampling pattern, the central 10 phase-encoding lines were fully acquired in each frame while the outer 30 phase-encoding lines were under-sampled following a variable density Poisson disc distribution in the phase encoding direction and a uniform Poisson

disc sampling along the temporal direction. Images sampled with these two sampling strategies were reconstructed using *k*-t PCA and *k*-t SLR with and without MC separately.

2.2.5 In-vivo study

Resting first-pass perfusion imaging was performed in 12 subjects undergoing clinically ordered CMR studies. Written informed consents were obtained from all subjects, and imaging studies were performed under institutional review board (IRB) approved protocols. Perfusion imaging was performed using 0.075 mmol/kg Magnevist (Bayer AG, Leverkusen, German) injected intravenously at a rate of 4 mL/s followed by 25 mL saline flush at 4 mL/s.

Scanning was performed on a 1.5 T scanner (MAGNETOM Avanto, Siemens Healthineers, Erlangen, Germany) at University of Virginia Medical Center. Multi-slice 2D saturation-recovery first-pass gadolinium-enhanced data were collected using a standard body phased-array RF coil. Sequence parameters included: FOV = 320 mm, TR = 2.4 ms, TE = 1.19 ms, saturation recovery time = 100 ms, voxel size = 2.0×2.0 mm^2, matrix size = 320×160, slice thickness = 8 mm. For each patient, 3 short-axis slices were acquired per heartbeat for 50-70 heartbeats. We first performed prospectively 4x (Pro R4) accelerated first-pass perfusion data in 10 patients with 96 ms acquisition-window for each slice. We also collected two data sets with prospectively 6x (Pro R6) accelerated data, where the acquisition window was further shortened to 64 ms per slice. This was done to maintain the same voxel size for comparison to the prospective 4x data.

2.2.6 Image analysis

For numerical phantom experiments, to test the performance of this motion compensation strategy, the Poisson disc under-sampled *k*-t PCA and *k*-t SLR reconstruction results with and without MC were compared. For the phantom studies, the image quality in the heart ROI was assessed in a ROI around the heart by comparison to the fully sampled images using normalized

RMSE and SSIM [106]. These metrics were compared among all frames using two-way ANOVA with each image frame serving as a separate block. Post hoc comparisons between techniques were performed using a paired difference test with Tukey correction for multiple comparisons. All statistical tests were performed using SAS software 9.4 (SAS Institute Inc., Cary, NC).

For in-vivo studies, image quality was assessed by two experienced cardiologists blinded to the reconstruction technique. To facilitate blinding, the non-motion corrected and non-rigid motion corrected datasets were rigidly registered by deriving the displacements from a region around the heart after reconstruction and the images were cropped around the heart. Image quality was evaluated on a 5-point scale ranging from 1 (poor) to 5 (excellent). Images were also ranked in numerical order from 1st (best) to 4th (worst) not allowing for ties. In a separate analysis, *k*-t PCA and *k*-t SLR with rigid-registration were compared to *k*-t PCA and *k*-t SLR with non-rigid registration, and to *k*-t FOCUSS using the same grading and ranking scheme by the expert reviewers. Statistical analysis using SAS software was performed using an ANOVA analysis with Tukey's Studentized Range test to correct for multiple comparisons.

2.3 Results

Figure 2.3 shows the results from the MR-XCAT phantom reconstructed with and without motion correction.

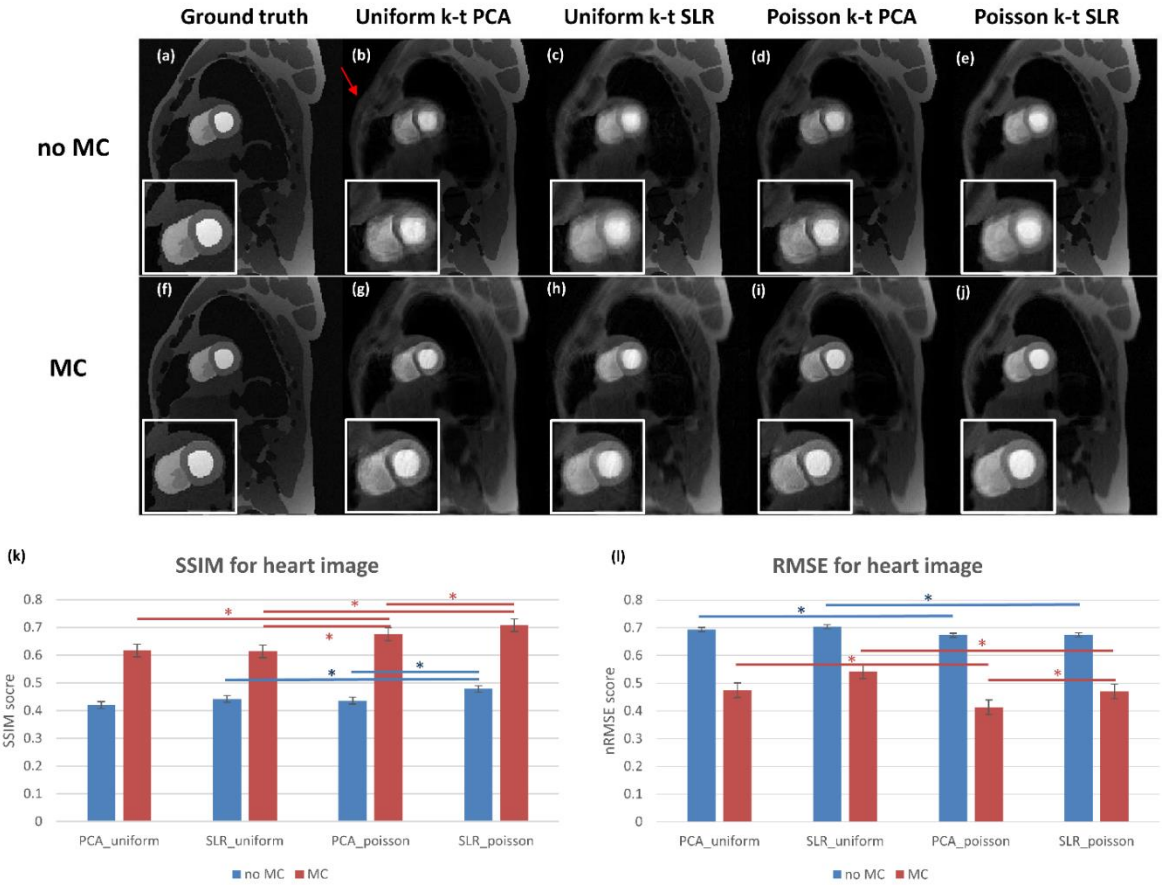

Figure 2.3 MR-XCAT phantom of uniform and Poisson disc under-sampling reconstruction with and without motion correction. The top part of the figure shows one static frame image results, and the first row corresponds to the ones without motion correction while the second row refers to the ones with motion correction. Each column represents the fully sampled ground truth (a,f), results from uniform under-sampling using k-t PCA (b,g), k-t SLR (c,h), Poisson disc under-sampling using k-t PCA (d,i) and k-t SLR (e,j). The red arrow indicates 1 example of the aliasing caused by under-sampling. (k) and (l) are statistic SSIM and normalized RMSE scores comparing the above 4 methods with the fully sampled ground truth among all frames. * indicates $p < 0.05$. *All the motion corrected results have significant higher SSIM ($p < 0.05$) and significant lower RMSE ($p < 0.05$) compared to the ones without motion compensation (not shown)*.

The SNR of the phantom on this frame was 12.8. The first column in Figure 2.3 shows the fully-sampled ground truth image without (Figure 2.3(a)) and with (Figure 2.3(f)) motion correction. In the sheared-grid sampled data reconstructed with *k*-t PCA (Figure 2.3(b)), there are discrete aliasing artifacts resulting from incomplete decoding in the presence of respiratory motion, which significantly degrades image quality. As the motion strategy corrects for heart motion, there are still aliasing artifacts in the *k*-t PCA with sheared-grid under-sampling (Figure 2.3(g)) resulting from the chest wall which has some motion that is not corrected. For *k*-t PCA with Poisson disc

sampling without motion correction (Figure 2.3(d)) there are less discrete aliasing artifacts and image quality is slightly improved in the region of the heart. The image with motion correction (Figure 2.3(i)) does not have discrete aliasing and has higher image quality. As expected, *k*-t SLR performs poorly for uniform under-sampling without motion correction (Figure 3(c)), resulting in some discrete aliasing, whereas for the Poisson disc sampling without motion correction (Figure 2.3(e)), there are no discrete aliasing artifacts. With motion correction, *k*-t SLR with uniform under-sampling (Figure 2.3(h)) again performs poorly due to the sampling requirements of CS which are not met, whereas the Poisson disc *k*-t SLR (Figure 2.3(j)) results have good image quality without blurring. For both *k*-t PCA and *k*-t SLR, Poisson disc sampled images have higher SSIM and lower RMSE compared to uniform sampled ones ($p < 0.05$). Moreover, for the Poisson disc sampling strategy *k*-t SLR has a higher similarity index than k-t PCA ($p < 0.05$). Without motion correction, there is significant spatial blurring and there are artifacts in the region of the myocardium which has lower SSIM ($p < 0.05$) and higher RMSE ($p < 0.05$).

By comparing the images in Figure 2.3, the images using Poisson disc under-sampling have better image quality than those using uniform under-sampling. *K*-t SLR typically out-performed *k*-t PCA in the setting of respiratory motion.

Figure 2.4 shows a comparison between *k*-t PCA and *k*-t SLR reconstruction results with and without motion correction acquired with a 4x accelerated Poisson disc under-sampling strategy as described above.

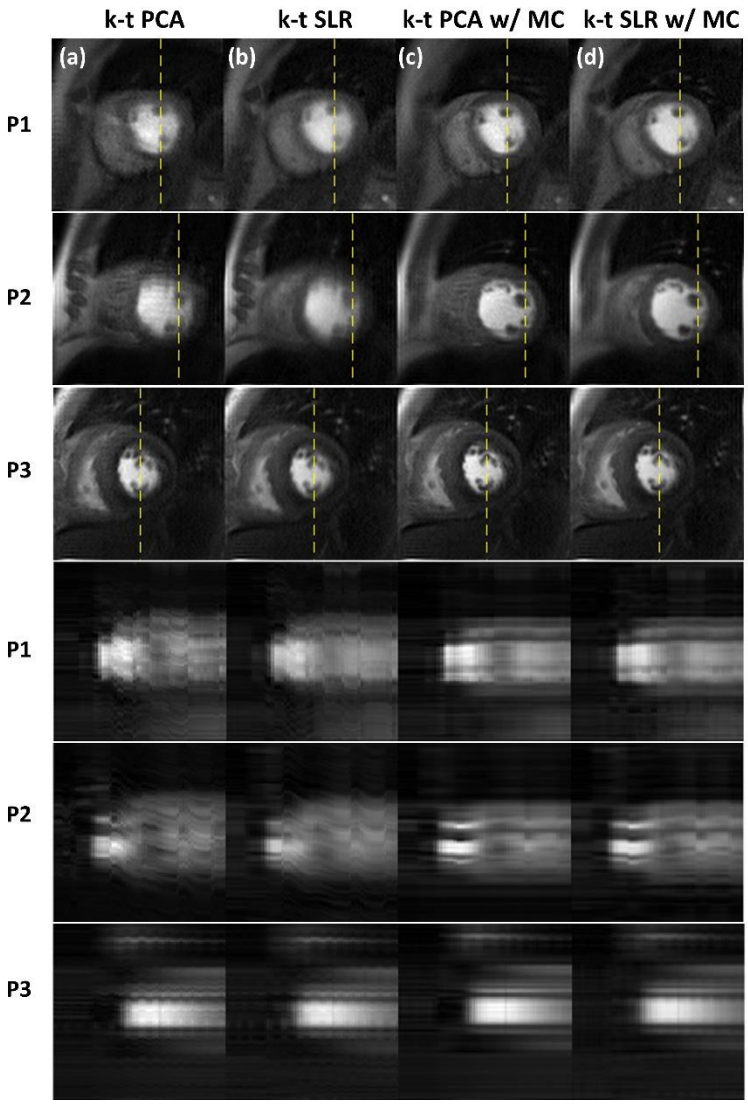

Figure 2.4 k-t PCA and k-t SLR reconstructions with and without motion compensation for patients. The top 3 rows are the reconstructed images at one frame and the bottom 3 rows are the x-t profiles for the dashed line pointed in the frames. Comparisons are made among reconstruction by without motion correction k-t PCA (a) and k-t SLR (b), with motion correction k-t PCA (c) and k-t SLR (d).

For subjects 1 and 2, when there is a significant amount of respiratory motion, the images reconstructed with *k*-t PCA and *k*-t SLR without motion compensation have significant blurring artifacts over the heart as compared to those with motion compensation. X-t profiles of motion corrected data show sharper borders between the blood pool and the myocardium, and the trabeculations can be well visualized. For the third subject in the figure there is minimal respiratory motion. Images with motion compensation look slightly sharper than the non-motion corrected images, but the differences are subtle. Similarly, the x-t profiles are similar between the motion corrected and non-motion corrected reconstructions. Note in this figure for comparison the

x-t profiles for the non-motion corrected techniques have been registered after reconstruction for display purposes.

Figure 2.5 shows perfusion images from the 30th frame (a-e) and the 68th frame (f-j) of a first-pass dataset acquired with 6x Poisson-disk under-sampling.

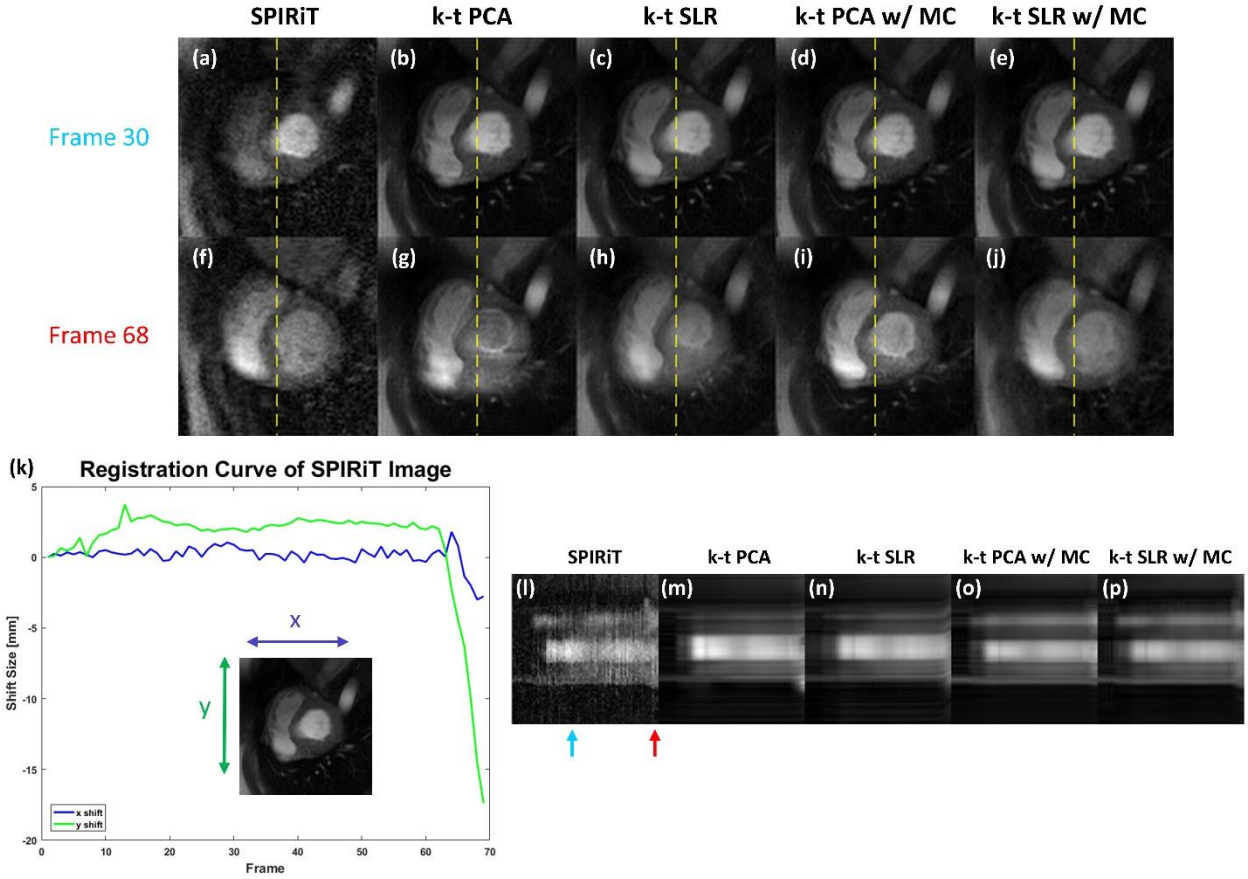

Figure 2.5 Reconstruction comparison of a subject with 6x accelerated Poisson disc undersampling. Reconstruction results are shown at 30th and 68th frame. Each column corresponds to direct SPIRiT reconstruction with registration (a,f), non-motion corrected k-t PCA (b,g) and k-t SLR (c,h), motion corrected k-t PCA (d,i) and k-t SLR (e,j). The temporal x and y-shifts of the heart position derived from rigid registration of the SPIRIT images (k) demonstrate that the patient took a deep breath near frame 60. The x-t profiles for the above 5 reconstruction methods are shown (l-p) with colored arrows denoting the 30th and 68th frames.

Figure 2.5(k) shows the temporal x and y-shifts of the heart position derived from rigid registration of the SPIRiT images. The x-t profiles for the above 5 reconstruction methods are shown in Figure 2.5(l-p) with colored arrows denoting the 30th and 68th frames. In this case, the subject held his breath reasonably well until frame 65 where he took a deep breath resulting in through-plane motion. This can be clearly seen in the SPIRiT reconstructed images. Note all

reconstructions demonstrate good image quality for the 30th frame. However, for the 68th frame the non-motion corrected *k*-t PCA and *k*-t SLR images have significant blurring artifacts. The motion-corrected *k*-t PCA images fail to show the through-plane motion. The motion-corrected *k*-t SLR images are able to capture this through-plane motion, albeit with some blurring of the inferior wall.

Figure 2.6 shows the comparison of scores and ranks for the cardiologists for *k*-t PCA and *k*-t SLR reconstructions for the 10 cases acquired with 4x under-sampling with and without motion-compensated reconstruction.

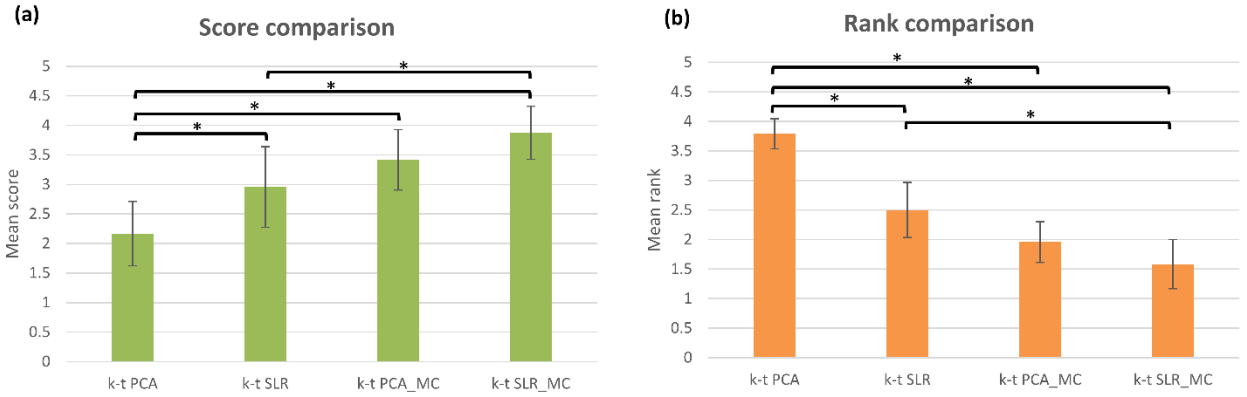

Figure 2.6 Score (a) and rank (b) comparisons of k-t PCA and k-t SLR reconstruction results with and without motion compensation by two experienced cardiologists. Four bars in each plot from left to right correspond to *k*-t PCA and *k*-t SLR without motion compensation, *k*-t PCA and *k*-t SLR with motion compensation. The scale of the scores ranges from 1 (very poor) to 5 (very good) and the scale of the ranks range from 1st to 4th. Error bars indicate the standard deviation, and * indicates significance at $p < 0.05$.

In the score plot (Figure 2.6(a)), the non-motion corrected reconstructions had significantly worse image quality scores than the motion corrected reconstructions ($p < 0.05$) for *k*-t PCA and *k*-t SLR. For non-motion-compensated reconstructions, there was significant higher image quality score for *k*-t SLR as compared to *k*-t PCA. Similar results were seen in the plot of the rank data (Figure 2.6(b)). *K*-t PCA and *k*-t SLR images with motion corrected reconstructions had significant better ranks than those without motion-compensated reconstruction ($p < 0.05$). Again, there were significant differences in rank between non-motion corrected *k*-t PCA and *k*-t SLR. Although the

difference between motion-corrected *k*-t PCA and *k*-t SLR is not significant, *k*-t SLR with motion correction had the best point estimates for mean score/rank of the techniques.

Figure 2.7 shows the results for the comparison of rigid-motion corrected *k*-t PCA and *k*-t SLR, non-rigid corrected *k*-t PCA and *k*-t SLR and *k*-t FOCUSS. As compared to our rigid-registration approach, the non-rigid registration correction using *k*-t PCA and -t SLR tended to have geometric distortion and blurring. *K*-t FOCUSS had a lower apparent SNR and also had some blurring and aliasing artifacts in frames with significant motion. The x-t profiles in the bottom rows show more temporal blurring and noise as compared to our proposed approach.

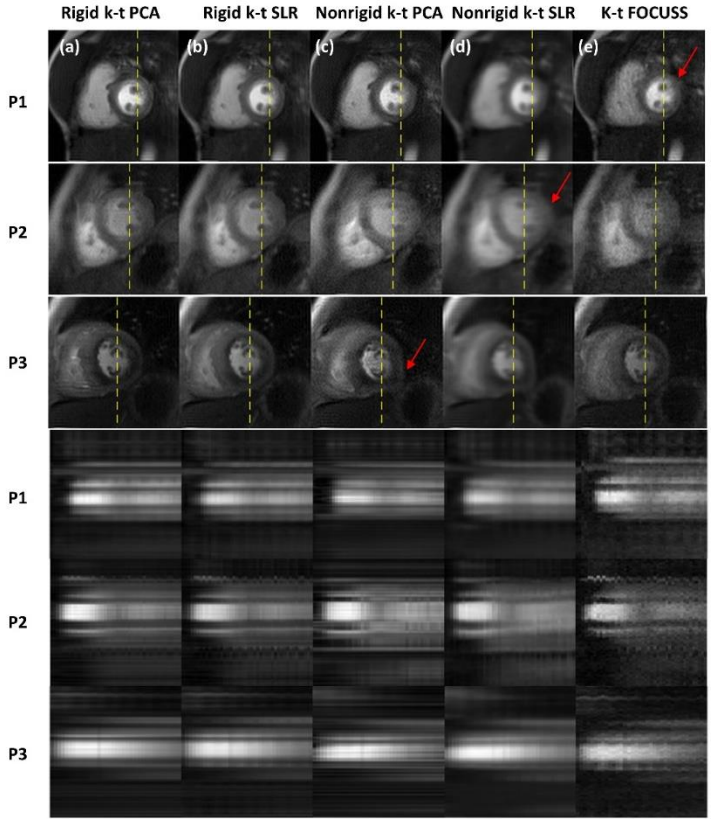

Figure 2.7 Motion correction rigid k-t PCA/SLR, nonrigid k-t PCA/SLR and k-t FOCUSS image reconstruction results for patients. The top 3 rows are the reconstructed images at one frame and the bottom 3 rows are the x-t profiles for the dashed line pointed in the frames. Comparisons are made among the proposed motion corrected rigid k-t PCA (a), rigid k-t SLR (b), as well as nonrigid k-t PCA (c), nonrigid k-t SLR (d) and k-t FOCUSS (e). Red arrows indicate some distortions and blurring deviation, and * indicates significance at $p < 0.05$.

As shown in Figure 2.8, the image quality scores and ranks were significantly higher ($p < 0.05$) for *k*-t PCA and *k*-t SLR with rigid motion correction as compared to the other motion-corrected reconstruction approaches.

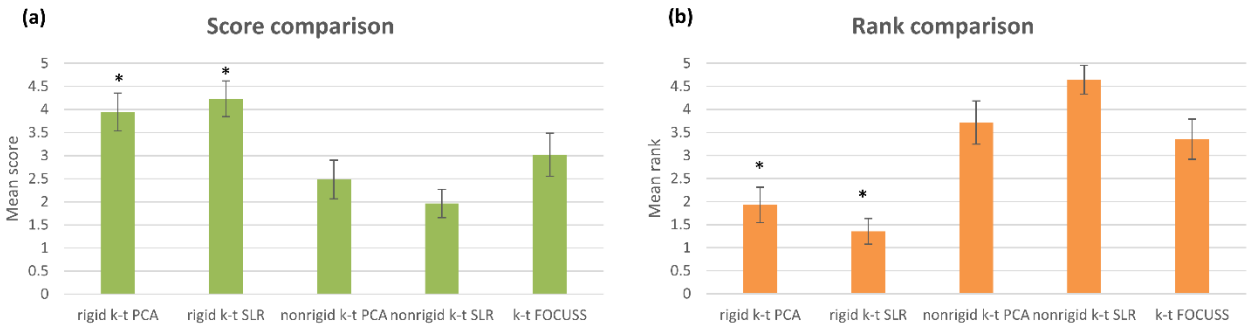

Figure 2.8 Score and rank comparisons among motion correction rigid k-t PCA/SLR, nonrigid k-t PCA/SLR and k-t FOCUSS reconstruction results by two experienced cardiologists. 5 bars in each plot from left to right corresponds to motion corrected rigid *k*-t PCA and *k*-t SLR, motion corrected nonrigid *k*-t PCA and *k*-t SLR, and motion corrected *k*-t FOCUSS. The scale of the scores ranges from 1 (very poor) to 5 (very good) and the scale of the ranks range from 1st to 5th. Error bars indicate the standard deviation, and * indicate the significance between rigid *k*-t PCA/*k*-t SLR and other methods.

2.4 Discussion

In this work, a simple robust motion correction strategy to reconstruct under-sampled motion corrupted dynamic perfusion MR data has been proposed. The method is based on deriving rigid translations of a ROI around the heart, and applying the linear phase shifts to the whole raw *k*-space as a pre-processing step. Our reconstruction strategy provides a simple way to remove respiratory motion artifacts in the heart region at the expense of some motion degradation of anatomy remote from the heart.

In this way, motion is corrected in the vicinity of the heart resulting in improved *k*-t accelerated and CS reconstruction of the heart. This property makes the strategy suitable when only a region around the heart is of interest, such as during cardiac first-pass perfusion imaging. Because of the large contrast change in the ventricular cavities during first-pass perfusion imaging, the automatic detection of the heart ROI based on the temporal standard deviation of signal intensity performs well for this application. The heart ROI was successfully detected in all cases. The strategy significantly reduces respiratory motion artifacts from poor breath-holding, thus improves image quality in the setting of respiratory motion. Alternatively, this strategy can also

be used for other cardiac imaging, such as cine images, where the most dynamic change in the FOV happened around the heart as well.

A sheared-grid sampling pattern should theoretically be optimal in terms of separating aliased replicates in x-f space [87], in the setting of respiratory motion. A prior perfusion study using *k*-t SENSE has demonstrated significant discrete aliasing artifacts, which can significantly impact image quality [97]. We showed a similar result in the MR-XCAT phantom with a sheared grid pattern, and demonstrated that image quality in the setting of respiratory motion is improved by using a Poisson disc sampling pattern with less discrete aliasing pattern. In the patient studies, we also demonstrated that using rigid motion correction around the heart further improves the quality of image reconstruction for *k*-t PCA in the setting of significant respiratory motion.

For *k*-t SLR, an example of a compressed-sensing reconstruction that may be sensitive to respiratory motion, it is demonstrated significant improvement in image quality using this rigid motion correction approach in both the MR-XCAT phantom and patient studies. In comparison of these techniques (*k*-t PCA and *k*-t SLR) both with and without motion correction, we found the best results from motion-corrected *k*-t SLR. This is particularly demonstrated in the case shown in Figure 2.5, where the patient has obvious through-plane motion resulting in significant shape changes of the heart during a small number of temporal frames at the end of the acquisition. As *k*-t PCA models the temporal basis functions directly from the training data, when motion occurs over a small number of frames, the *k*-t PCA calibration may become biased towards the motion-free frames and may not accurately capture changes due to through-plane motion. In *k*-t SLR, the low-rank constraint is enforced iteratively with soft-thresholding, potentially reducing sensitivity to bias from a small number of discordant frames.

While currently more complex techniques for motion corrected *k*-t acceleration exist [48,54,98,107], their performance is highly dependent on non-rigid registration, which is sensitive to image quality related factors. As we had tested in Figure 2.7, in the non-rigid registration cases, the complex computation has a potential to result in geometric distortion of the images and blurring. In addition, running non-rigid registration motion correction methods require longer image reconstruction time, limiting their general applications. By comparison, the approach utilized in this dissertation has a number of advantages. Firstly, rigid translations are easily determined even in images with some degrees of residual aliasing where occasionally non-rigid registration will fail and attempt to register the aliasing artifacts. Secondly, as only translations are being estimated, there is no possibility of the registration causing geometric distortions of the heart, which may occur with non-rigid registration techniques. Considering that the registration only phase shifts the *k*-space data, it avoids spatial blurring resulting from the repeated application of non-rigid registration operators during conventional iterative motion-compensated reconstruction [108]. In addition, this strategy does not only apply to Cartesian sampling as shown here, but also is suitable for non-Cartesian techniques, such as radial or spiral trajectories. Furthermore, this registration step could be easily added as a pre-processing step for current *k*-t PCA and *k*-t SLR pipelines. Although we did not evaluate the technique during stress perfusion in this study, we would expect to see similar findings during stress perfusion acquisition.

This reconstruction technique has some inherent limitations. As with most 2D registration techniques, the registration is sensitive to through-plane motion. While non-rigid motion techniques can register the heart on beats with mis-triggering, rigid registration does not allow any deformation of the heart resulting in some residual motion of the heart. As these were all clinical patients, the majority of patients had difficulty holding their breath for 50-70 heart beats, which is

about 30-60 seconds. The proposed technique may not work if the patient takes very large breaths resulting in significant through-plane motion.

2.5 Conclusion

A simple robust rigid motion compensation strategy is presented for dynamic 2D cardiac perfusion MRI. It greatly reduces motion artifacts and improves image quality for the standard k-t acceleration (k-t PCA) and CS (k-t SLR) techniques in setting of respiratory motion.

Chapter 3: Free breathing cardiac self-gated cine imaging

3.1 Introduction

Cardiac magnetic resonance cine imaging is widely regarded as the "gold-standard" technique for the non-invasive assessment of cardiac function. Typically, images are acquired using breath-held 2D segmented ECG-gated balanced steady-state free precession (bSSFP) pulse sequences. The approach of using ECG triggering and breath-hold acquisition has several limitations. Firstly, the ECG signal can be distorted, particularly at higher field strengths (3T), due to the magnetohydrodynamic effect [109], rapid switch of magnetic-field gradients [110], as well as radiofrequency interference [111,112] resulting in mis-triggering. Furthermore, optimal placement of the ECG leads increases the time to prepare the patient for the CMR exam. Additionally, a significant number of patients are not able to adequately hold their breath during cine acquisition, resulting in motion artifacts and the need to repeat image acquisition of the same slice location on subsequent breath-holds. Even if the patient can perform good breath-holds, this approach is inefficient as it requires 10-12 breath-holds to cover the left ventricle (LV), which can take longer than 10 minutes, and requires coordination between the operator and the patient. Real-time imaging techniques, which do not require ECG gating or breath-holding can be used clinically; however, some of these techniques may sacrifice spatial and/or temporal resolution [35,64,113]. Thus, there is a growing interest in free-breathing and self-gated approaches that can acquire images with excellent quality that have high temporal and spatial resolution. A recent study has used a breath-held cardiac self-gated spiral technique to quantify coronary artery vasodilation [61]. To date, no studies have explored the use of free-breathing cardiac and respiratory self-gated golden angle spiral trajectories for the evaluation of cardiac anatomy and function.

Despite a number of recent advances, there are still several limitations to be overcome. Firstly, for imaging at 3T, bSSFP sequences typically require frequency-scouts and careful shimming to avoid off-resonance artifacts such as banding artifact and thus may be less robust for automatic free breathing acquisition. To address this issue, our SPiral Acquisition with Respiratory correction and Cardiac Self-gating (SPARCS) utilized a spoiled gradient echo pulse sequence (spoiled-GRE) with data acquired using a single spiral interleaf rotated by the golden-angle (137.51°) in time. While spiral pulse sequences are sensitive to blurring from off-resonance, short spiral readout durations can be used to mitigate this issue. Self-gating approaches usually require careful selection of receive coil elements to obtain self-gating signals as each coil has different sensitivity to cardiac motion and respiratory motion. Here, the cardiac self-gating signal was extracted using PCA on a gridded 8×8 central region of *k*-space for each spiral, which eliminates the process of selecting coils that contribute significant aliasing artifacts in the heart region. This also improves the performance of coil compression and image reconstruction. Finally, as it is inefficient to discard data acquired at different respiratory phases, we utilized rigid registration of the data from each heartbeat to correct the breathing motion to obtain 100% data acquisition efficiency. Images were reconstructed with a rigid-motion compensated L+S technique [71]. SPARCS was designed to provide whole heart coverage with clinically relevant spatial (1.25 mm × 1.25 mm) and temporal (< 40 ms) resolution from a self-gated free breathing acquisition of less than 90 seconds.

3.2 Methods

3.2.1 Image acquisition

3.2.1.1 Spoiled-GRE at 3T

At 3T, we used a spoiled-GRE readout. Data were acquired continuously using a spiral trajectory rotated by the golden angle (137.5°).

3.2.1.2 bSSFP at 1.5T

At 1.5T, we used a balanced steady-state free precession (bSSFP) readout. Data were acquired continuously using a spiral trajectory rotated by the golden angle (137.5°).

3.2.2 Cardiac self-gating

The automatic pipeline that we developed for cardiac self-gating is shown in Figure 3.1. Self-gating cardiac signals were determined by gridding an 8×8 fully sampled central region of *k*-space for each spiral interleaf for all receiver coils (Figure 3.1(a)), followed by low-pass temporal filtering to eliminate the high frequency component caused by the golden-angle sampling pattern. Next, PCA was performed on this data. The first 5 temporal-basis functions, which typically explained greater than 90% of total variance, were used for further processing (Figure 3.1(b)). To extract and determine the cardiac self-gating signal, a band-pass filter with a passband from 0.5 Hz to 2 Hz was applied to the 5 temporal-basis functions. Then, frequency spectrum analysis was used to find the cardiac motion-related component by determining which basis function had the highest

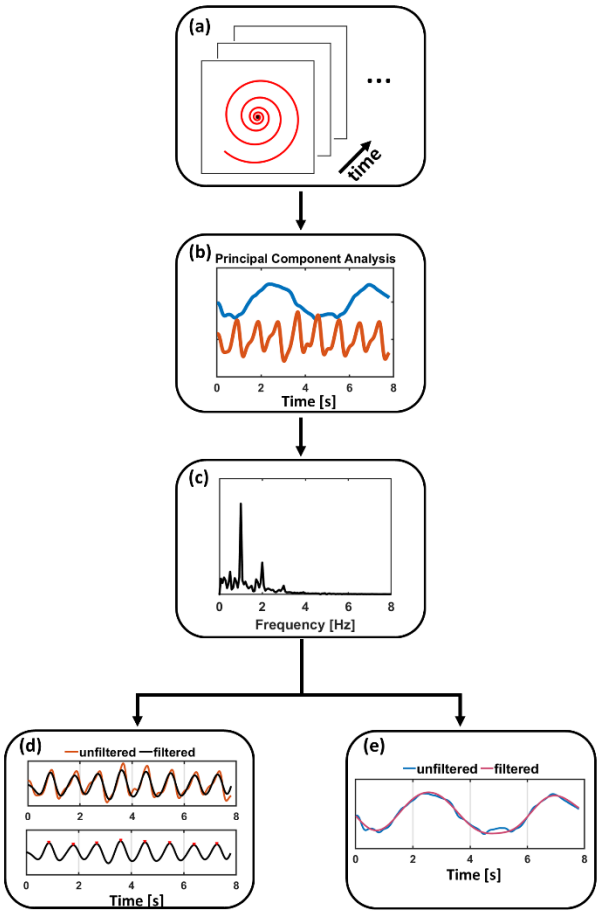

Figure 3.1 Pipeline of cardiac self-gating. (a) In the first step, the 8x8 center region of k-space is gridded across all coils through time. (b) Principal component analysis is then performed across this data to derive temporal-basis functions. (c) Frequency spectrum analysis is performed to separate the cardiac and respiratory components. (d) Extracted filtered cardiac motion component and peak detection is performed to detect the cardiac triggers. (e) A respiratory motion component can also be derived and used for self-gating as alternative to rigid registration.

amplitude in the cardiac motion frequency range (Figure 3.1(c)). Finally, the cardiac self-gating triggers were extracted by performing peak detection on this filtered temporal-basis function. To exclude potential artifactual peaks that are unrelated to cardiac motion, a signal threshold was set by taking the mean of all the peaks and troughs (Figure 3.1(d)). Since the cardiac trigger from self-gating signal is based on the *k*-space center intensity, rather than on the physiological ECG signal, the triggers derived from SPARCS are typically not at the same time as the triggers derived from an ECG signal, as shown in Figure 3.2.

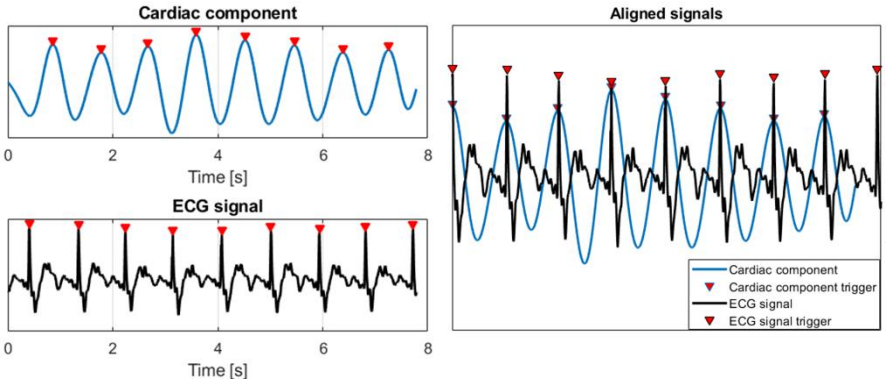

Figure 3.2 Comparison of ECG trigger and "self-gated" cardiac trigger. Triggers are aligned on the right figure to make a clear visual comparison.

However, as the signal fluctuation varies reproducibly between systole and diastole, the SPARCS gating signal is consistent from beat to beat. Thus, the R-R interval of the SPARCS gating signal and the ECG signal were very similar. As the heart shape varies between different slices the exact position of the trigger within the cardiac cycle may be different at the different slice locations. To compare gating data across all subjects and slice positions, we compared the recorded ECG R-R interval length versus the cardiac cycle length as determined by the time interval between subsequent SPARCS triggers. When determining ejection fraction (EF), end-diastole and end-systole were determined visually for each slice, and the images from each slice were aligned. This is a limitation of all non-ECG gated techniques including non-gated free breathing techniques. A respiratory gating signal can also be obtained from the PCA data using a band-pass filter with a frequency range from 0.05 Hz to 0.5 Hz (Figure 3.1(e)). While in SPARCS we use registration to correct for respiratory motion, this PCA respiratory gating signal, or the

displacements derived from registration, could be used for self-gating to reject data that is outside of a desired "self-gating" window.

Once the cardiac triggers were detected, the data were retrospectively binned to a fixed number of phases across the cardiac cycle. This number of phases was determined by dividing the average cardiac trigger interval (cardiac cycle length) by a fixed temporal resolution of 39 ms, corresponding to 5 spiral interleaves (Figure 3.3(a)). This resulted in 25-35 cardiac phases depending on the average length of the cardiac cycle.

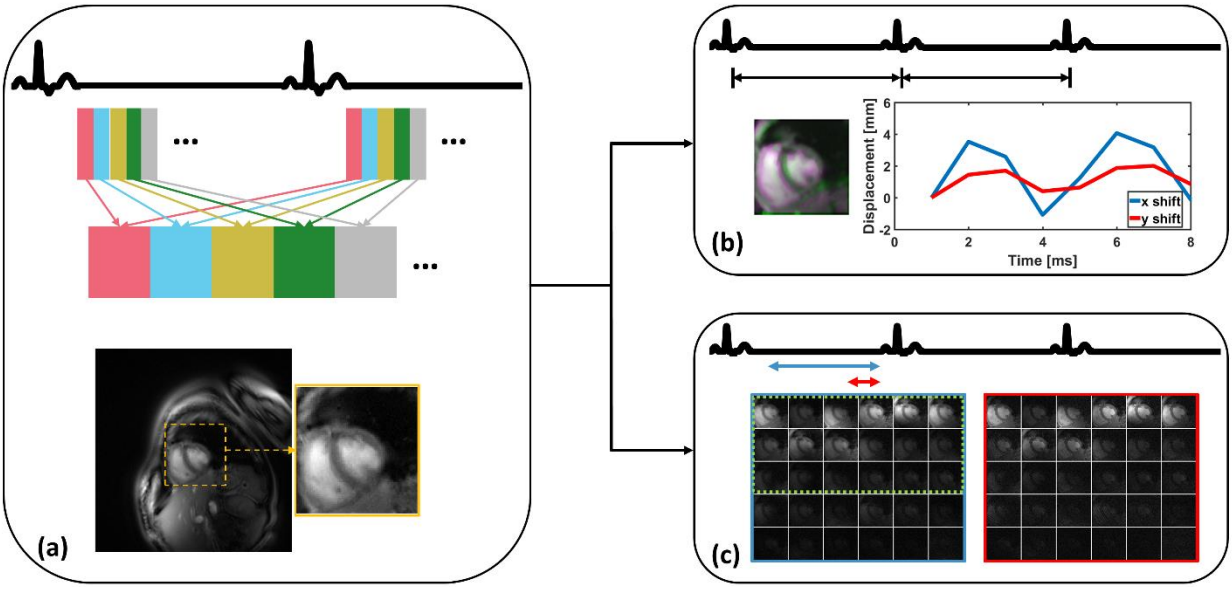

Figure 3.3 Pipeline of respiratory motion correction. In the first step (a), retrospective cardiac binning of the data across multiple R-R intervals, was performed so that the heart could be located based on the variation in signal intensity due to cardiac motion throughout the cardiac cycle. Once the heart ROI was selected, further processing used only this defined ROI and data were averaged over part of individual heartbeats. In the second step (b), by using all of the spiral interleafs for each heartbeat, a single static image was created for each heartbeat and these images were registered to determine the respiratory motion. For the automatic coil selection (c), a reference image (blue) was reconstructed from a single heartbeat using a large temporal window and an aliased image (red) was reconstructed using a small temporal window. The images reconstructed from these two temporal windows provided an assessment of the artifact power, and coils with high SNR and low artifact power (circled by green dashed line) were selected appropriately.

3.2.3 Respiratory motion correction

We developed a fully automated strategy [32] to detect an 80×80 pixel ROI containing the heart. Using a NUFFT reconstruction [39] of the retrospectively binned cardiac data, the heart was automatically detected based on the fact that, in cine imaging, the heart region has the largest

magnitude changes in signal intensity due to cardiac motion. Thus, the ROI containing the heart was automatically detected by finding the largest connected region of high standard deviation on a standard deviation map, whose signal intensity was calculated from the whole dynamic dataset (Figure 3.3(a)).

To correct the respiratory motion, it was assumed that the respiratory position does not vary considerably during each R-R interval. Based on this assumption, the k-space data over each R-R interval was combined to create a static image for each heartbeat (Figure 3.3(b)). Rigid registration was performed over the heart ROI to determine the in-plane displacements required to compensate for the bulk changes in heart position resulting from respiratory motion. While breathing results in non-rigid motion of structures of the chest, the motion of a small square ROI around the heart on a cardiac gated short-axis image can be reasonably approximated by in-plane rigid motion in the head-foot and anterior-posterior directions [32]. Rigid translational registration was performed by using mutual information as a metric to determine the rigid transformation from the source image to that of the target image [99] (Figure 3.3(b)).

Images from all frames were first registered to the image from the first acquired heartbeat to derive the relative displacements due to respiratory motion. The end-expiration state image was then determined by finding the most positive head-foot and anterior-posterior shift along the curve. The displacement information was adjusted by treating the end-expiration image as the target image, and this displacement was used to derive the appropriate k-space linear phase shifts to register the heart. The difference between registering the images to end-inspiration and to end-expiration can be appreciated in Figure 3.4. These linear phase shifts derived from each R-R

interval combined images were applied to the acquired raw k-space data for each frame within that R-R interval as previously described [32].

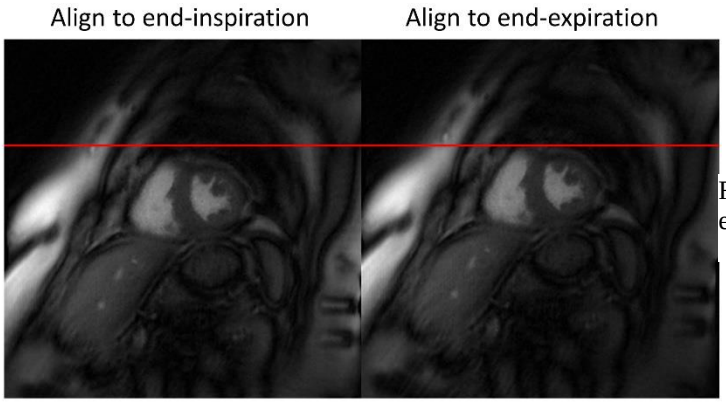

Figure 3.4 Comparison of rigid registration to end-inspiration and end-expiration.

3.2.4 Automatic coil selection

Unlike in Cartesian imaging where the aliasing manifests as wrapping in the phase encoding direction, for spiral imaging aliasing appears as swirling artifacts on the opposite side of the unsupported portion of the field of view (FOV), which could affect image quality within the heart region. Therefore, we developed a strategy to automatically select coils based on a spiral aliasing artifact ratio within the automatically detected heart ROI (Figure 3.3(c)). Our method was inspired by several studies [114,115] that have developed techniques for automatic coil selection to reduce streaking artifacts in radial acquisitions. By using golden-angle sampling, increasing the temporal window for reconstruction results in an increase in the supported FOV such that a completely unaliased image (Ref_{heart}) can be recovered. By comparing this to an image that does not support the whole FOV (i.e. smaller temporal window, Img_{heart}), we can characterize the aliasing pattern and assess its impact on the desired FOV. An artifact ratio was defined over the heart ROI for the kth coil (r_k) as:

$$r_k = \frac{\|Ref_{heart}(k) - const \times Img_{heart}(k)\|_F}{\|Ref_{heart}(k)\|_F},\ k \in [1, N], \tag{3.1}$$

where N is the number of coils, Ref_{heart} is an aliasing-free multi-coil magnitude (reference) image that was reconstructed by using 100 continuous-acquired spirals, Img_{heart} indicates an under-

sampled multi-coil magnitude image with aliasing artifacts reconstructed using only 30 spirals, and $const$ is a constant value calculated based on the energy difference of the reference and aliasing images, which is the ratio between the number of spirals that were used to generate the reference and under-sampled images. $\|*\|_F$ indicates the Frobenius-norm. To eliminate coils which predominantly contribute aliasing artifacts over the heart region, while still having an adequate number of coils for parallel imaging, coils with an artifact ratio lower than 0.3 were retained. This threshold was chosen by screening the selection of coils in 10 subjects. After coil selection, we used PCA-based coil compression to decrease the number of coils to reduce computations during reconstruction.

3.2.5 Image reconstruction

Images were reconstructed using low-rank plus sparse decomposition [71] as shown in Equation 1.5. Temporal finite difference was used as the sparsifying transform. This method can reconstruct highly accelerated dynamic MRI datasets by separating the background static-information from the dynamic information. In the reconstruction, the iterative SENSE algorithm [116] was adopted to enforce joint multi-coil low-rank (L) and sparsity (S) simultaneously to exploit inter-coil correlations. Data compression in the L model was performed by truncating the singular value decomposition (SVD) representation of the dynamic image series while in the S model it was done by discarding low-value coefficients in the temporal total variation domain. Coil sensitivity maps were computed from the temporal average of binned data using the adaptive coil combination technique [100]. Reconstruction parameters were chosen based on providing images with adequate reduction in aliasing artifacts with minimal visual temporal blurring of the endocardial border. To determine appropriate values for λ_L and λ_S, SPARCS cine data from 3 subjects were reconstructed with λ_L and λ_S varied over a range from 0.000001 to 0.1. An

experienced cardiologist chose the combination of λ_L and λ_S which resulted in images with reduced aliasing artifacts and no obvious temporal blurring. The parameters λ_L of 0.01 and λ_S of 0.00001 were chosen and used to reconstruct all datasets.

3.2.6 In-vivo study

Scanning was performed on a 3T scanner (MAGNETOM Prisma or Skyra, Siemens Healthineers, Erlangen, Germany) at the University of Virginia Medical Center. Continuous spiral cine imaging was performed in 45 subjects. The subjects included 37 healthy volunteers and 8 patients undergoing clinical CMR studies. Written informed consent was obtained from all subjects, and imaging studies were performed under institutional review board (IRB) approved protocols. Image datasets were acquired using the standard body phased-array RF coil. Pulse sequence parameters included: FOV = 320 mm, TR = 7.8 ms, TE = 1 ms, voxel size = 1.25×1.25 mm2, slice thickness = 8 mm, flip angle = 15°. A dual density (DD) spiral readout trajectory was rotated by the golden angle between subsequent TRs for data acquisition. The DD spiral had a fermi-function transition region with a *k*-space density of 0.2 times Nyquist for the first 20% of the trajectory and an ending density of 0.02 times Nyquist [117]. This density was chosen such that the center of *k*-space would be approximately fully sampled and the outer-region of *k*-space would have a maximum acceleration factor of approximately 8x for the combination of 5 spiral interleaves (39 ms temporal resolution). Data were acquired for 8 seconds per slice. In the same scan, the clinical "gold-standard" breath-hold ECG-gated bSSFP Cartesian cine images were also acquired for further comparison.

Scanning was performed on a 1.5T scanner (MAGNETOM Avanto or Aera, Siemens Healthineers, Erlangen, Germany) at the University of Virginia Medical Center. Free breathing continuous spiral cine imaging with bSSFP readouts were acquired with 5 healthy volunteers using

the standard body phased-array RF coil. Pulse sequence parameters included: FOV = 320 mm, TR = 4.85 ms, TE = 1.05 ms, voxel size = 1.5×1.5 mm^2, slice thickness = 8 mm, flip angle = 60°. A linear variable density (VD) spiral readout trajectory was rotated by the golden angle between subsequent TRs for data acquisition. The VD spiral had a starting density of 0.01875 times Nyquist and an ending density of 0.00469 times Nyquist. This density was chosen such that the center of *k*-space and the outer-region of *k*-space would have density as 0.15 times Nyquist and 0.0375 times Nyquist for the combination of 8 spiral interleaves (39 ms temporal resolution). In the same scan, the clinical "gold-standard" breath-hold ECG-gated bSSFP Cartesian cine images were also acquired for further comparison.

3.2.7 Image analysis

For 3T experiments, continuously acquired spiral data were obtained at a single short-axis location for 32 subjects. During the acquisition, the ECG signal was also recorded. The R-R interval length from the ECG signal and extracted cardiac trigger from SPARCS were compared using Bland-Altman [118] and linear regression plots. Images were reconstructed from 8 seconds worth of data (1000 spirals) using NUFFT and L+S techniques. The first 200 spirals in the acquired data were discarded to allow the signal to achieve steady state. To evaluate quantification of LVEF, slices covering the whole heart in short-axis were collected in 13 subjects including: 10 healthy volunteers and 3 clinical subjects. EF was determined by manual tracing of the endocardial borders by an experienced cardiologist. The calculated LVEF was compared to that from the standard clinical breath-hold ECG gated bSSFP sequence. Image quality for all datasets was assessed by 2 experienced cardiologists blinded to the reconstruction technique. Image quality was evaluated on a 5-point scale ranging from 1 (poor and not usable) to 5 (clinically excellent). A score of 3 would be clinically acceptable, but with some artifacts. Comparison between the scores from the different

techniques were compared using Friedman's test and Wilcoxon signed-rank tests for the comparisons between individual reconstruction techniques. The EF comparison between the techniques was performed using a two-way ANOVA analysis with Tukey's Studentized Range test to correct for multiple comparisons.

For 1.5T experiments, image quality for all datasets was assessed by an experienced cardiologist blinded to the reconstruction technique, with the same standard as 3T experiments. Comparison between the scores from the proposed technique and reference was using paired *t*-test. All statistical analysis was performed using SAS software 9.4 (SAS Institute Inc., Cary, NC).

3.3 Results

3.3.1 3T results

3.3.1.2 Cardiac self-gating

R-R interval length was compared between the recorded ECG signals and the extracted cardiac "self-gated" trigger signals as shown in Figure 3.5.

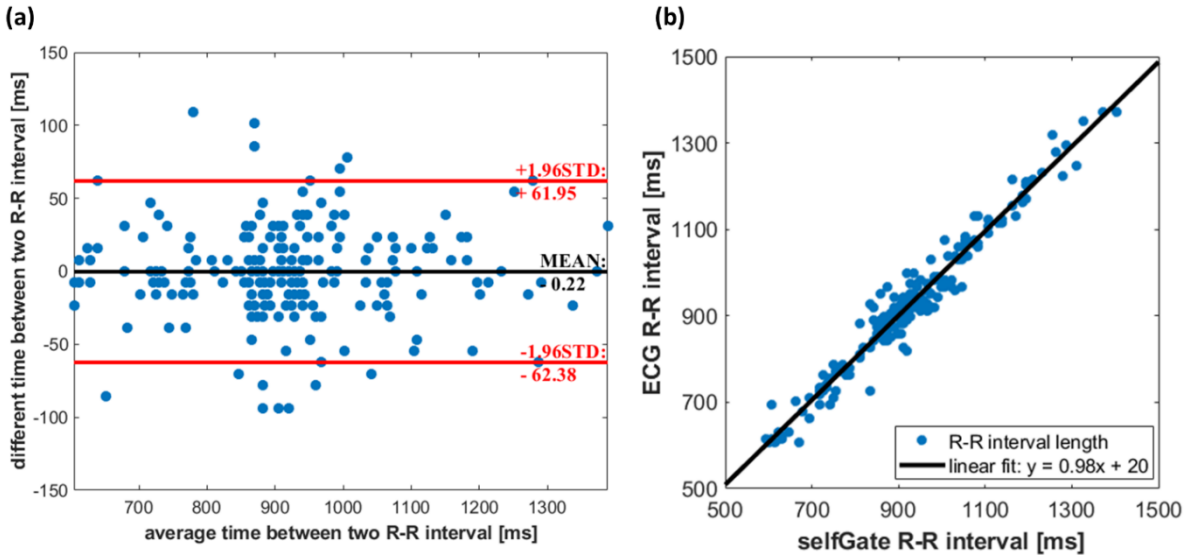

Figure 3.5 Cardiac gating consistency. (a) Bland-Altman plot indicates a non-significant bias of -0.22 ms for the R-R interval length difference between self-gated signals and ECG signals across all the subjects. (b) There is a strong positive correlation relationship (R^2=0.96) between self-gated and ECG R-R interval lengths.

The mean difference between the ECG and self-gating cardiac cycle lengths for the patients with measured ECG data was -0.22 ms, with a 95% confidence interval of 61.95 ms to -62.38 ms. There was a good correlation, $R^2 = 0.96$, between the R-R interval length from ECG and self-gated cardiac signals without a significant bias (p = 0.92, paired sample *t*-test).

As the self-gated cardiac trigger and ECG signals performed similarly, the self-gating strategy provides a reasonable surrogate. While ECG gating techniques have improved significantly, ECG gating can sometimes be unreliable at 3T, particularly in patients with high BMI (as shown in Figure 3.6).

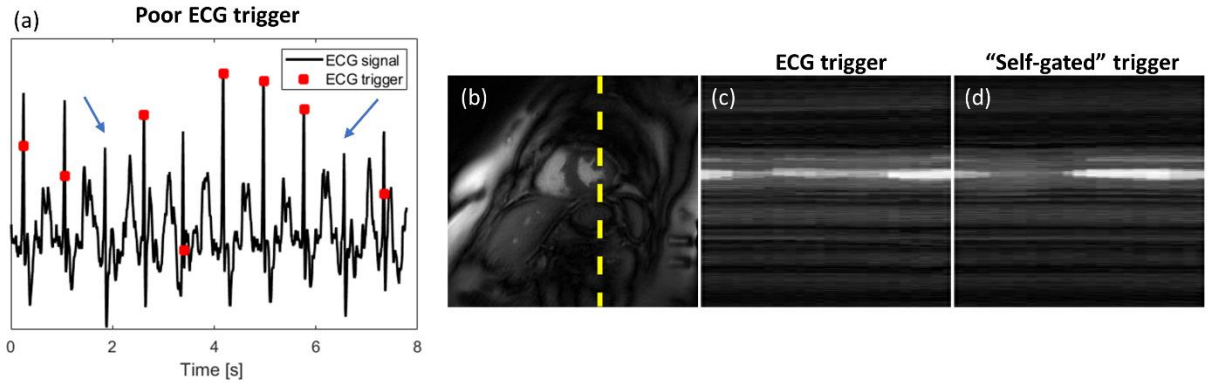

Figure 3.6 A poor ECG trigger example from a clinical patient. This subject had a BMI of 33.6 and was undergoing clinical evaluation for acute myocarditis. (a) The ECG tracing was exported from the scanner. Missed triggers are shown as blue arrows. X-t profiles of cine movies reconstructed using the ECG triggers (c) and "self-gated" triggers (d) are shown. The dashed line in (b) corresponds to the x position.

3.3.1.2 Respiratory motion correction

Figure 3.7 shows the rigid registration performance from one representative subject. After the heart region was automatically detected (Figure 3.7(a)), images from each self-gated cardiac interval were registered to correct for respiratory motion. The anterior-posterior (x) and head-foot (y) displacements extracted from rigid registration are plotted in Figure 3.7(b). The registration performance can be seen by comparing the x-t and y-t (Figure 3.7(d)) profiles before and after rigid registration, where the crossing lines on x and y directions are shown in Figure 3.7(c). After registration, both x-t and y-t profiles (Figure 3.7(d)) are sharper and less corrupted by respiratory motion.

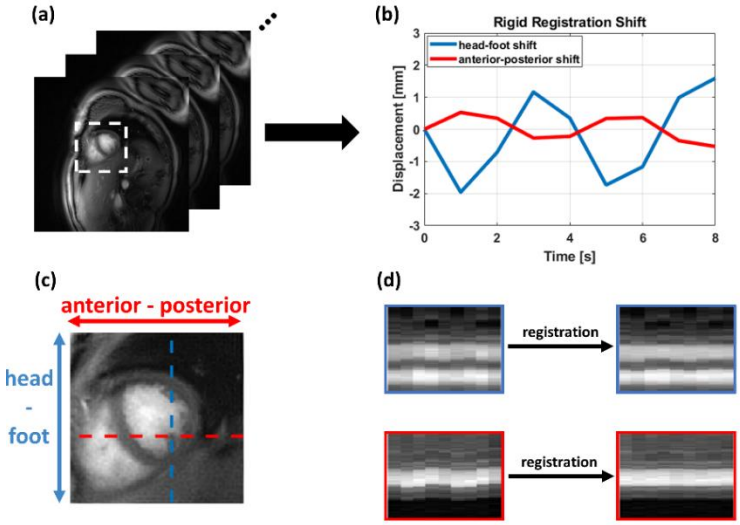

Figure 3.7 Motion correction performance in a representative subject. (a) A static image was reconstructed from each heartbeat to generate the images used for respiratory motion compensation. (b) The rigid registration displacement in x (anterior-posterior: A-P) and y (head-foot: H-F) directions was determined and used to correct the respiratory position. X-t and Y-t profiles before and after registration in the H-F and A-P directions (c) are shown in (d). The heart borders are more closely aligned following respiratory motion correction.

3.3.1.3 Automatic coil selection

Figure 3.8 demonstrates the automatic coil selection results. Coil images in a region around the heart are shown in Figure 3.9. As expected, the coils that have a high SNR and low aliasing in the heart region rank higher. With a threshold of artifact energy of 0.3, coils whose images are circled in green were retained while the ones in red were discarded. Figure 3.8(a) and 3.8(b) show the NUFFT image results before and after automatic coil selection, respectively. The difference image of these is shown in Figure 3.8(c), with a 10-fold scaling factor. In this particular case, the aliasing artifacts caused by remote coils started from the bottom right (red arrow) and extended all the way into the heart region. Automatic coil selection significantly reduced aliasing artifacts.

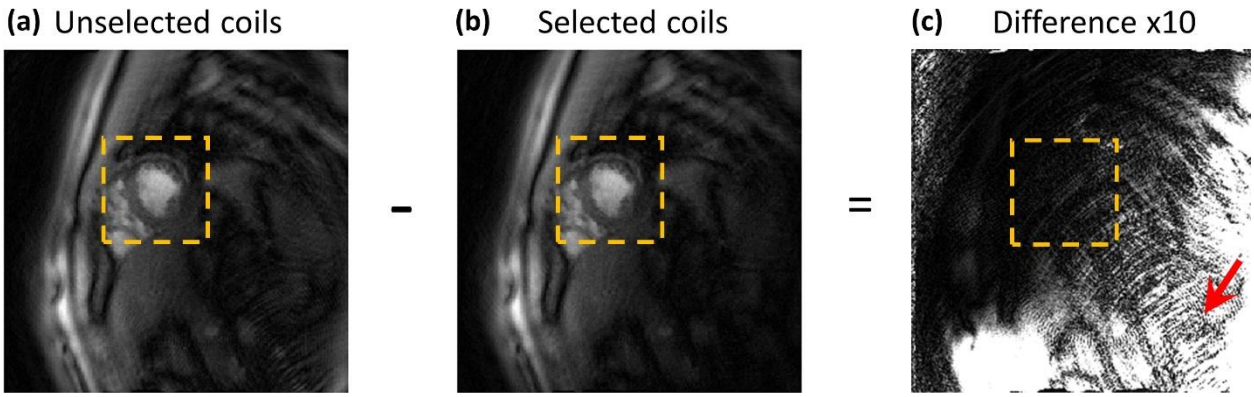

Figure 3.8 Automatic coil selection. (a) and (b) show the reconstructed images before and after the proposed coil selection method, respectively. (c) is the difference image between (a) and (b), with 10-fold scaling to better visualize aliasing artifacts. The red arrow indicates aliasing caused by remote coils. correction.

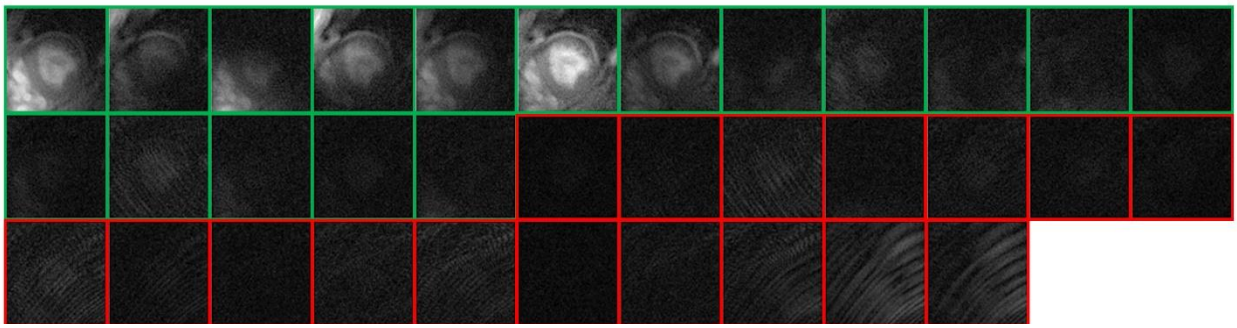

Figure 3.9 Coil images in a region around the heart, with the coils ranked from lowest to highest artifact energy from the top left to the bottom right. With a threshold of artifact energy of 0.3, coils whose images are circled in green were retained while the ones in red were discarded.

3.3.1.4 Evaluation of cine images

Figure 3.10 shows reconstructed short-axis cine images from a healthy volunteer. The first row (Figure 3.10(a-c)) shows cine images reconstructed with NUFFT while the second row (Figure 3.10(d-f)) shows the L+S reconstructed images. The third row (Figure 3.10(g-i)) shows the clinically used breath-hold ECG-gated bSSFP images. End-diastolic and end-systolic images are shown in the first and second columns respectively. X-t profiles for the reconstructed images along

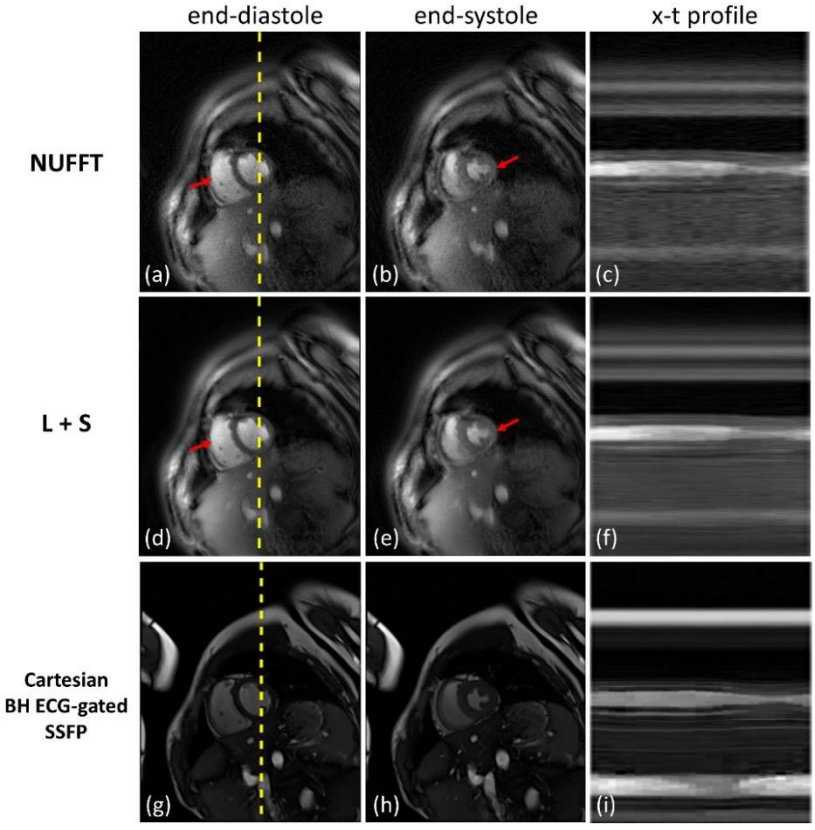

Figure 3.10 Short axis SPARCS images from a healthy volunteer. The first and second rows show SPARCS reconstructed images using NUFFT and L+S, respectively. The third row shows the clinically used breath-hold ECG-gated bSSFP images for comparison. End diastolic and end systolic images are shown in the first and second columns, respectively, and x-t profiles are shown in the last column. X positions are indicated as dashed yellow lines in end-diastolic images. Red arrows indicate aliasing artifacts that are obvious in NUFFT images but are reduced by the L+S technique. The image-quality scores for this subject from 2 cardiologists were: 4 and 3 for SPARCS NUFFT images; 5 and 4.5 for SPARCS L+S images; and 5 and 5 for breath-hold ECG-gated bSSFP images.

the profile denoted by the dashed line in Figures 3.10(a,d,g) show preserved temporal fidelity of the SPARCS technique.

Figure 3.11 demonstrates images from a subject in the patient group. In this clinical subject, mild susceptibility artifacts are seen in the bSSFP images (indicated by red arrows) in Figure 3.11(g-i). As the NUFFT technique reconstructs each frame independently, it is free of temporal blurring between frames, but less effective at reducing aliasing artifacts (e.g., red arrows in Figure 3.11) as compared to the L+S reconstruction. The X-t profiles from the L+S reconstruction show the reduction of residual aliasing artifacts without introducing significant visual temporal blurring as compared to NUFFT.

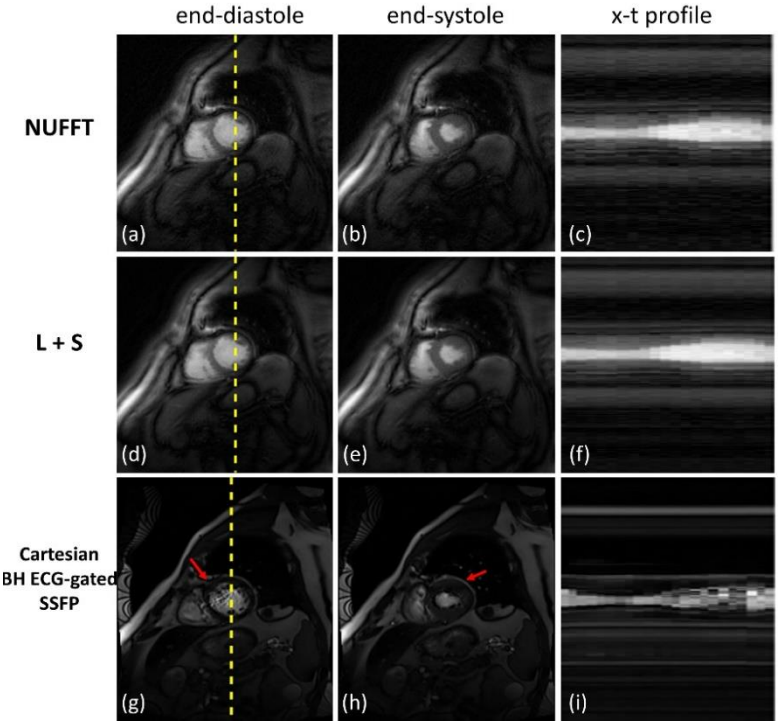

Figure 3.11 Short axis SPARCS images from a clinical patient subject. The first and second rows show SPARCS reconstructed images using NUFFT and L+S, respectively. The third row shows the clinically used breath-hold ECG-gated bSSFP images for comparison. End-diastolic and end-systolic images are shown in the first and second columns, respectively, and x-t profiles are shown in the last column. X positions are indicated as dashed yellow lines in end-diastolic images. Red arrows indicate susceptibility artifacts that often occur in clinical bSSFP images. The image-quality scores for this subject from 2 cardiologists were: 4 and 3.5 for SPARCS NUFFT images; 5 and 4.5 for SPARCS L+S images; and 3 and 3.5 for breath-hold ECG-gated bSSFP images.

Figure 3.12 shows the L+S reconstructed images from one subject with 10 slices covering the left ventricle. Figure 3.12(a) corresponds to end-diastolic frames and Figure 3.12(b) are end-systolic frame images.

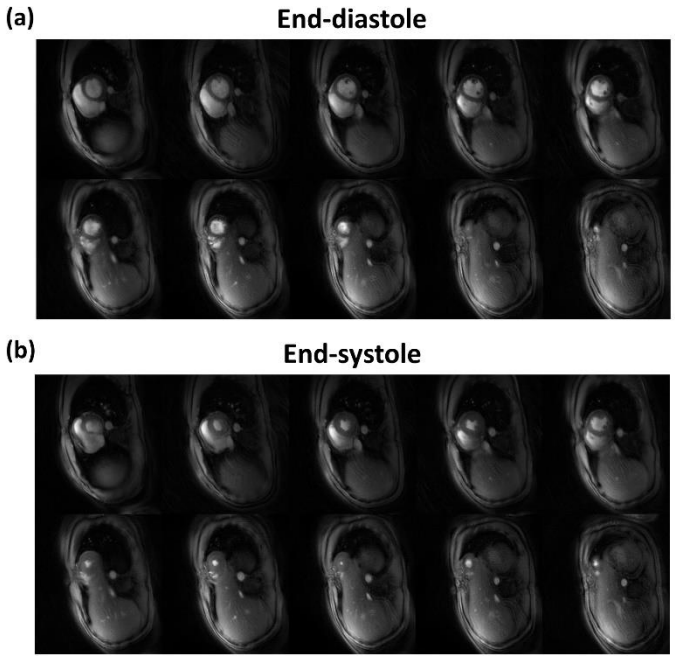

Figure 3.12 Whole-heart reconstruction results. (a) The top 2 rows of images are L+S diastolic frames across all slices. (b) The bottom 2 rows of images are L+S systolic frames across all slices.

Image-quality scores (N = 42) from the 2 cardiologists are shown in Figure 3.13. Here, the 3 subjects that were used to tune L+S reconstruction parameters were excluded. The mean (± standard deviation) image-quality scores of SPARCS NUFFT, SPARCS L+S and breath-hold ECG-gated bSSFP images were 3.2 (± 0.7), 4.0 (± 0.7) and 4.5 (± 0.6). The L+S reconstruction was graded significantly higher than the SPARCS NUFFT reconstruction ($p < 0.001$), and breath-hold ECG-gated bSSFP was graded significantly higher than SPARCS NUFFT and L+S reconstruction ($p < 0.001$), which might due to the difference contrast between GRE and bSSFP readouts. Given the relatively short readout duration per interleaf, the SPARCS images had minimal blurring or signal dropout artifacts due to off-resonance. Fine trabeculations were clearly visualized in the right and left ventricles in the SPARCS images.

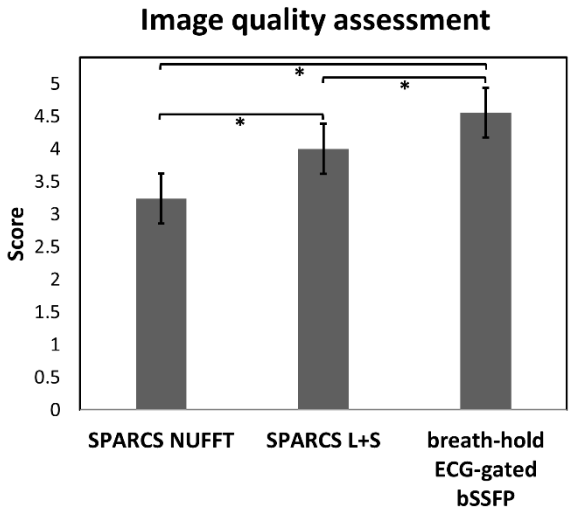

Figure 3.13 Blinded image quality scores for all subjects. The bar plot shows the scores for SPARCS images using NUFFT and L+S, as well as breath-hold ECG-gated bSSFP images, graded in a blinded fashion by 2 cardiologists. * indicates a significant difference ($p < 0.001$).

Across all studies with whole ventricular data (N = 13), the mean (± standard deviation) LVEF for NUFFT and L+S were 58.5 (± 7.6) and 57.3 (± 7.9), respectively, for the SPARCS technique as compared to 58.3 (± 7.7) for the standard bSSFP cine images. A Bland-Altman plot comparing EF between Cartesian bSSFP images and SPARCS NUFFT spiral images is shown in Figure 3.14(a), and one comparing Cartesian bSSFP images and SPARCS L+S spiral images is shown in Figure 3.14(b). A blocked ANOVA test showed no significant difference among the 3 groups (p = 0.09), demonstrating the accuracy of calculating LVEF using the proposed SPARCS strategy.

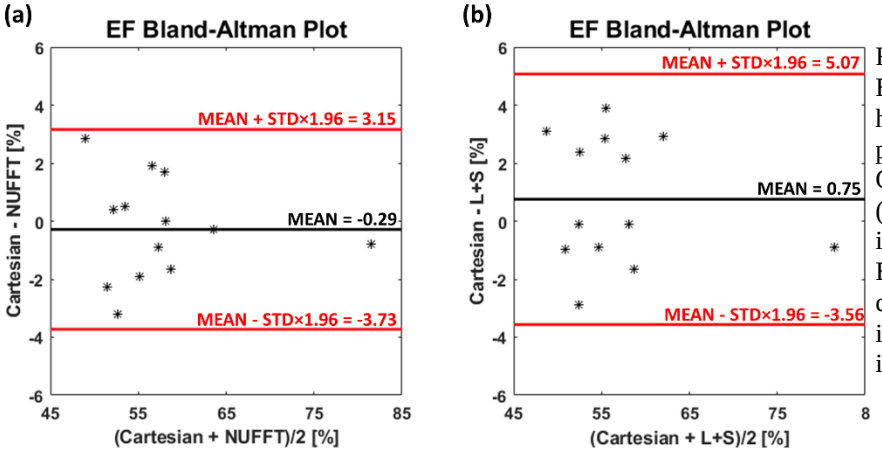

Figure 3.14 Bland-Altman plots of EF for the subjects with whole-heart coverage. (a) Bland-Altman plot of EF calculated from Cartesian bSSFP image results (Cartesian) and SPARCS NUFFT image results (NUFFT). (b) Bland-Altman plot of EF calculated from Cartesian bSSFP image results and SPARCS L+S image results (L+S).

3.3.2 1.5T results

Figure 3.15 demonstrates the reconstruction results of three healthy volunteers. The end-diastolic and end-systolic frames show comparable image quality between the clinically used breath-hold ECG-gated Cartesian bSSFP results and the proposed SPARCS bSSFP images. X-t profiles indicate preserved temporal fidelity of the SPARCS bSSFP technique.

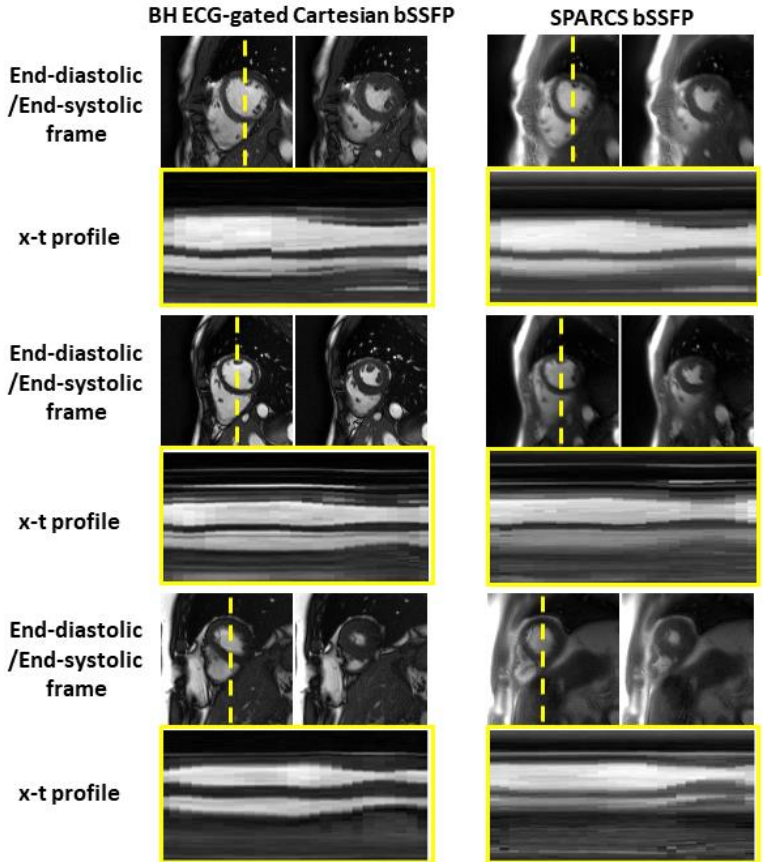

Figure 3.15 Short axis SPARCS images from three subjects. The first row shows the clinically used breath-hold ECG-gated bSSFP images, while the second row shows SPARCS bSSFP results. Both end-diastolic/end-systolic frames and x-t profiles are shown. The dashed line indicates the location where the x-t profiles are derived.

Figure 3.16 shows the heart region reconstruction images from one subject with 8 slices covering the left ventricle. The clinically used breath-hold ECG-gated Cartesian bSSFP results are shown in top two rows while SPARCS bSSFP results are shown in bottom two rows. SPARCS bSSFP images show comparable image quality with clinical "gold-standard". As compared to the standard breath-held Cartesian cine acquisition, SPARCS was relatively insensitive to breathing

motion (slice 5 in Figure 3.16). The image grades for BH ECG-gated Cartesian bSSFP and SPARCS bSSFP are 4.63 ± 0.61 and 4.57 ± 0.37, with no significant difference ($p = 0.75$).

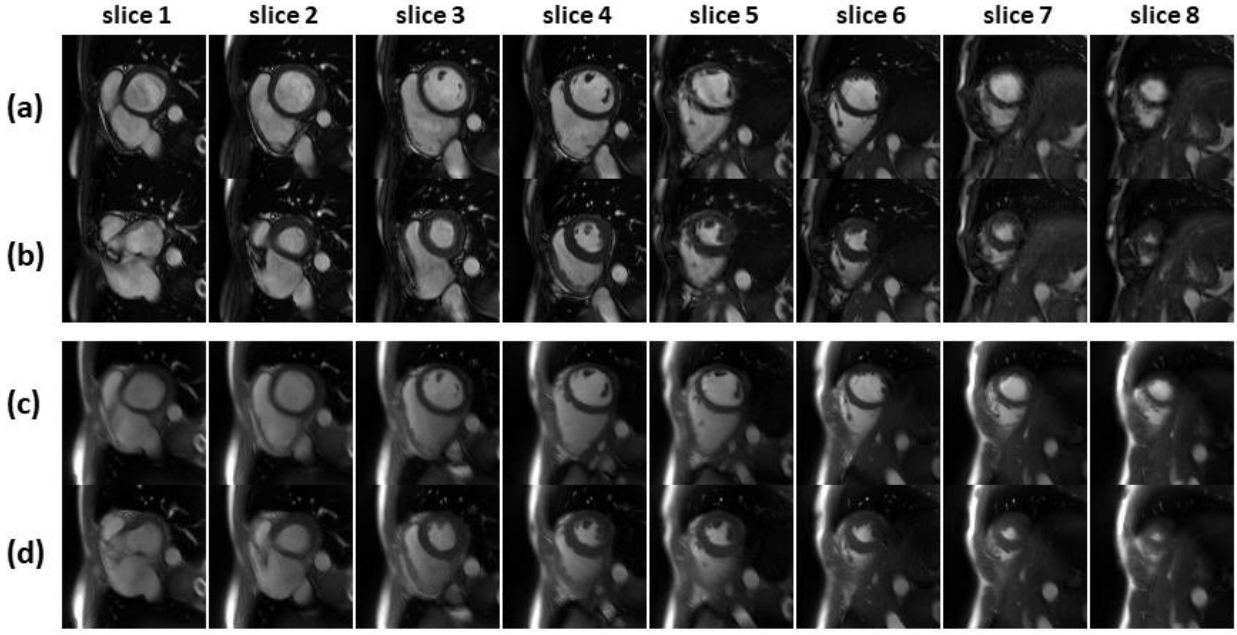

Figure 3.16 Whole-heart reconstruction results. Top two rows (a,b) show the clinically used breath-hold ECG-gated Cartesian bSSFP results while the bottom two rows (c,d) show SPARCS bSSFP results. (a,c) corresponds to end-diastolic frames and (b,d) are end-systolic frame images.

3.4 Discussion

In this work a free-breathing, continuous-acquisition, respiratory and cardiac self-gated, golden-angle spiral-cine strategy (SPARCS) was proposed and developed. The method used the 8×8 *k*-space center region from the acquired data to derive a cardiac trigger signal without the need for ECG gating.

To enable free-breathing acquisition with 100% sampling efficiency, a rigid registration strategy was implemented to correct respiratory motion between heartbeats. While currently there are more complex techniques for non-rigid registration[54,98], their performance is sensitive to image quality related factors, and their implementation for non-Cartesian trajectories significantly increases reconstruction time and complexity. Since most cardiac motion caused by breathing is in the head-foot and anterior-posterior directions, a rigid registration can be used. We have

previously demonstrated the robustness of this motion-correction strategy for myocardial perfusion imaging [32].

As SPARCS registers data acquired at different respiratory phases, residual uncorrected respiratory motion could cause some loss of spatial resolution. This is true of all techniques which achieve 100% navigator efficiency using registration. Our approach assumes that respiratory motion within each heartbeat is relatively small. The difference in respiratory position in the head-foot direction between beats across all subjects typically fell within a ± 2-4 mm window, which is in the range of typical diaphragmatic navigator acceptance windows of 4-8 mm [42,119]. Correction of residual respiratory motion with each heartbeat may be feasible using a sliding window approach to assess the respiratory position throughout the cardiac cycle. However, such an algorithm would have to account for changes in the heart position due to cardiac contraction and would add additional complexity to the reconstruction. Blurring due to residual respiratory motion could be a disadvantage of self-gating techniques as compared to real-time techniques and requires further investigation. This strategy also does not account for through-plane motion or potential differences in cardiac morphology between inspiration and expiration. As the respiratory phase of each heartbeat is known, discordant data could be rejected either using a self-gating window as we have used for free-breathing T_1 mapping [120], or based on an image correlation metric as has been used for free-breathing LGE imaging [121]. The trade-off for rejecting data would be a reduction in acquisition efficiency. As the R-R interval duration for each heartbeat is also known, heartbeats with significantly different durations can also be rejected, again at the cost of acquisition efficiency. At relatively low acceleration factors (2-3x), non-Cartesian SPIRiT [68] and non-Cartesian SENSE [66] perform well for spiral imaging. For more highly accelerated spiral techniques, compressed sensing approaches have been shown to improve reconstruction performance [117]. The L+S

reconstruction method can provide a decomposition of low-rank and sparsity components to separate background and dynamic components in an image. The L component captures static and periodic motion in the background among cardiac phases, while the S component contains the dynamic cardiac motion information. Since the background has been suppressed, the S component has a sparser representation than the original matrix [71]. By exploiting the spatial and temporal correlation of the dynamic image series with an iterative SENSE implementation, the L+S method offers an efficient and robust reconstruction. L+S reconstruction with inappropriate regularization parameters could suffer from temporal blurring. We chose the smallest regularization parameters for the L+S reconstruction that visually reduced spatial blurring without obvious loss of temporal fidelity. Furthermore, we intentionally compared L+S to NUFFT so that we could directly assess the effects of temporal regularization on the temporal fidelity of the L+S reconstruction. Our assessment of LVEF with L+S reconstruction as compared to NUFFT reconstruction of the SPARCS data and the breath-held cine bSSFP data demonstrates that the respiratory motion correction and temporal regularization do not result in significant biases in determination of the LVEF. This is important as LVEF remains a key parameter for clinical decision making. However, we note that some reduction in spatial resolution due to residual respiratory motion may not greatly impact the measured EF. The comparison of EF measurements between SPARCS and the "gold-standard" Cartesian method had no significant bias, and clinically acceptable limits of agreement. Prior studies [122,123] have demonstrated similar limits of agreement for intra-observer, inter-study EF measurements as -5.19 to 6.33.

Although bSSFP sequences are typically used for cine imaging due to improved contrast to noise ratio, a gradient echo strategy may have advantages for simplifying 3T cine imaging. As the spiral-trajectory implementation has a relatively long TR, there is more time for inflow-

enhancement of the LV blood pool resulting in a contrast which is similar to Cartesian bSSFP imaging rather than that seen with short-TR Cartesian spoiled-GRE imaging. As the sequence is spoiled GRE-based rather than SSFP-based, a frequency scout, which is often needed for bSSFP acquisition to avoid banding artifacts and out of plane flow artifacts, is not required. While spiral techniques may be sensitive to off-resonance artifacts, for cine applications at 3T we have found that a readout duration of 5 ms or less produces acceptable results without off-resonance correction. The SPARCS technique is compatible with off-resonance deblurring techniques [124], and spectral-spatial excitation [125] could be used to further eliminate the signal from fat. With 8 seconds of data acquisition per slice, the whole ventricle can be covered in about 90 seconds. At 1.5T, considering the reduced SNR, bSSFP would be a better choice compared to GRE readouts. In this case, we also provide the spiral trajectory design to make it suitable for bSSFP readouts at 1.5T.

The idea of self-navigation was first pioneered by Larson et al. [59] for cardiac cine imaging using radial *k*-space sampling and a breath-hold SSFP sequence, where the self-gated signal was extracted from the echo-peak magnitude, kymogram and 2D correlation. This idea was further explored by using the center *k*-space point [58], center *k*-space line [64] or processed center *k*-space data [61]. These cardiac "self-gated" methods typically use breath holds to avoid the complexity of separating cardiac motion and respiratory motion. Some studies also focused on free breathing imaging using navigator signals [48,49,126]. A respiratory and cardiac self-gated method using a multi-echo 3D hybrid radial SSFP acquisition strategy was proposed by Liu et al. [51], where coils were selected based on the smallest variance of either the R-R intervals or respiratory positions for each individual coil. In our technique, PCA is used to separate combinations of coils which correspond predominantly to the respiratory and cardiac signals. The optimal PCA basis functions for the cardiac and respiratory self-gating signal were determined by choosing the basis functions which

had the highest amplitude in the cardiac or respiratory frequency ranges after band-pass filtering. Another study by Pang et al. [49] retrospectively binned the data into different cardiac and respiratory phases based on information extracted from self-gated projections, and the different respiratory states were reconstructed to perform motion correction. This approach could have potential issues with subjects that have irregular breathing patterns resulting in some respiratory bins with not enough data to reconstruct a reasonable quality image to do motion correction between bins. Thus, the performance of binning the data into different respiratory bins might vary in individuals with different breathing patterns. In the proposed SPARCS method, respiratory motion was corrected for each R-R interval, which should provide robustness to irregular breathing patterns. SPARCS provides cine images with similar spatial and temporal resolution to current clinical breath-hold techniques with a short free-breathing self-gated acquisition. In the future this technique could be compared to other free-breathing and/or self-gated techniques.

While previous real-time techniques required a sacrifice of spatial and/or temporal resolution, newer real-time techniques, such as real-time compressed sensing (CS) cine imaging, are becoming clinically available and are demonstrating real-time imaging with high spatial and temporal resolution. The current clinically available real-time compressed-sensing technique still requires an ECG to define the R-R interval [127], and the manufacturer recommends that this real-time technique is performed during a breath-hold. The L+S model we used in SPARCS is similar to the real-time CS reconstruction. Unfortunately, we could not compare SPARCS directly to this real-time CS technique, as it was not available on our scanner. A future comparison between SPARCS and such techniques may be of interest.

There are also several limitations for the current SPARCS strategy. Firstly, the spiral based acquisitions may be more sensitive to off-resonance artifacts than Cartesian GRE. Nonetheless,

with short spiral readouts, there is relatively little spiral-induced blurring or dropout artifacts. Additionally, off-resonance correction can be applied to further improve off-resonance performance. Compared with the ECG signal trigger, which always corresponds to the beginning of systole, the SPARCS extracted cardiac trigger can vary within the cardiac cycle. Moreover, this technique involves binning of data and could be sensitive to arrhythmias. To overcome this issue, data from R-R intervals that differ significantly from the mean R-R interval can be rejected, and data acquisition time could be extended if needed. Our filter cut-off frequency was set to support a maximum heart rate of 120 bpm. For all subjects scanned, the maximum heart rate was < 120 bpm, which justified a filter cutoff frequency of 2 Hz as reasonable when extracting the cardiac trigger. However, in pediatric patients or other patients with high heart rates, increasing the cutoff frequency to 3 Hz would support maximum heart rates of 180 bpm.

To summarize, the SPARCS technique can obtain 2D cine images with clinically acceptable spatial and temporal resolution, and adequate image quality, in a short free-breathing self-gated acquisition. In the future, this idea can be extended to a 3D or simultaneous multi-slice (SMS) acquisition. Although it might result in reduced contrast between the blood-pool and myocardium, an approach similar to that used for GRE-based coronary angiography at 3T, where images were acquired after administration of contrast, could also be utilized.

3.5 Conclusion

A free-breathing, continuous-acquisition, respiratory and cardiac self-gated, golden-angle spiral-cine imaging strategy, SPARCS, was presented. It enables cardiac cine imaging without ECG leads and with free breathing, which provides a simpler and more efficient protocol for clinical CMR imaging.

Chapter 4: Free breathing single acquisition of cine images and T1 maps

4.1 Introduction

Cardiac magnetic resonance (CMR) imaging is a widely used technique to provide important diagnostic and prognostic information in cardiac diseases. The advantage of CMR is that it can quantify cardiac function and perform tissue characterization. Cine imaging has become the gold standard for measuring left ventricular ejection fraction (LVEF). Parametric mapping of myocardial native T_1 and extracellular volume fraction (ECV), have shown the potential to assess a variety of myocardial pathologies [9,128] and guide therapy [129].

In current clinical practice, T_1 maps are usually acquired before and after contrast using a Modified Look-Locker Inversion recovery (MOLLI) technique [12] with breath-holding and ECG-gating. However, other approaches for accelerated T_1 mapping have been proposed. Those techniques utilize Bloch-equation simulations both to increase acquisition efficiency and improve T_1 accuracy. Model-based approaches [130–132] estimated T_1 maps directly from an under-sampled *k*-space based on a Bloch simulation model. The drawback of this approach is that the problem can be highly nonconvex and differences between the model and acquisition can lead to errors in the final maps [133]. The MR fingerprinting technique [75,76] utilizes a complex incoherent acquisition strategy and matches the corresponding dictionary curves generated by Bloch simulation to extract T_1 values. This technique depends on sufficient variation between the signal evolutions of tissues with different T_1 values, and is subject to the fidelity of the model accurately modeling the real acquisition. Dictionary learning (DL) is another method that has recently been used for accelerated parametric mapping, where a dictionary was formed using Bloch simulation and used as a

regularization term in the reconstruction problem [72,74]. The use of dictionary learning improved image quality in T_1 maps compared to the conventional SENSE method [74].

In a separate set of acquisitions, a stack of 10-12 2D short-axis cine images are typically acquired with breath holding and ECG-gating. This approach to CMR image acquisition is inefficient and subject to artifacts related to poor breath-holds, and requires the patient to perform a large number of breath-hold maneuvers during a 30-minute or more acquisition. To make the acquisition more simplified and efficient, the goal is to develop a strategy to obtain cine images and T_1 map in a single free-breathing acquisition.

4.2 Methods

4.2.1 Image acquisition

As shown in Figure 4.1, following an inversion recovery (IR) RF pulse, spirals are acquired continuously over 5 seconds using a spoiled-GRE spiral trajectory.

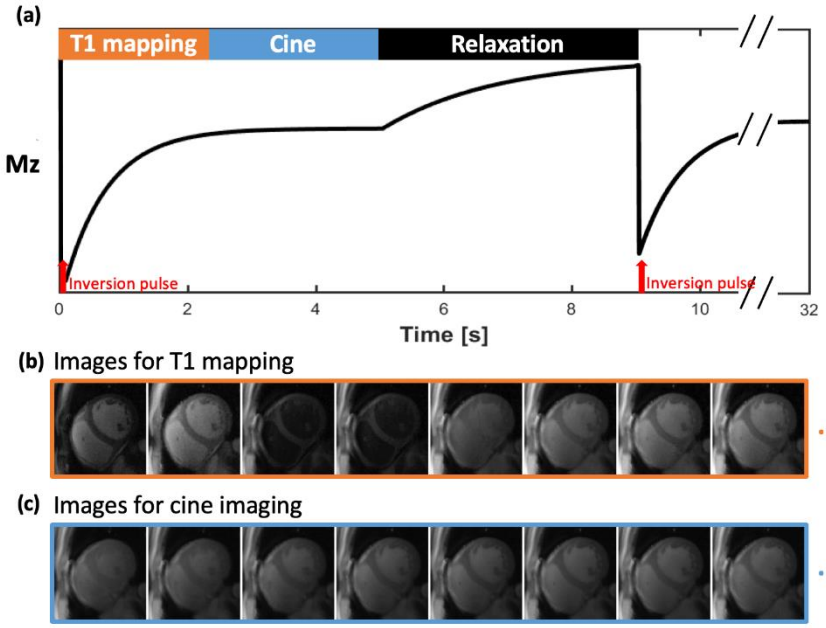

Figure 4.1 Schematic of the Acquisition. (a) acquisition strategy; (b) example of T1 map series; (c) example of cine image series.

A 4-seconds recovery period was allowed before the application of the next IR pulse, so that the effects of flip angle and T_1 can be differentiated when estimating the T_1 values in a 3-parameter model. This scheme was repeated 4 times over a 32 seconds acquisition per slice. T_1

maps were generated using the whole recovery curve, while cine images were reconstructed from the part where the signal is approaching steady state (Figure 4.1).

4.2.2 Image reconstruction

The processing pipeline is shown in Figure 4.2. An automatic algorithm [32,134] was used to detect the heart and select coils that had high SNR and minimal remote coil artifacts. PCA was performed on the images from each heartbeat to generate synthetic images for image registration. For T_1 mapping, every 5 spirals were combined to create a set of 4 images during a 167 ms diastolic acquisition window for each R-R interval. A dictionary was generated by k-SVD [135] using Bloch simulation with the acquisition parameters and ranging T_1 from 100 to 3000 ms, flip angle from 5 to 8 degree, IR efficiency from 0.9 to 1. Dictionary learning [73,74] reconstruction was performed in an alternating procedure to generate aliasing-free images (Figure 4.2(g)). Firstly, Orthogonal Matching Pursuit (OMP) algorithm was used to solve a_p:

$$\min_{a_p} \left\| R_n[x] - D a_p \right\|_2^2, \qquad s.t. \left\| a_p \right\|_0 \leq K \tag{4.1}$$

where R_n is the operator to choose the nth pixel through time, D is the dictionary, a_p is the sparse representation of the pth curve with respect to D, and K is the sparsity level. Then Sparse Linear Equations and Sparse Least Squares (LSQR) was used to solve x:

$$\min_{x,a_p} \|y - FSx\|_2^2 + \lambda \sum_n \left\| R_n[x] - D a_p \right\|_2^2, \qquad s.t. \left\| a_p \right\|_0 \leq K \tag{4.2}$$

where x is the vectorized T_1-weighted image to be reconstructed, y is the acquired under-sampled *k*-space data, F is the Fourier transform, and S is the sensitivity map. The parameters for dictionary learning reconstruction were initially chosen based on previous studies [72,74], and then tuned empirically for 3 data sets. The threshold for stopping criterion was $\varepsilon = 0.00001$, the number of dictionary atoms was 1000, the sparsity level (K) was 3, the regularization parameter (λ) was 4,

and the maximum iteration number was 15. Then, the dictionary learning reconstructed images were fitted by a 3-parameter model to generate T_1 maps (Figure 4.2(h)). For cine, after retrospective binning images were reconstructed using L1-SPIRiT [136] with temporal total variance (Figure 4.2(d)).

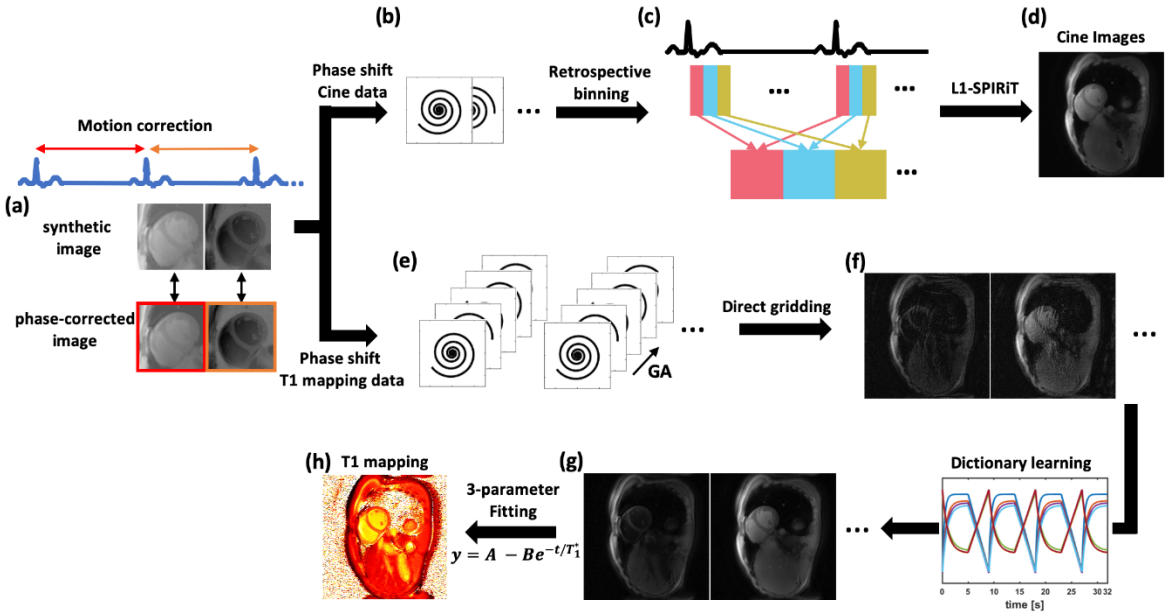

Figure 4.2 Processing pipeline. (a) Breathing motion was corrected by rigidly registering the phase corrected image with its corresponding synthetic image, as they share similar image contrast. (b) cine data after k-space phase shift were retrospectively binned across cardiac cycles (c); (d) cine images were reconstructed using L1-SPIRiT; (e) after k-space phase shift, every 5 spirals of T1 mapping data were combined to create direct gridding images (f); (g) dictionary learning results; (h) 3-parameter fitting to get T1 map.

4.2.3 In-vivo study

Six human subjects were imaged on a 3T Prisma or 3T Skyra Siemens scanners. During the scan gadolinium (Gd)–based contrast agents (Gadoteric acid – Gadoterate meglumine, Dotarem Guerbet or Clariscan GE Healthcare) were used. All subjects gave written informed consent, and imaging studies were performed under institutional review board (IRB) approved protocols. Pulse sequence parameters included: FOV = 340 mm, TR = 8.35 ms, TE = 1.45 ms, voxel size = 1.5×1.5 mm^2, slice thickness = 8 mm, flip angle = 7°, RF pulse time-bandwidth product = 5.4. A dual density (DD) spiral readout trajectory was rotated by the golden angle between subsequent TRs for data acquisition. The DD spiral had a fermi-function transition region

with a k-space density of 0.2 times Nyquist for the first 20% of the trajectory and an ending density of 0.026 times Nyquist [117]. Data were acquired for 32 seconds per slice. In the same scan, the clinical "gold-standard" breath-hold ECG-gated bSSFP MOLLI [12] T_1 images were also acquired with the following imaging parameters: FOV = 340 mm, resolution = 1.5 × 1.5 × 8 mm^3, TR/TE = 2.61/1.08 ms, flip angle = 35°, GRAPPA with R=2, 6/8 partial Fourier. Images were acquired during an end-diastolic window of 167 ms.

4.3 Results

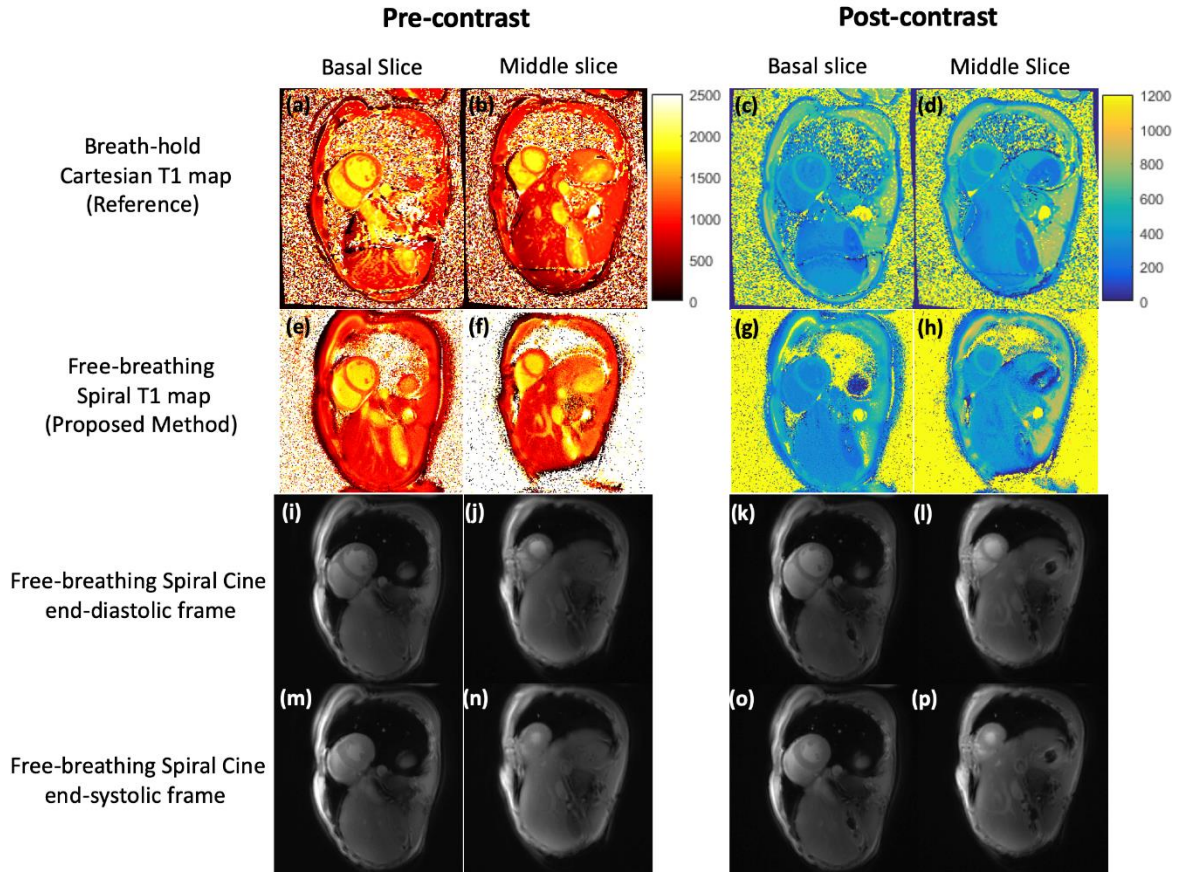

Figure 4.3 Cine and T1 mapping results. Basal (a,c) and middle (b,d) slice T1 maps are compared to the corresponding standard MOLLI results (a-d) both pre-contrast and post-contrast. End-diastolic and end-systolic cine frames acquired pre-contrast and post-contrast are shown in (i,j,m,n) and (k,l,o,p).

Figure 4.3 shows an example of T_1 mapping results (proposed method: Figure 4.3(e-h)) compared to the standard breath-hold Cartesian MOLLI T_1 maps (reference: Figure 4.3(a-d)) at basal and middle slice both pre- and post-contrast. T_1 values in myocardial and blood pool ROI

across subjects demonstrated good agreement with the reference (Table 4.1). The simultaneously acquired end-diastolic and end-systolic cine images show high image quality (Figure 4.3(i-p)).

Sequence type	Myocardium pre-contrast T1 value [ms]	Blood pool pre-contrast T1 value [ms]	Myocardium post-contrast T1 value [ms]	Blood pool post-contrast T1 value [ms]
BH Cartesian (reference)	1175.85 ± 76.77	1793.92 ± 66.46	538.60 ± 6.62	365.27 ± 13.07
DL Spiral (proposed method)	1199.33 ± 48.35	1794.73 ± 102.50	537.50 ± 10.21	380.03 ± 37.66

Table 4.1 T_1 value comparison.

4.4 Discussion

The proposed strategy demonstrates the acquisition of cine images and T_1 map in a single free breathing acquisition. T_1 values from the proposed method are comparable to the standard MOLLI sequence and the cine images show good image quality. However, the waiting time before each IR pulses is wasted and ECG signal is still needed to identify the cardiac phase. This can be optimized by changing the acquisition strategy and taking advantage of self-gating signals. In addition, as the flip angle equals 7°, the contrast in cine images may not be optimized.

4.5 Conclusion

We proposed a strategy to acquire cine images and T_1 map in a single free breathing acquisition. T_1 values from the proposed method are comparable to the standard MOLLI sequence and the cine images show good image quality.

Chapter 5: Dual excitation flip angle acquisition of cine images, T1 maps and LGE images

5.1 Introduction

During an imaging session, a stack of short-axis cine images is typically acquired while the patients are holding their breath and using ECG-gating to synchronize the acquisition to the cardiac cycle. LGE images are acquired in a similar fashion approximately 10 minutes after gadolinium injection. Typically, a number of short-axis T_1 maps will be acquired before and after contrast to quantify ECV. This approach of acquiring cine images, T_1 maps, and LGE images separately is inefficient, and subject to artifacts related to poor ECG-gating and/or breath-holds, leading to a 30-minute or more acquisition.

Recently, a few studies [76,137–139] have proposed acquiring cine images and T_1 maps simultaneously to simplify the acquisition and improve acquisition efficiency. However, most of these techniques either rely on breath-holding to constrain the respiratory motion or use ECG-gating to synchronize cardiac motion. The recently developed CMR multi-tasking technique [78] has shown great potential to obtain cine images and T_1 maps at the same time in a continuous radial acquisition scheme, where every other radial *k*-space data is used as auxiliary data to resolve both cardiac and respiratory motion. One limitation is that when a Look-Locker type acquisition is performed continuously, the recovery time constant T_1^* is a function of both flip angle and T_1. It is thus impossible to distinguish between the effects of flip angle and T_1 relaxation as has been discussed previously by Crawley and Henkelman [79]. Therefore, a B_1^+ map is needed to accurately determine T_1 from the effective T_1^* in such acquisitions. Since a B_1^+ map is often acquired using a separate specialized pulse sequence, there is a potential for mis-registration between the B_1^+ map

and the other acquired data, particularly for a cardiac and respiratory self-gated acquisition. An additional consideration for accurate 2D T_1 mapping is the slice profile effect. Previous studies [137,140,141] have demonstrated that taking slice profile effect into consideration will improve the accuracy of T_1 quantification.

To address the current technical challenges and extend the work in Chapter 4, we proposed a dual excitation flip angle continuous acquisition strategy to simultaneously acquire cine images and T_1 maps during free-breathing and without ECG-gating. Cardiac motion is extracted by applying PCA to a sliding window reconstruction of low-resolution heart images, and respiratory motion is corrected using data from each heartbeat. By measuring T_1^* from the Look-Locker data for each of the two flip angles, the dual flip angle approach can separate the flip angle and T_1-relaxation effects. Utilizing an iterative projection onto convex sets (POCS) approach, slice profile correction can also be performed. Thus, both cine images and T_1 maps can be acquired during the continuous spiral acquisition. Spiral acquisitions repeatedly collect the low spatial-frequency portion of *k*-space, facilitating self-gating. These acquisitions are more time efficient than Cartesian or radial acquisitions as they cover a greater extent of *k*-space during each repetition. The proposed technique is tested in a T1MES phantom [142] with 14 human subjects, and compared to conventional BH ECG-gated bSSFP cine imaging and MOLLI T_1 mapping techniques.

5.2 Theory

5.2.1 Dual flip angle acquisition

The proposed strategy is comprised of a continuous acquisition with an IR RF pulse applied every four seconds, using one excitation flip angle (FA_1) following the first four inversion pulses and another excitation flip angle (FA_2) following the subsequent four inversion pulses. As there is no gap before applying the next inversion pulse, signals $M(t)$ following the 2nd - 4th IR pulses and

6th - 8th IR pulses follow a T_1^* recovery from $-M_{z+}$ to M_{z+}, which can be fitted to a 3-parameter model [143]:

$$M(t) = M_{z+} - (M_{z+} + E_{IR}M_{z+})e^{-t/T_1^*}, \quad (5.1)$$

where M_{z+} is the signal immediately before the next inversion pulse, E_{IR} is the IR efficiency and T_1^* is the apparent T_1. Then, based on the relationship between T_1^* and T_1 [143], the T_1 map can be recovered by simultaneously solving two equations:

$$\frac{1}{(T_1^*)_1} = \frac{1}{T_1} - \frac{\ln\cos\beta FA_1}{TR}, \quad (5.2)$$

$$\frac{1}{(T_1^*)_2} = \frac{1}{T_1} - \frac{\ln\cos\beta FA_2}{TR}, \quad (5.3)$$

where β is the scale factor between the nominal flip angle and the actual flip angle, and the two apparent T_1 maps $(T_1^*)_1$ and $(T_1^*)_2$ are obtained for two flip angles by fitting Equation 5.1. Along with the T_1 map, this fitting scheme provides a flip angle scale (β) map.

5.2.2 Slice profile correction

While the above approach would be sufficient for an ideal slice profile, the actual slice profile must be considered to accurately recover T_1 from the fitted T_1^* maps. As the signal evolution is a function of the T_1, the B_1^+ scale factor (β), and the flip angle profile of the slice, the signal evolution will vary across the slice and the T_1^* that is measured experimentally will be based on the signal evolution after integration of these effects across the slice profile at each TR. By performing Bloch equations across a range of T_1 and β values, and simulating the signal evolution across the actual slice flip angle profile FA(z), a look up table for T_1^* as a function of T_1 and β can be created for each of the two flip angles.

$$(T_1^*)_1 = f(T_1, \beta, FA_1(z)), \quad (5.4)$$

$$(T_1^*)_2 = f(T_1, \beta, FA_2(z)), \quad (5.5)$$

At a small excitation flip angle, the B_1^+-related flip angle effects will minimally disrupt the apparent T_1 recovery, and thus T_1^* will closely approximate the T_1 recovery curve. On the contrary, when a large excitation flip angle is used, the T_1^* recovery curve will be more strongly weighted by the B_1^+-related flip angle effects. Based on this observation, instead of directly solving Equation 5.2 and Equation 5.3 as a system of equations, to take into consideration the slice profile effects, the final T_1 and β values can be determined iteratively from the measured T_1^* maps for each flip angle and the look-up tables using a POCS-based approach as described in the methods section.

5.3 Methods

5.3.1 Image acquisition

As shown in Figure 5.1, following an inversion-recovery RF pulse, spiral trajectories are acquired continuously over 4 seconds using a spoiled gradient-echo (SP-GRE) pulse sequence, with each spiral interleaf rotated by the golden-angle (137.51°) relative to the immediately preceding interleaf. This pattern is repeated 4 times with flip angle 1 (3°) and subsequently repeated another 4 times with flip angle 2 (15°).

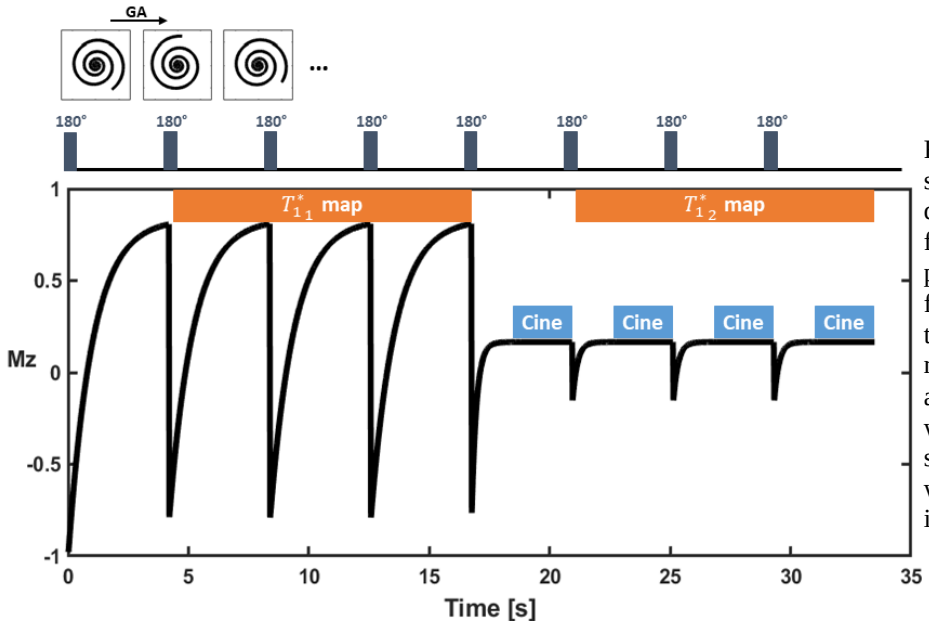

Figure 5.1 Acquisition strategy. Signal evolution during acquisition. After the first 4 inversion recovery pulses, flip angle 1 was used for generating $(T_1^*)_1$ map. For the second 4 inversion recovery pulses, where flip angle 2 was used, $(T_1^*)_2$ map was generated. Data in the steady state using flip angle 2 was used to generate cine images.

5.3.2 Simulation

To determine the choice of the dual excitation flip angles, a Monte Carlo simulation was implemented by varying the flip angles from 1° to 30°, β from 0.4 to 1.2, and T_1 from 200 ms to 2500 ms. To mimic the SNR of the actual scan protocol, white Gaussian noise was added to the simulated signal curves. Root mean square error (RMSE) of the T_1 value was calculated across flip angle combinations. Flip angles yielding the lowest RMSE across the T_1 range were chosen. The T_1 and β were calculated according to Equation 5.2 and Equation 5.3.

5.3.3 Cardiac self-gating

As shown in Figure 5.2(a), a low-resolution (5×5 mm^2) sliding window image was reconstructed for each frame by combining the central portion of 10 neighboring spiral interleaves and reconstructing with Non-Uniform Fast Fourier Transform (NUFFT). Considering different signal intensities and SNR between FA_1 and FA_2, self-gating cardiac signals for the two excitation flip angles were extracted separately. An automatic heart detection algorithm [134] was implemented to detect an 80×80 pixel ROI containing the heart using images collected with FA_2, since it's easier to capture intensity changes in the heart region under higher readout flip angle. Two series of heart images with FA_1 and FA_2 through time can then be obtained using the heart ROI (Figure 5.2(b)). For each flip angle, after stacking the pixels in each heart image as a vector, a low-pass temporal filtering was used to eliminate the high frequency component caused by noise and residual aliasing. Next, PCA was performed on this data through time (Figure 5.2(c)), similar to the approach described in [134]. To extract and determine the cardiac self-gating signal, a band-pass filter spanning the cardiac motion frequency range (0.5 Hz to 2 Hz) was applied to the first 10 temporal basis functions. Then, frequency spectrum analysis was used to automatically find the cardiac motion-related component by determining which basis function had the highest amplitude in the cardiac

motion frequency range. After bandpass filtering the chosen component, peak detection with a signal threshold determined from the mean of all the peaks and troughs was implemented. Since data near the null point in the T_1 recovery might disturb peak detection, linear interpolation was used to correct the point right after the inversion pulses (Figure 5.2(d)).

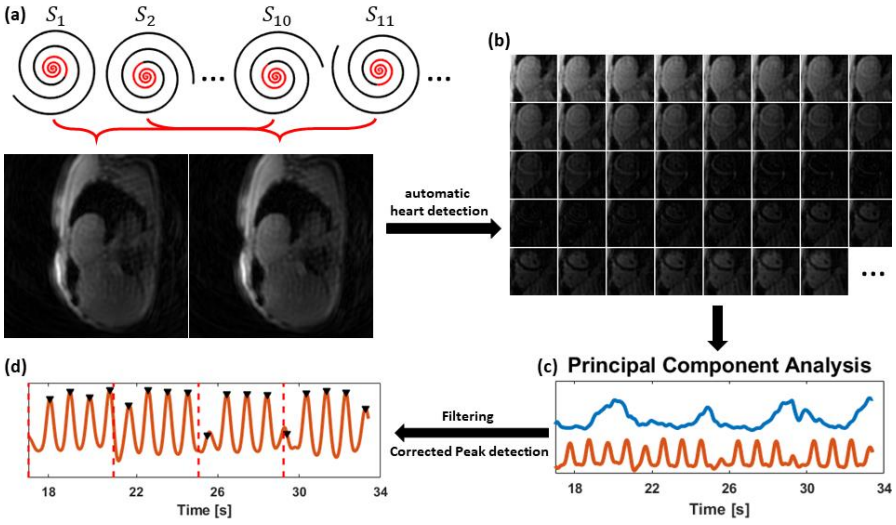

Figure 5.2 Pipeline of cardiac self-gating. (a) The central data (red) from every 10 consecutive spiral interleaves were used to generate a series of sliding window low-resolution images. (b) Using the automatic heart detection algorithm, a series of sliding window images which only retain the heart region were obtained. (c) PCA was performed across this image navigator through time to derive temporal-basis functions. (d) Extracted filtered cardiac motion component and corrected peak detection was performed to detect the cardiac triggers.

Since the cardiac self-gating signal was extracted from the image as compared to the physiological ECG signal, the triggers derived typically correspond to peak-systole rather than to the R-wave of the ECG. To validate the accuracy of the self-gating signal, we compared the recorded ECG R-R interval length versus the cardiac cycle length as determined by the time interval between subsequent self-gating triggers.

5.3.4 Respiratory motion correction

To correct respiratory motion, it was assumed that the respiratory position did not vary significantly within each heartbeat [134]. Based on this assumption, the *k*-space data over each R-R interval was combined to create a static image for each heartbeat. The previously detected heart ROI was used to select only the heart region for each heartbeat image. To increase the robustness of motion detection to signal intensity changes during T_1 recovery, a synthetic image series was generated by applying PCA on the original images. Only the first and second component of the

PCA, corresponding to the average intensity and the signal intensity change caused by inversion pulses, respectively are used. The original image series can therefore be rigidly registered to the synthetic image series, without the influence of signal intensity change, to estimate the bulk motion caused by breathing (Figure 5.3(c)). These linear phase shifts derived from each R-R interval combined images were applied to the acquired raw *k*-space data for each frame within that R-R interval as previously described [32].

5.3.5 Image reconstruction

Before reconstructing images, an automatic coil selection algorithm [134] was used to discard the low SNR and remote coils which primarily contribute aliasing energy over the heart.

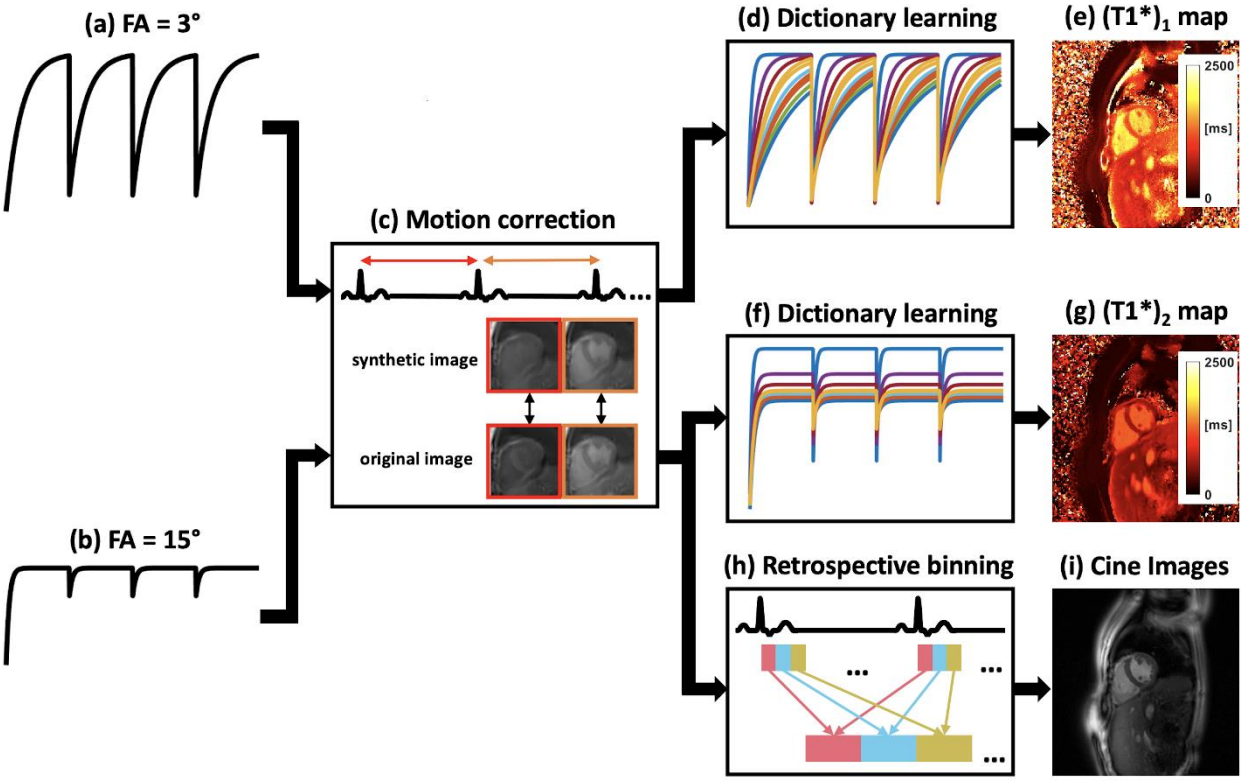

Figure 5.3 Pipeline of data processing. Data with FA_1 = 3° (a) and FA_2 = 15° (b) were motion corrected by rigidly registering the original images with its corresponding synthetic images, as they share similar image contrast (c). After respiratory motion correction, using the dictionary for FA_1 (d), dictionary learning reconstruction was performed to create $(T_1^*)_1$ map (e). Similarly, the dictionary for FA_2 (f) was used to generate $(T_1^*)_2$ map. Data from the constant-signal portion for FA_2 were retrospectively binned (h) to create cine images (i).

5.3.5.1 Cine images

Cine images were reconstructed using the steady state portion of the signal collected using FA_2 due to the higher SNR and improved blood-pool to tissue contrast, similar to our SPARCS approach [134]. After correcting the respiratory motion, data were retrospectively binned using the extracted self-gating signal with a temporal resolution of around 40 ms. The number of reconstructed phases were determined by dividing the R-R interval into 40 ms temporal bins. Images were reconstructed using the L+S method [71], as shown in Equation 1.5. We have used L+S model to reconstruct cardiac self-gated cine images in Chapter 3.

5.3.5.2 T1 maps

For T_1 mapping, every 5 spirals were combined to create a set of 4 images during a 167 ms diastolic acquisition window for each R-R interval. Two dictionaries, one for each of the two flip angles, were generated by k-SVD [135] using Bloch simulation time courses with the acquisition parameters including slice profile effects, where two hundred isochromats were simulated across the actual slice profiles that were used in the study (time-bandwidth (TBW) = 5.4). T_1 values varied from 200 to 2500 ms. β values were ranging from 0.4 to 1.2. IR efficiency values varied from 0.9 to 1. Dictionary learning [73,74] reconstruction was performed similarly as in Equation 4.1 and Equation 4.2. The parameters for dictionary learning reconstruction were initially chosen based on previous studies [72,74], and then tuned empirically for 3 data sets. The threshold for stopping criterion was $\varepsilon = 0.00001$, the number of dictionary atoms was 1000, the sparsity level (K) was 3, the regularization parameter (λ) was 4, and the maximum iteration number was 15.

Two apparent T_1 maps ($(T_1^*)_1$, $(T_1^*)_2$) were obtained by fitting the 3-parameter model of Eq. [1] using the Dictionary learning reconstructed images. As described in the Theory section 2.2, Bloch simulation of the signal evolution from CAT-SPARCS was performed using the actual excitation flip angle profiles. Two hundred isochromats were simulated across the slice profile for a range of T_1 values from 200 ms to 2500 ms and B_1^+ scales (β) from 0.4 to 1.2 to create look-up tables for each flip angle including slice profiles. Then, the correct T_1 and β values were determined iteratively from the measured T_1^* maps and the look-up tables using a POCS-based approach (Figure 5.4). In the first iteration, an estimated $(T_1)_0$ is obtained using look-up table I for 3° flip angle (green) (Equation 5.4), and the $(T_1^*)_1$ map with β held fixed at $\beta_0 = 1$. Then a new β_1 value can be obtained using the $(T_1^*)_2$ map and look-up table II for 15° flip angle (blue) (Equation 5.5) by holding $(T_1)_0$ fixed. For the next iteration, β_1 will be combined with $(T_1^*)_1$ map and look-up table I to generate a new $(T_1)_1$. And next the $(T_1)_1$ will be used with $(T_1^*)_2$ map and look-up table II to generate a new β_2. This iterative POCS-procedure can be repeated until both T_1 and β converge, typically in 3 iterations.

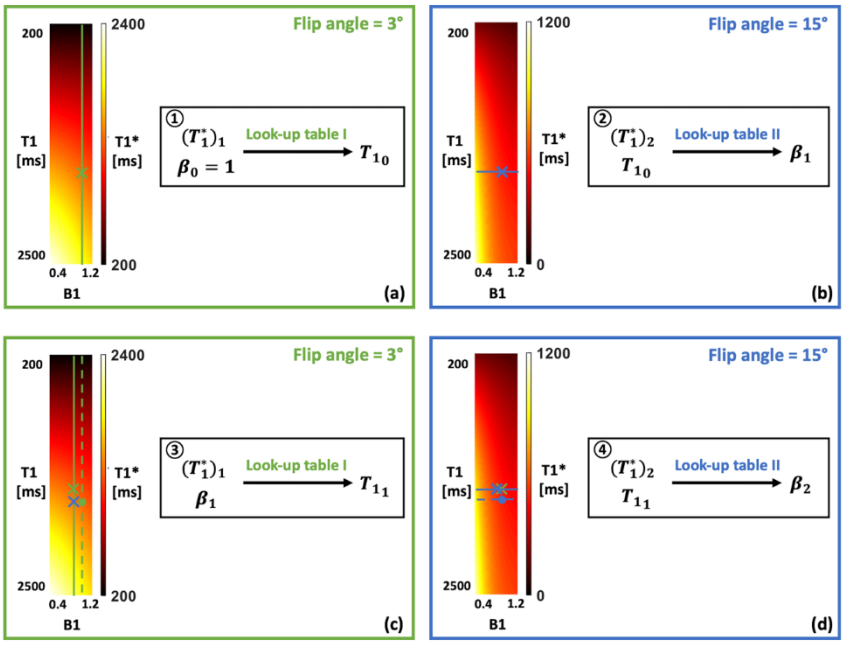

Figure 5.4 POCS-based iterative fitting using look-up tables. (a)(b) show the first iteration while (c)(d) show the second iteration. The solid lines and crosses show the determined β and T_1. The dashed lines and circles indicate the β and T_1 values at the previous iteration.

5.3.5.3 LGE images

After respiratory motion correction (Figure 5.5(a)), the 15° data can be used to generate LGE images. Firstly, to determine the inversion time (TI) a sliding window approach was used in the first few hundred milliseconds after the 6th inversion pulse (Figure 5.5(b)). Then, using the self-gated cardiac triggers the same cardiac phase data at the chosen TI after 6th, 7th, and 8th inversion pulses were combined to reconstruct an LGE image using SPIRiT [68].

Alternatively, using the generated post-contrast T_1 map (Figure 5.5(c)), we can also make a synthetic LGE image by using the equation [144]:

$$SI(TI) = 1 - 2 \times e^{-\frac{TI}{T_1}}, \tag{5.6}$$

where SI represents signal intensity.

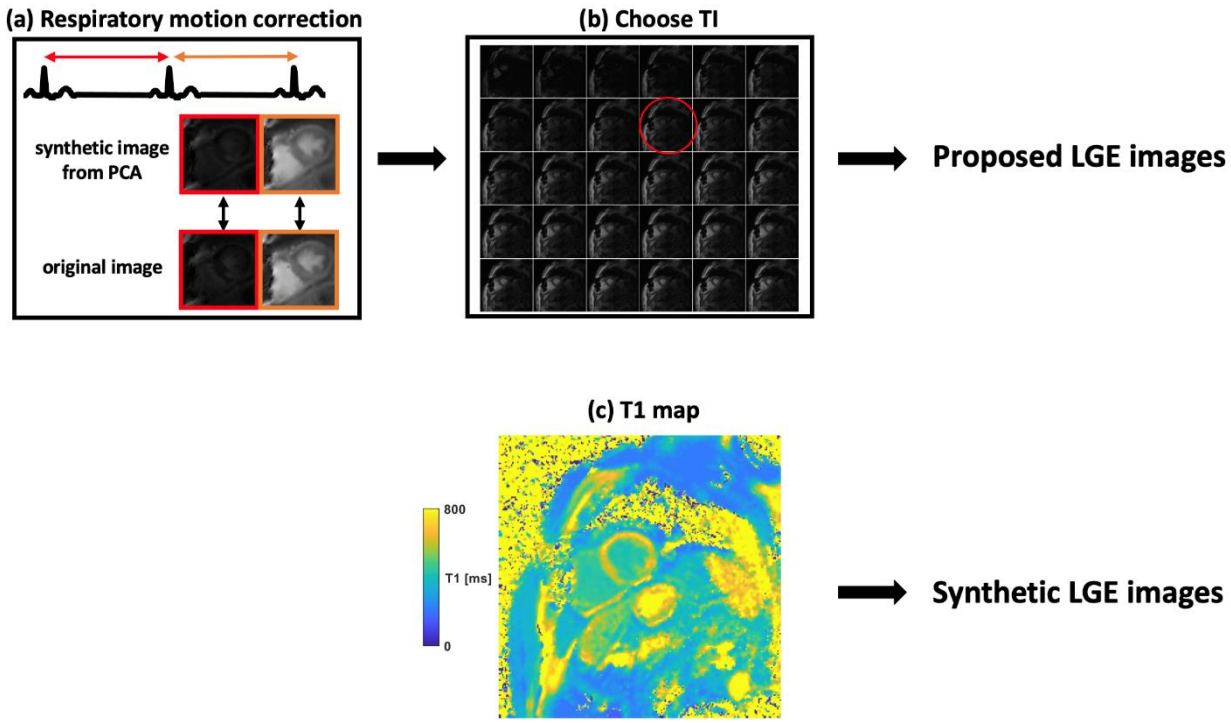

Figure 5.5 LGE generation (a) respiratory motion correction (b) choose TI based on sliding window results (c) post-contrast T_1 map.

5.3.6 Phantom study

In order to evaluate the accuracy of the proposed strategy, a T1MES phantom consisting of 9 tubes with T_1 values ranging from ~250 – 1700 ms [142] was imaged using the standard body phased-array RF coil. Scanning was performed on a 3T scanner (MAGNETOM Prisma, Siemens Healthineers, Erlangen, Germany). The proposed CAT-SPARCS acquisition strategy was implemented as stated above. The sequence parameters included: TR/TE = 8.35/1.45 ms, RF pulse time-bandwidth product = 5.4, FOV = 340 mm, spatial resolution = 1.5 ×1.5 × 8 mm^3. A dual-density spiral readout trajectory was used with a fermi-function transition region and a *k*-space density of 0.2 times Nyquist for the first 20% of the trajectory and an ending density of 0.026 times Nyquist [117]. To obtain reference T_1 values of the phantom for validation, a gold-standard 2D inversion-recovery spin-echo (IR-SE) sequence was performed with the following parameters: FOV = 190 × 190 mm^2, spatial resolution = 1.5 × 1.5 × 8 mm^3, TR/TE = 10000/10 ms, 15TIs = 50, 100, 150, 200, 250, 300, 400, 500, 750, 1000, 1200, 1500, 1700, 2000, and 3000 ms. The reference T_1 values were determined by a 3-parameter non-linear least square fitting algorithm. In addition, a clinically used 5(3)3 MOLLI sequence with bSSFP readouts [12] was performed with the following imaging parameters: FOV = 340 mm, resolution = 1.5 × 1.5 × 8 mm^3, TR/TE = 2.61/1.08 ms, flip angle = 35°, GRAPPA with R=2, 6/8 partial Fourier. Images were acquired during an end-diastolic window of 167 ms. The ECG signal was simulated on the scanner at a heart rate of 60 beats per minute during the experiments.

To compare with a reference B_1^+ map, a Cartesian spoiled-GRE based Bloch-Siegert shift B_1^+ mapping [145] sequence was performed. An off-resonant Fermi pulse was played between the slice rewinder and the phase-encoding gradient lobes: Fermi pulse duration = 8 ms, off-resonance shift = ±4 kHz, K_{BS} = 79.73 rad/G^2, $B_{1,peak}$ = 0.13 G. The following sequence parameters were

used: FOV = 290 × 290 mm^2, spatial resolution = 1.5 × 1.5 × 8 mm^3, TR/TE = 151.50/12.30 ms, flip angle = 15°.

5.3.7 In-vivo study

Continuous inversion-recovery dual excitation flip angle spiral imaging was performed in 14 subjects: 10 subjects acquired basal and middle short-axis slices, and 4 subjects performed whole-heart coverage short-axis slices. The subjects included 10 healthy volunteers and 4 patients undergoing clinical CMR studies. Among them, 12 subjects received gadolinium (Gd)–based contrast agents (Gadoteric acid – Gadoterate meglumine, Dotarem Guerbet or Clariscan GE Healthcare) during the scan. All subjects gave written informed consent, and imaging studies were performed under institutional review board (IRB) approved protocols. Experiments were performed on the 3T Prisma or Skyra scanners (MAGNETOM, Siemens Healthineers, Erlangen, Germany) utilizing same pulse sequence parameters including spiral gradient waveforms as Chapter 5.3.6. Both pre-contrast and post-contrast (5-10 minutes after the contrast injection) acquisitions were performed. Although, for the proposed method, ECG-gating is not needed, the ECG signal was recorded for validation of the self-gating. The standard MOLLI pulse sequence was performed for the same slice positions as the proposed method with parameters as described above. Standard bSSFP breath-hold ECG-gated Cartesian cine imaging and phase-sensitive IR LGE images [146] were also performed for a comparison.

5.3.8 Image analysis

Cine image quality for all datasets was assessed by an experienced cardiologist in a blinded fashion. Image quality was evaluated on a 5-point scale ranging from 1 (poor and not usable) to 5 (clinically excellent). A score of 3 is clinically acceptable, but with some artifacts. Comparison

between the scores from the proposed method and the standard cine images were computed using paired *t*-test tests.

To analyze the phantom T_1 results, circular ROIs were drawn for each tube. The mean and standard deviation of T_1 values were compared among the proposed method, IR-SE and MOLLI techniques. The in-vivo T_1 values were measured by drawing ROI on myocardium in basal short-axis slice. Bland-Altman plots of pre- and post-contrast myocardium T_1 values across all cases were made for the proposed method and MOLLI technique. To evaluate quantification of LVEF, slices covering the whole heart in short axis were collected in 5 subjects. LVEF was determined by manual tracing of the endocardial borders in systole and diastole by an experienced cardiologist. The calculated LVEF was compared to that from the standard clinical breath-hold ECG-gated bSSFP cine images using paired *t*-test.

Image reconstruction and processing were performed using MATLAB (The Mathworks Inc., Natick, MA). Statistical analysis was performed using SAS software 9.4 (SAS Institute Inc., Cary, NC).

5.4 Results

5.4.1 Simulation

Figure 5.6(a) and (b) show RMSE colormaps for different flip angle combinations at 4 typical T_1 values in the myocardium and blood pool, pre- and post-contrast, when β = 1. Figure 5.6(c) summarizes the Monte Carlo simulation results and shows the excitation flip angle combinations with lowest T_1 RMSE across a range of T_1 values from 200 to 2500 ms. Based these results, we chose FA_1 to be 3 degrees and FA_2 to be 15 degrees.

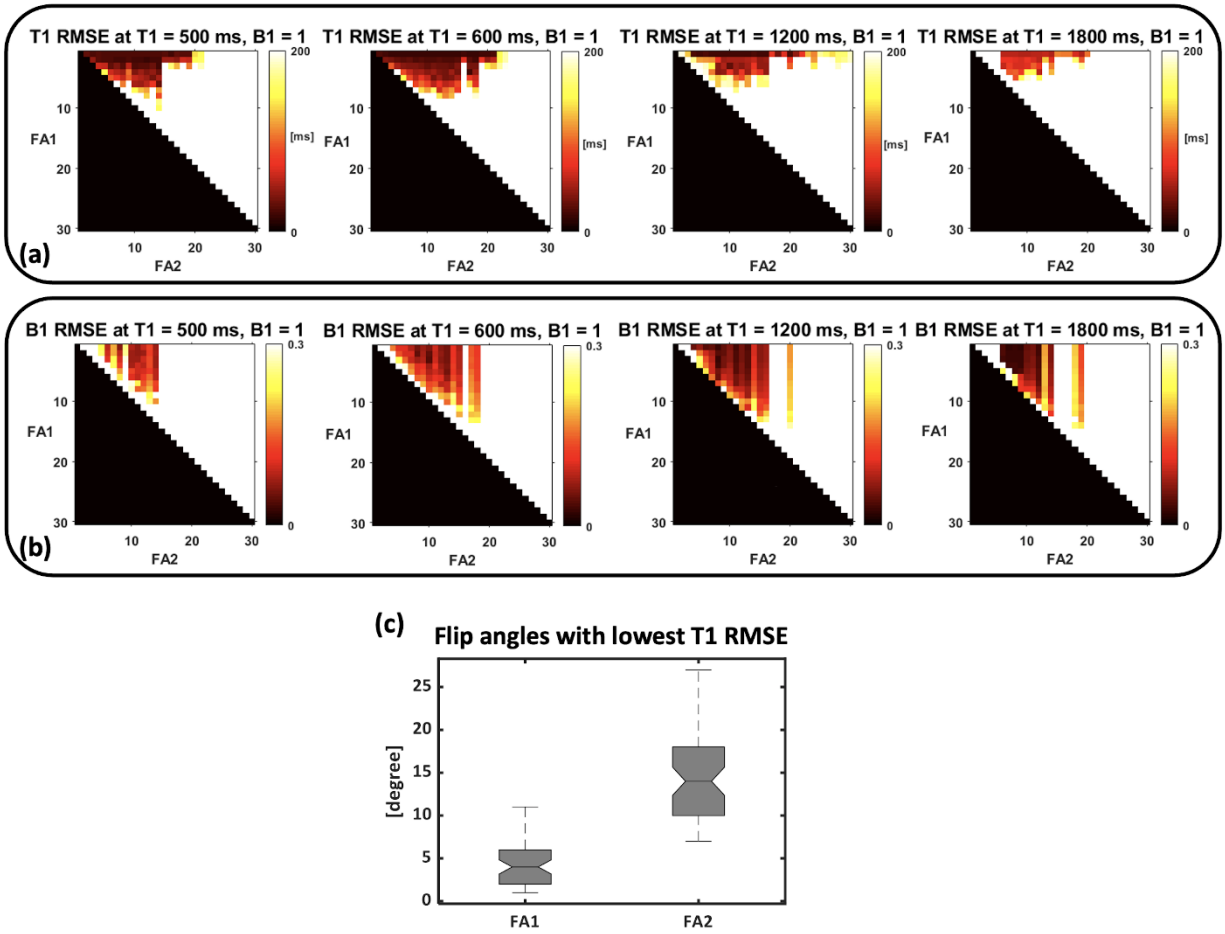

Figure 5.6 Monte Carlo Simulation. (a) and (b) Plots of T_1 RMSE (a) and B_1^+ RMSE (b) as a function of the two flip angles for 4 typical T_1 values in the myocardium and blood pool, pre- and post-contrast. (c) Values for FA_1 and FA_2 yielding the lowest T_1 RMSE for T_1 values ranging from 200 ms to 2500 ms.

5.4.2 Evaluation of phantom results

Figure 5.7 shows the T1MES phantom results. The $(T_1^*)_1$ map and $(T_1^*)_2$ map are the apparent T_1 maps corresponding to the two excitation flip angles. Following dual flip angle fitting, a T_1 map and β map can be created. The proposed β map (Figure 5.7(c)) was compared with the

Bloch-Siegert shift B_1^+ map (Figure 5.7(d)), and both demonstrated similar B_1^+ scale variation across the phantom. There were some differences in the B_1^+ scale for the long T_1 tubes; however, use of the derived β resulted in T_1 values that were closer to the IR-SE results, suggesting that the β map may correct for other system imperfections. The proposed T_1 map (Figure 5.7(e)) was compared with that from IR-SE (Figure 5.7(g)) and the clinically used MOLLI (Figure 5.7(f)) pulse sequence. The mean values from the ROIs for the 9 tubes are compared in Figure 5.7(h). The mean bias for the short T_1 tubes between IR-SE and the proposed method is 15.8 ms, compared to 27.2 ms between IR-SE and MOLLI, while the mean bias for the three long-T_1 tubes between IR-SE and the proposed method is 99.9 ms, compared to 120.4 ms between IR SE and MOLLI. Across all nine tubes the bias in T_1 values compared to gold standard IR-SE was smaller for the proposed technique as compared to MOLLI (p = 0.01). The NRMSE between proposed β map and BS B1 map in 9 tube ROIs is 0.10.

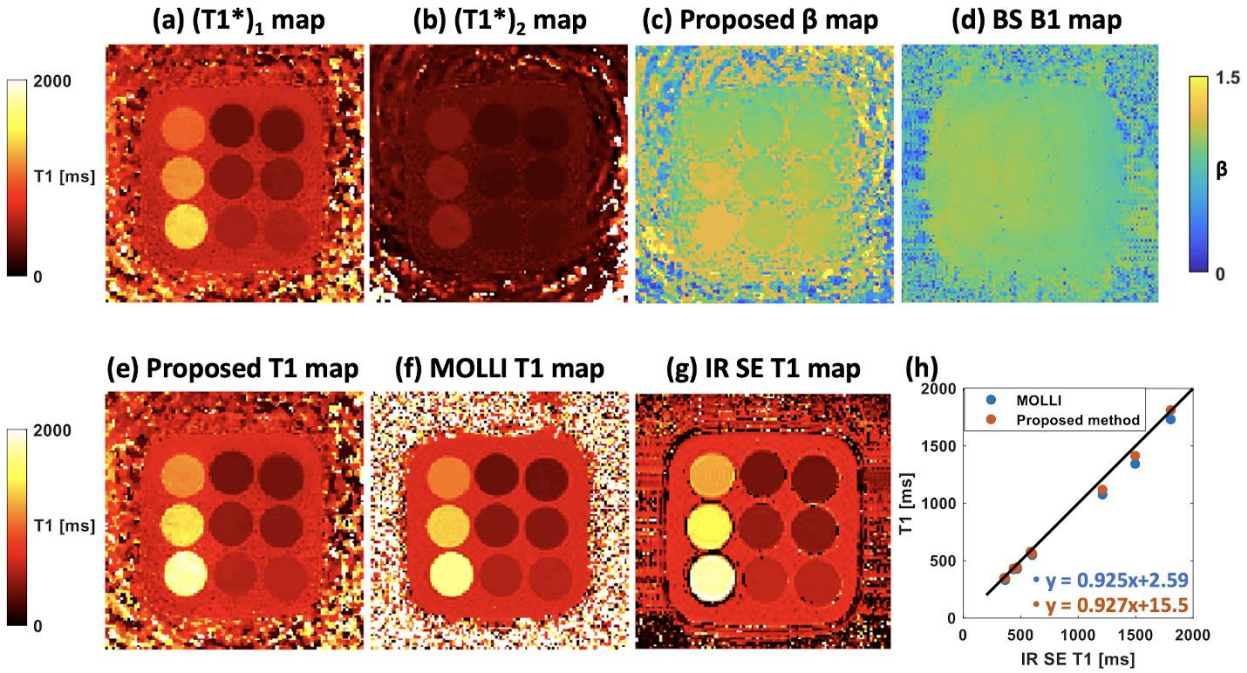

Figure 5.7 Phantom results. $(T_1^*)_1$ and $(T_1^*)_2$ maps corresponding to the 2 flip angles are shown in (a) and (b). With the proposed method, a β map (c) and T_1 map (e) can be obtained. (f) T_1 map for the MOLLI pulse sequence. (f) T_1 map for the IR-SE pulse sequence. (h) Comparison of T_1 values from the proposed method and MOLLI, compared to the "gold-standard" IR-SE results. The black line is the reference (diagonal) line. The mean T_1 values of 9 ROIs from proposed method show a strong positive correlation relationship with the IR-SE results ($R^2 = 0.998$).

5.4.3 Cardiac self-gating

A Bland-Altman plot comparing the R-R interval length from the recorded ECG trigger to that from the extracted cardiac self-gated trigger is shown in Figure 5.8(a). The mean difference of cardiac cycle lengths between the ECG and self-gating signals for the subjects was -0.26 ms, with a 95% confidence interval of 66.60 ms to -67.13 ms. The correlation plot in Figure 5.8(b) demonstrates a good correlation, $R^2 = 0.97$, between the R-R interval length from ECG and self-gated cardiac signals without a significant bias (p = 0.27, paired sample *t*-test). These results demonstrate that the self-gating cardiac trigger can be used as a reasonable surrogate for the ECG signal.

5.4.4 Respiratory motion correction

Figure 5.8(c) and (d) show an example of respiratory motion correction performance. The improvement in the temporal fidelity can easily be appreciated in the x-t profiles following rigid-respiratory motion correction.

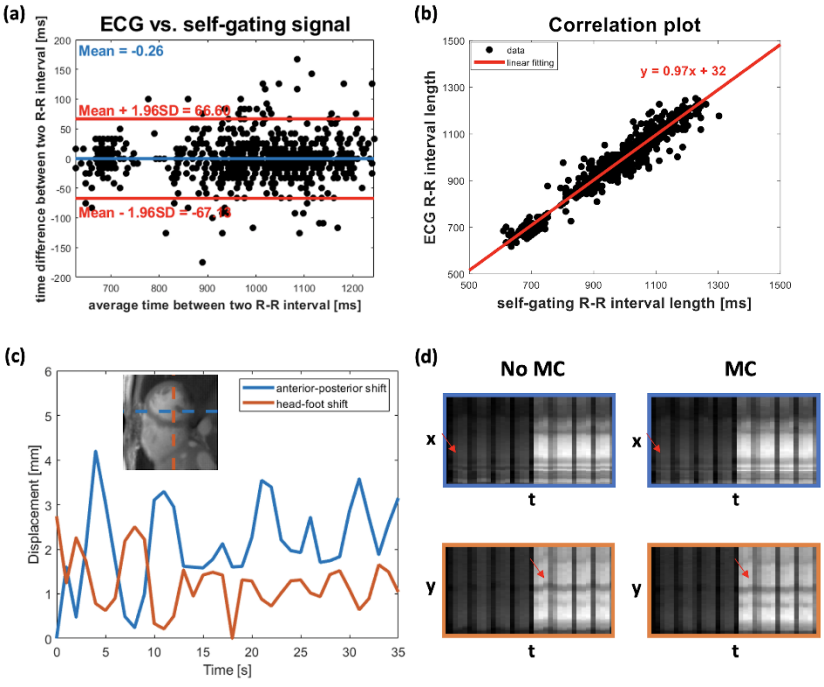

Figure 5.8 Self-gating and motion correction performance. (a) Bland-Altman plot indicates a non-significant bias of -0.26 ms for the R-R interval length difference between self-gated and ECG signals across all the subjects. (b) There is a strong positive correlation relationship ($R^2 = 0.97$) between self-gated and ECG R-R interval lengths. (c) A static image was reconstructed from each heartbeat to generate the images used for respiratory motion compensation. The rigid registration displacements in x (anterior-posterior: A-P) and y (head-foot: H-F) directions were determined and used to correct the respiratory position. (d) x-t and y-t profiles before and after registration in the H-F and A-P directions. The x and y positions are shown as dashed lines in (c). As indicated by the red arrows, the heart borders are more closely aligned following respiratory motion correction (MC).

5.4.5 Evaluation of cine images

Figure 5.9(a-l) shows reconstructed short-axis cine images from two subjects.

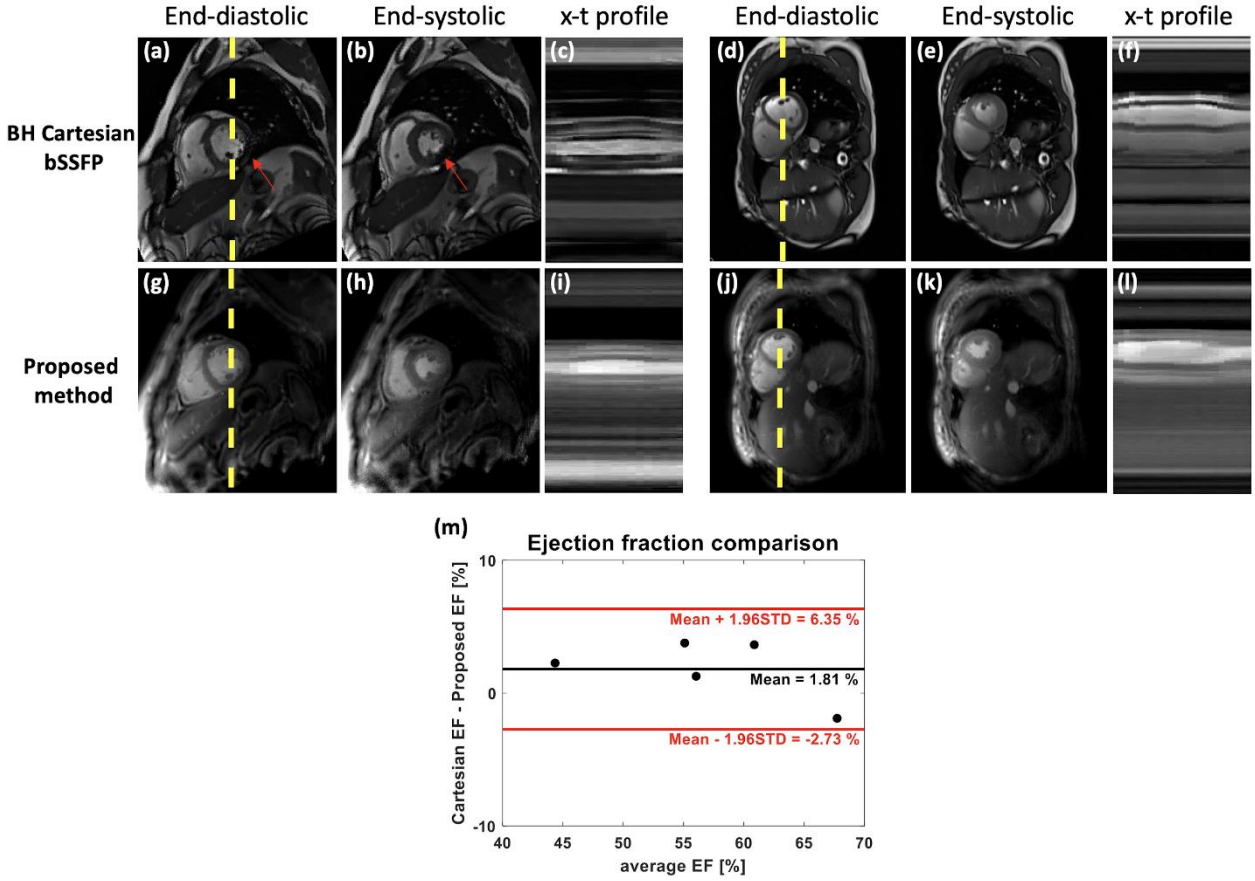

Figure 5.9 Cine image results. End-diastolic (a, d) and end-systolic (d, e) frames for two subjects from the standard breath-hold (BH) ECG-gated Cartesian bSSFP sequence compared with those (g, h, j, k) from the proposed CAT-SPARCS strategy. X-t profiles (c, f, i, l) for the reconstructed images along the profile, denoted by the dashed line in end-diastolic images. We can see the obvious banding artifacts using the standard method (red arrows). (m) is the Bland-Altman plot of LVEF for the subjects with whole-heart coverage (N = 5), comparing among the proposed CAT-SPARCS cine images and the standard results. STD = standard deviation.

Figure 5.9(a-f) correspond to the standard breath-hold ECG-gated Cartesian bSSFP results while Figure 5.9(g-l) demonstrate the proposed method. In subject 1 on the left, we can visualize the banding artifacts using the standard bSSFP method as indicated by the red arrows. Compared to the standard bSSFP method, as expected, the gradient-echo based CAT-SPARCS technique is less susceptible to off-resonance artifacts seen with bSSFP at 3T. A Bland-Altman plot comparing LVEF between the proposed cine images and the standard Cartesian bSSFP images is shown in Figure 5.9(m). The paired *t*-test shows no significant difference between the two methods (p =

0.16). Although there is a signal intensity difference in the x-t profiles caused by the contrast difference between GRE and bSSFP readouts, both the X-t profiles and Bland-Altman plot demonstrate the accuracy of calculating LVEF using the proposed CAT-SPARCS strategy. The mean (± standard deviation) image-quality scores of standard bSSFP images and CAT-SPARCS images were 4.65 (± 0.30) and 4.31 (± 0.50). There is no significant difference between the two methods by paired t-test (p = 0.095). A larger study is needed to further validate the significance of the image quality difference.

5.4.6 Evaluation of T1 maps

Figures 5.10 demonstrates an example case from in-vivo studies. Figure 5.10(a-d, i-l) show the short-axis basal and middle slices pre-contrast while (e-h, m-p) show the ones post-contrast. The first two columns are the apparent T_1 maps corresponding to the two excitation flip angles. The third column is the T_1 map from the proposed method, compared with the clinically used MOLLI T_1 map in the fourth column. Figure 5.10(q, s) are base and mid ECV maps from proposed technique, comparing to the ECV maps generated from MOLLI images (Figure 5.10(r, t)).

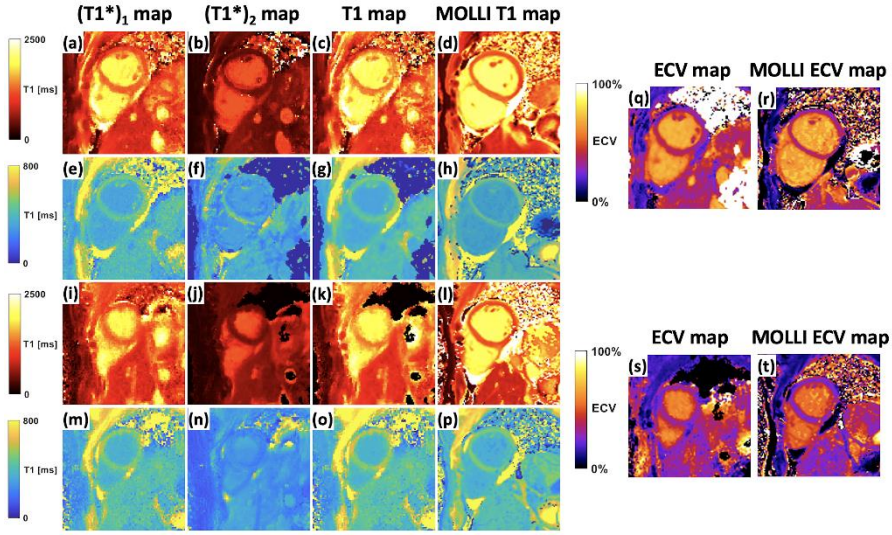

Figure 5.10 Human pre-contrast and post-contrast T1 map example. (a-d, i-l) are the short-axis basal and middle slices pre-contrast, and (e-h, m-p) are the analogous results post-contrast. The first two columns show the $(T_1^*)_1$ and $(T_1^*)_2$ maps, and T_1 maps from the proposed method in the third column are compared to MOLLI T_1 maps in the fourth column. (q, s) are the proposed base and mid ECV maps, compared to MOLLI ECV maps in (r, t). The mean myocardium ECV value from proposed technique is 25.9%, comparing to 25.0% from MOLLI ECV map.

Figure 5.11 shows the T_1 maps from a pre-contrast whole-heart coverage subject. Images from the top row are the T_1 maps using the proposed method. The bottom row images are MOLLI

T_1 maps in the corresponding slice locations, where some banding artifacts can be seen in the inferolateral region.

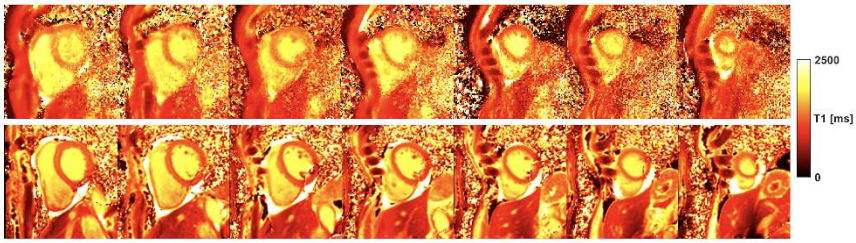

Figure 5.11 Whole-heart coverage pre-contrast human T1 map example. Images in the top row show the proposed method T_1 maps from base (left) to apex (right). The bottom row images demonstrate the MOLLI T_1 maps from corresponding slices.

The pre- and post-contrast myocardium T_1 mean values across the basal slice from all the subjects for MOLLI and the proposed method are shown in the Bland-Altman plots in Figure 5.12. There is a mean bias of 94 ms for the proposed strategy compared to MOLLI results for native T_1 and a mean bias of 38 ms in post-contrast maps. Slice profile correction resulted in an increase of the native T_1 compared to the ones with no slice profile correction by 25 ms.

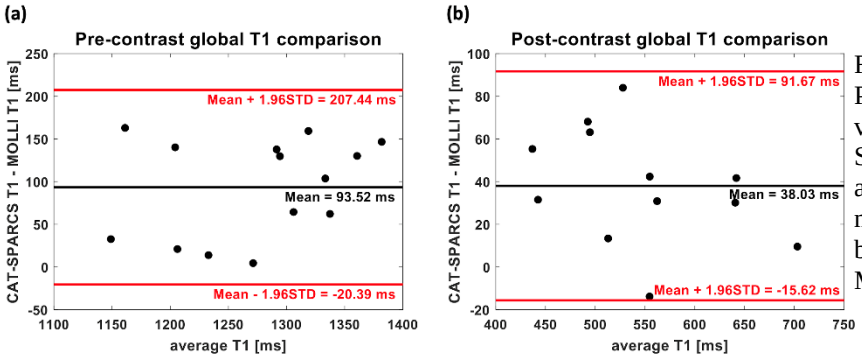

Figure 5.12 T_1 Bland-Altman plots. (a) Pre-contrast global myocardium T_1 value comparison between CAT-SPARCS technique and MOLLI across all subjects. (b) Post-contrast global myocardium T_1 value comparison between CAT-SPARCS technique and MOLLI across all subjects.

5.4.7 Evaluation of LGE maps

Figure 5.13 demonstrates the LGE results from 2 patients. The first patient on the top row has a scar in the basal inferior region, while the second patient on the bottom shows a scar in the basal inferoseptal region. Both of the proposed (Figure 5.13(a)) and synthetic (Figure 5.13(b)) LGE images show good agreement with breath-hold ECG-gated PSIR LGE images (Figure 5.13(c)).

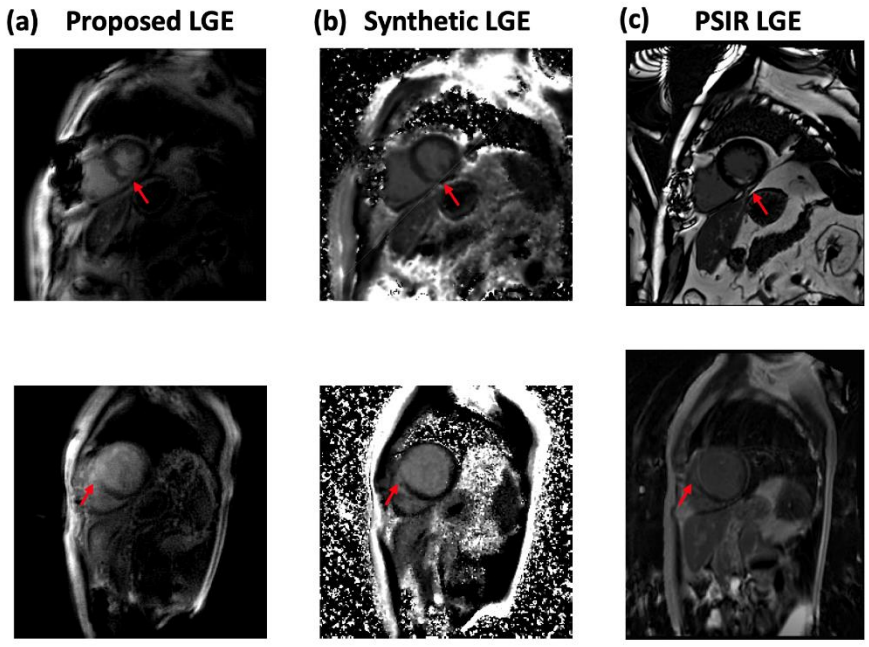

Figure 5.13 LGE results from 2 patients. (a) shows the proposed LGE image. (b) shows the synthetic LGE image generated using the post T_1 map. (c) shows the reference PSIR LGE image.

5.5 Discussion

In this work, we proposed and developed a free-breathing and cardiac self-gated dual excitation flip angle continuous spiral strategy (CAT-SPARCS 2FAs) to simultaneously obtain T_1 maps and cine images. This method eliminates the need for ECG monitoring and breath-holds, requires no accessory acquisitions such as a B_1^+ map, and provides a novel approach for continuous acquisition for T_1 mapping when both flip angle bias and apparent T_1^* recovery need to be corrected. The total acquisition time for the current implementation is approximately 30 seconds per slice.

In this study, there is an 8% bias of the native T_1 values between MOLLI and CAT-SPARCS 2FAs in in-vivo experiments, which can be explained by several factors. Although MOLLI is commonly used in clinic settings and has high precision and reproducibility, its accuracy can be affected by a number of factors including T_2, off-resonance and magnetization transfer effects. In addition, the Look-Locker correction using the 3-parameter model depends on inversion

efficiency. Previous studies also demonstrated that MOLLI tends to underestimate T_1 for high T_1 values and higher heart rates [147–149].

For a Look-Locker type acquisition, the magnetization is allowed to recover back to thermal equilibrium following data acquisition, before the next inversion pulse. In this scheme, the actual T_1 value can be obtained from the apparent T_1 (T_1^*) by utilizing Look-Locker correction. We have utilized this technique previously [150], which resulted in good quality T_1 maps and cine images. However, this type of acquisition is less efficient because it requires waiting for the magnetization to recover to thermal equilibrium between inversion pulses. Furthermore, it is more challenging to perform accurate self-gating with an intermittent acquisition scheme. Based on the relationship between the actual T_1 and T_1^* from the original Look-Locker paper [143], it is impossible to accurately recover T_1 from T_1^* without knowledge of the flip angle if one does not wait for the magnetization to recover to its equilibrium value. In this case, a B_1^+ map needs to be acquired to correct T_1^* to obtain correct T_1 values. In the multi-tasking technique, a low flip angle was utilized and the flip angle parameter was tightly constrained during the T_1 fitting [151]. This assumes minimal effects from B_1^+ inhomogeneity and could result in biases in the actual fitting of T_1, as a 4-parameter fit is used for a T_1 recovery model that has only 3 degrees of freedom. For example, for a TR of 3.6 ms, a T_1 value of 1200 ms, and when the flip angle (5°) is reduced by 20% (4°) because of slice profile and B_1^+ effect, the estimated T_1 bias using the 4-parameter fit could be as much as 100 ms in the setting of no noise and using all points along the curve. Alternatively, if a separate scan such as B_1^+ mapping was performed, this extra mapping may cause potential issues with motion correction and cardiac trigger synchronization, especially for a free-breathing and self-gating acquisition.

We proposed that B_1^+ and slice profile corrected T_1 values can be obtained from a single continuous acquisition by acquiring continuous Look-Locker trains with two flip angles. The flip angle bias and apparent T_1 effect can be distinguished by iteratively fitting T_1 and β values using look-up tables that includes slice profile effect with at least two reasonably chosen flip angles. Our simulations indicate that, for the range of T_1 values expected for cardiac T_1 mapping, this should include the combination of a small flip angle to sensitize the T_1^* recovery to T_1 and a large flip angle to sensitize the T_1^* recovery to B_1^+ differences. In this study, we acquired the low (3°) and high (15°) flip angle images both before and after contrast. If post-contrast cine images are not desired, the pre-contrast β map could be used to correct the post-contrast T_1 maps derived from the 3° flip angle post-contrast images. An inherent advantage of acquiring both flip angles pre- and post-contrast is that the T_1 and β maps are co-registered, and any biases between the acquisitions can be accounted for. In terms of application of the proposed strategy, for a non-contrast study, this technique would yield cine and native T_1 maps. The technique could also be performed following contrast to look at cine and post-contrast T_1 map, which can be used to assess LGE either directly as we have shown previously [152] or through the generation of synthetic LGE images from T_1 maps.

For the proposed method at 3T, a spoiled-GRE strategy was chosen for the continuous acquisition. Compared with bSSFP imaging, spoiled-GRE readouts are not sensitive to banding artifacts or off-resonance out-of-plane flow artifacts. This strategy was chosen to simplify the acquisition so that a frequency scout would not be necessary, and so that the signal recovery would only depend on T_1 and flip angle, not on T_2 or off-resonance frequency. The spiral acquisition enables us to use a relatively long TR which results in improved inflow-enhancement of the LV blood pool in cine images, resulting in a contrast that is similar to that for Cartesian bSSFP cine

imaging rather than that for a short-TR Cartesian SP-GRE pulse sequence. For our cine reconstruction, we utilize the data from the higher flip angle which further improves myocardial-blood pool contrast.

The most challenging problem for cardiac imaging is the cardiac and respiratory motion during scanning. The MR fingerprinting technique [76], which can simultaneously quantify T_1 and T_2, resolves the cardiac and respiratory motion by using ECG triggering and breath-holds respectively. To simplify the acquisition, we proposed to synchronize the cardiac motion by using self-gating signals. Due to the high sampling efficiency of spiral imaging and flexible choice for *k*-space density, we can create low-resolution heart images using a combination of a sliding window approach and an automatic heart detection algorithm. Considering the intensity change during T_1 recovery, we focus on the heart region to eliminate the effect of T_1 recovery for other tissues in the chest. We demonstrate that PCA can effectively separate the inversion recovery signal from the cardiac and respiratory components. One challenging time point is the one right after the inversion pulses, when the signal is transitioning from negative to positive (around the null point). Theoretically, when there is no signal from the raw data it is difficult to derive a self-gated cardiac trigger. This fact might bias the extracted cardiac motion component right after the inversion pulses in some cases, especially for pre-contrast acquisition when the T_1 recovery is slower than that in post-contrast. Therefore, we corrected the triggers right after inversion pulses by linearly interpolating the neighboring triggers.

To deal with respiratory motion, some techniques, such as multi-tasking [151], treat it as an additional dimension in addition to the cardiac-motion and T_1-recovery dimensions, and attempts to resolve them simultaneously. However, considering the entangled effects of cardiac motion, respiratory motion and T_1 recovery in the raw data, there is no guarantee that these dimensions can

be perfectly separated using this approach. Therefore, it may be more accurate and efficient to resolve the respiratory motion first. Besides, compared to the multi-tasking technique, which used the respiratory motion dimension information to separate the data into different breathing states, our method implemented rigid registration to correct breathing motion for each heart beat independently. Our approach assumes that respiratory motion within each heartbeat is relatively small. When there is no significant through-plane motion, instead of using a non-rigid registration method, rigid registration can be more stable with less computation time [32]. For 2D imaging the effects of through-plane motion cannot be corrected. One possibility is to reject out-of-plane data based on the image correlation matrix [153].

There are also several limitations for the current 2FAs strategy. First of all, linear interpolation might cause bias at the self-gating triggers right after inversion pulses for arrhythmic patients. To overcome this issue, a strategy to reject any R-R interval that is significantly different from the mean R-R interval can be implemented; however, this may require a longer acquisition time to obtain enough data for final reconstruction. Currently, we are reconstructing cine images only using the data from the steady-state portion of the recovery from the high flip angle images. This produces a bright-blood image contrast similar to the SPARCS technique [134]. However, a reconstruction utilizing all of the data to simultaneously determine T_1 maps and cine imaging may improve efficiency and enable shorter acquisitions. Secondly, although inflow effect can improve the contrast for cine images, there might be some bias of the pre-contrast blood pool T_1 values. One possible way to overcome this issue could be to model the inflow effect in the dictionary, which would increase the computation burden and time, and requires assumptions regarding the inflow effects across the cardiac cycle. While we show good agreement with MOLLI for myocardial T_1, with a bias of 94 ms for native T_1, further experiments using a more accurate in-

vivo gold standard sequence such as SASHA [14] are warranted. MOLLI is known to under-estimate T_1 values as compared to SASHA. Furthermore, in this study we generated the coil sensitivity map using the time-averaged data, which is widely used in CMR applications. However, the effects of respiratory motion on the fidelity of the CSM could potentially be further improved by generating coil sensitivity maps for each R-R interval and applying the inverse transformation to the coil sensitivities as shown for brain imaging by Bammer et al. [154], or by inserting the motion operator in the image domain within the encoding operator.

5.6 Conclusion

A free-breathing, self-gated, IR-based acquisition using dual excitation flip angles and continuous golden-angle spiral trajectories, CAT-SPARCS 2FAs, was presented to obtain T_1 maps, cine images and LGE images with clinically acceptable spatial and temporal resolution, without ECG monitoring or breath-holds. The dual excitation flip angle approach to deal with flip angle bias including B_1^+ and slice profile effect, and the apparent T_1 effect provides new insights for continuously acquired T_1 mapping. It may provide a simpler and more efficient protocol for clinical CMR imaging, which would greatly reduce the work and time associated with CMR imaging protocols. In the future, this technique can be extended to a 3D or simultaneous multi-slice (SMS) acquisition, which would further accelerate scanning efficiency.

Chapter 6: B1-corrected single excitation flip angle acquisition of T1 maps and comparison to dual excitation flip angle acquisition

6.1 Introduction

Cardiac T_1 maps have demonstrated the ability to assess both focal and diffuse myocardial processes in cardiomyopathy [155,156]. However, to use a continuous Look-Locker acquisition, where cardiac self-gating can be achieved, both B_1^+ and slice profile effects[157,158] need to be considered to quantify T_1. In Chapter 5, we proposed a technique to obtain T_1 and flip-angle-scale maps in a single free-breathing self-gated continuous IR-based acquisition using dual excitation flip angles[159] (CAT-SPARCS 2FAs). Previously, Sacolick et al. have proposed a B_1^+ mapping technique by Bloch-Siegert shift, where it encodes the B_1^+ information into signal phase. To further improve T_1 mapping accuracy, we proposed a Bloch-Siegert B_1^+-corrected single flip angle acquisition under free-breathing and cardiac self-gating (1FA+B_1^+), and compare it with the previous technique.

6.2 Methods

6.2.1 Image acquisition

As shown in Figure 6.1, for Bloch-Siegert shift (BS) B_1^+ mapping [145], data were acquired continuously with golden-angle rotated spiral trajectories for 2 seconds. An off-resonance Fermi pulse was applied between the slice rewinder and the readout-gradient lobes. To minimize motion effects during acquisition, positive and negative off-resonance pulses are interleaved for each spiral trajectory. For T_1^* mapping, following an IR RF pulse, golden-angle spiral trajectories are

acquired continuously over 4 seconds using a spoiled-GRE pulse sequence. This pattern is repeated 4 times. In the 2FAs approach, the IR acquisition is repeated with a second flip angle.

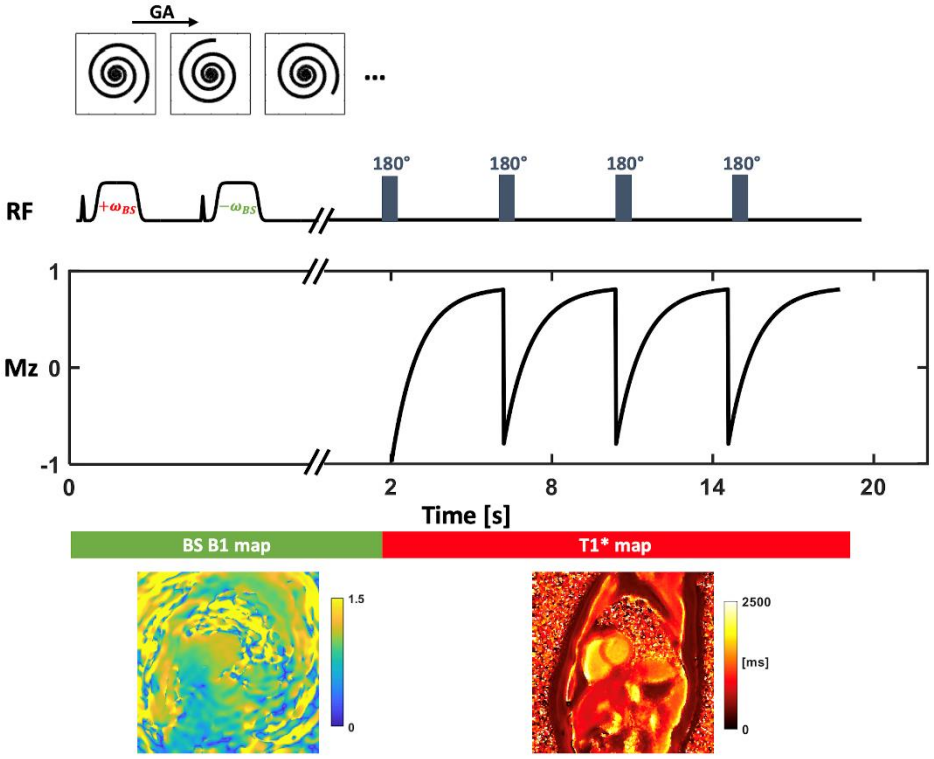

Figure 6.1 Schematic of the acquisition. Data in the first two seconds acquired with off-resonance Fermi pulses were used to reconstruct the Bloch-Siegert B_1^+ map. Data acquired with repetitive inversion pulses were used to reconstruct the T_1^* map.

6.2.2 Image reconstruction

For the BS B_1^+ map, images were reconstructed using NUFFT [39] and Walsh coil combination [100]. The BS frequency shift is generated by irradiating with an off-resonance RF pulse following spin excitation. The phase shift can be expressed as [145]:

$$\phi_{BS} = B_{1,peak}^2 \int_0^{T_{pulse}} \frac{(\gamma B_{1,norm}(t))^2}{2\omega_{BS}(t)} dt = B_{1,peak}^2 \cdot K_{BS}, \quad (6.1)$$

where $B_{1,peak}$ is the magnitude of the maximum point in the RF waveform B_1, and the factor K_{BS} can be computed as a function of the normalized BS pulse shape $B_{1,norm}(t)$ with duration T_{pulse}, the off-resonance $\omega_{BS}(t)$ and the gyro-magnetic ratio γ.

The positive (I_+) and negative (I_-) off-resonance images are proportional to the magnitude of the magnetization M, the background phase ϕ_0, and the BS phase ϕ_{BS}, whose phase images are shown in (Figure 6.2(a)). The two images be formulated as [160]:

$$I_+ \propto |M|e^{j(\phi_0+\phi_{BS})}, \tag{6.2}$$

$$I_- \propto |M|e^{j(\phi_0-\phi_{BS})}, \tag{6.3}$$

Thus, the B_1^+ map (Figure 6.2(b)) is given as the peak value of the BS pulse $B_{1,peak}$:

$$B_{1,peak} = \sqrt{\frac{\arg(I_+/I_-)}{2K_{BS}}} = \sqrt{\frac{\phi_{BS}}{K_{BS}}}, \tag{6.4}$$

For the T_1^* map, self-gating cardiac triggers were extracted from a sliding-window heart image navigator (Figure 6.2(d,e)). Respiratory motion correction was performed by rigidly registering the original image with its corresponding synthetic image that is generated from PCA, as they share similar image contrast (Figure 6.2(f)). Then, the T_1^* map was obtained by fitting the 3-parameter model using dictionary learning (Figure 6.2(g)) reconstructed images as described previously [159]. Furthermore, so as to align the heart location of the acquired B_1^+ map and the generated T_1^* map, a rigid registration was performed on the magitude images from BS B_1^+ mapping and the T_1^* map around the heart ROI.

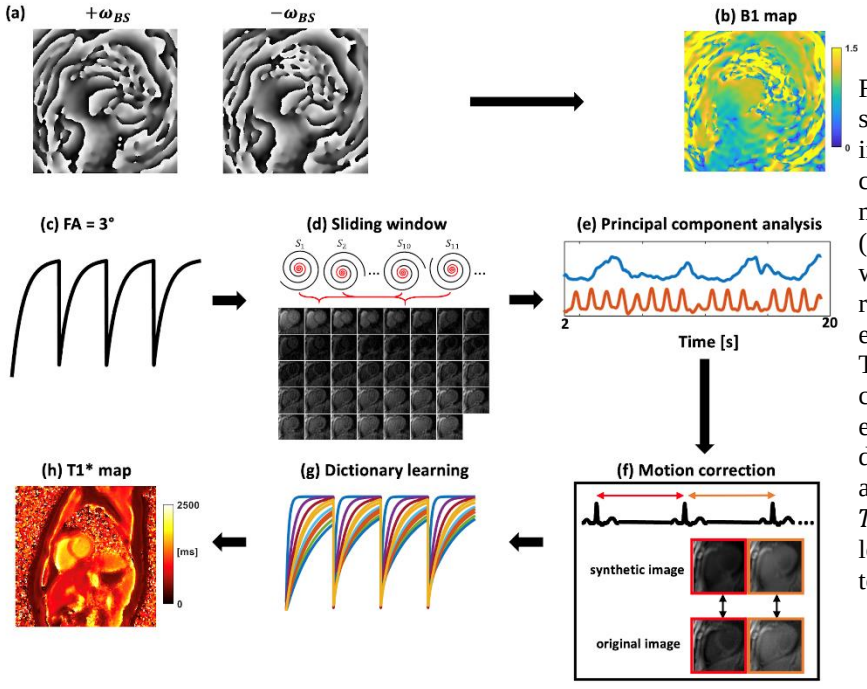

Figure 6.2 Image processing strategy. Positive and negative phase images (a) were extracted to calculate the Bloch-Siegert shift B_1^+ map (b). Data with inversion pulses (c) firstly performed a sliding window approach to generate a low-resolution image navigator (d) to extract self-gated cardiac trigger (e). Then, respiratory motion was corrected by rigid registration on each heartbeat (f). Next, one dictionary is generated based on the acquisition parameters and varying T_1 and B_1^+ values. Dictionary learning reconstruction is performed to create the T_1^* map (h).

In order to account for slice profile and B_1^+ effects, firstly the dictionaries were generated by simulating 200 isochromats across the actual slice profile (time-bandwidth [TBW] = 5.4). Then, 200 isochromats were simulated with the proposed acquisition parameters across the slice profile for a range of T_1 values from 200 ms to 2500 ms and B_1^+ scales from 0.4 to 1.2 to create a look up table including slice profile effects. Finally, a T_1 map was generated by using the B_1^+ map, T_1^* map as well as the look-up table.

6.2.3 Phantom study

Imaging experiments were performed at 3T (MAGNETOM Prisma, Siemens Healthineers, Erlangen, Germany) in the T1MES phantom [142]. The proposed strategy (1FA+B_1^+) and the previous technique (2FAs) were performed and compared to IR-SE, MOLLI [12] and SASHA [11] T_1 maps. The sequence parameters of 1FA, 2FA, IR-SE and MOLLI are the same as shown in Chapter 5.3.6. For SASHA T_1 mapping, parameters included: FOV = 340 mm, resolution = 1.5 × 1.5 × 8 mm^3, TR/TE = 2.9/1.24 ms, flip angle = 70°, GRAPPA with R=2, 7/8 partial Fourier. Images were acquired during an end-diastolic window of 167 ms. The ECG signal was simulated on the scanner at a heart rate of 60 beats per minute during the experiments.

For BS B_1^+ maps were acquired with the following parameters: Fermi pulse duration = 8 ms, off-resonance shift = ±4 kHz, K_{BS} = 79.73 rad/G^2, $B_{1,peak}$ = 0.0544 G; FOV = 340 mm, spatial resolution = 1.5 × 1.5 × 8 mm^3, TR/TE = 40.2/9.14 ms, flip angle = 15°, and reconstructed with 10 × 10 × 8 mm^3 spatial resolution. For T_1^* mapping, parameters included: TR/TE = 8.35/1.45 ms, RF pulse TBW = 5.4, FOV = 340 mm, spatial resolution = 1.5 ×1.5 × 8 mm^3, flip angle = 3°.

6.2.4 In-vivo study

Imaging experiments were performed at 3T (MAGNETOM Prisma or Skyra, Siemens Healthineers, Erlangen, Germany) in 3 healthy volunteers and 10 patients undergoing clinically

ordered CMR, including 2 coronary artery disease patients, 1 pulmonary atresia patient, 2 diabetes patients and 5 cardiomyopathy patients. Among them, healthy volunteers only performed pre-contrast scans, while patients received gadolinium (Gd)–based contrast agents (Gadoteric acid – Gadoterate meglumine, Clariscan GE Healthcare) during the scan to perform both pre- and post-contrast acquisitions. Both short-axis base and middle slices are acquired. All subjects gave written informed consent or consented through phone calls, and imaging studies were performed under institutional review board (IRB) approved protocols. The proposed strategy (1FA+B_1^+) and the previous technique (2FAs) were performed and compared to MOLLI [12] and SASHA [11] T_1 maps. Sequence parameters are the same as those in phantom experiments. The T_1 values were compared by drawing ROIs in different tubes (phantom) and the regions of myocardium and blood pool (human subjects).

6.2.5 Image analysis

To analyze the phantom T_1 results, circular ROIs were drawn for each tube. The mean and standard deviation of T_1 values were compared among the mentioned four techniques. A Bland-Altman plot T_1 values was made to compare the techniques with IR-SE method. The in-vivo T_1 values were measured by drawing ROIs on myocardium and blood pool in basal short-axis slice, and then plot in bar plots. Two-way ANOVA was used to perform the statistical test with considering the variance across the subjects. Image reconstruction, processing and statistical analysis were performed using MATLAB (The Mathworks Inc., Natick, MA).

6.3 Results

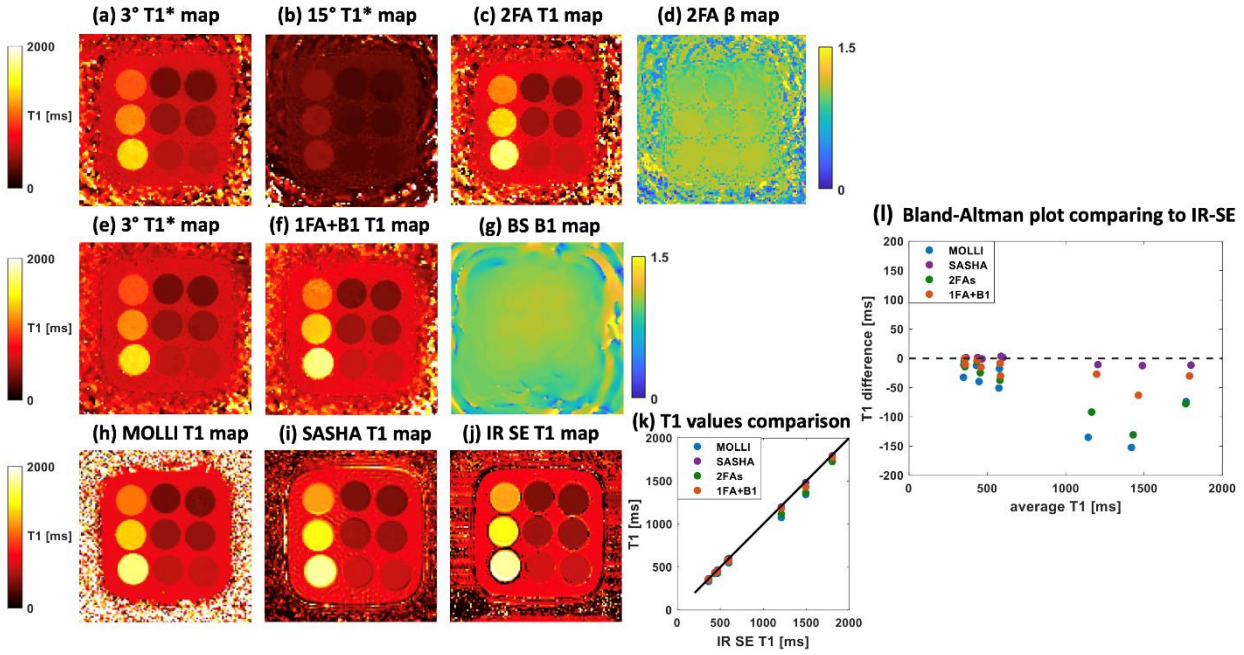

Figure 6.3 Phantom results. 3° (a) and 15° (b) T_1^* maps are used to generate 2FAs T_1 map (c) and flip angle scale β map (d) as described in the previous literature. 3° T_1^* map (e) and Bloch-Siegert shift B1 map (g) are used to generate 1FA+B1 T_1 map (f). The proposed T_1 maps are compared to MOLLI (h), SASHA(i) and IR-SE (j) T_1 maps. T_1 values across 9 ROIs in each tube among the four techniques are compared in (k), where the x axis corresponds to the gold-standard IR-SE T_1 values. (l) shows the Bland-Altman plot comparing the 4 techniques with IR-SE.

Figure 6.3 shows the phantom results of 1FA+B_1^+ and 2FA techniques, compared to results from MOLLI, SASHA and IR-SE. The phantom T_1 values of 9 tubes from 1FA+B_1^+ and 2FAs are in close agreement with the IR-SE results (Figure 6.3(k)). 2FAs, 1FA+B_1^+ and SASHA showed better agreements with IR-SE compared to MOLLI. For 1FA+B_1^+ technique, the highest bias for the long T_1 tube is less than 5%.

Figure 6.4 shows results from one healthy volunteer for short-axis basal (Figure 6.4(a)) and middle (Figure 6.4(b)) slices for 2FAs and 1FA+B_1^+ techniques, compared to MOLLI and SASHA T_1 maps. Figure 6.5 shows results from one patient for short-axis basal slices of pre- (Figure 6.5(a)) and post-contrast (Figure 6.5(b)) for 2FAs and 1FA+B_1^+ techniques, compared to MOLLI and SASHA T_1 maps.

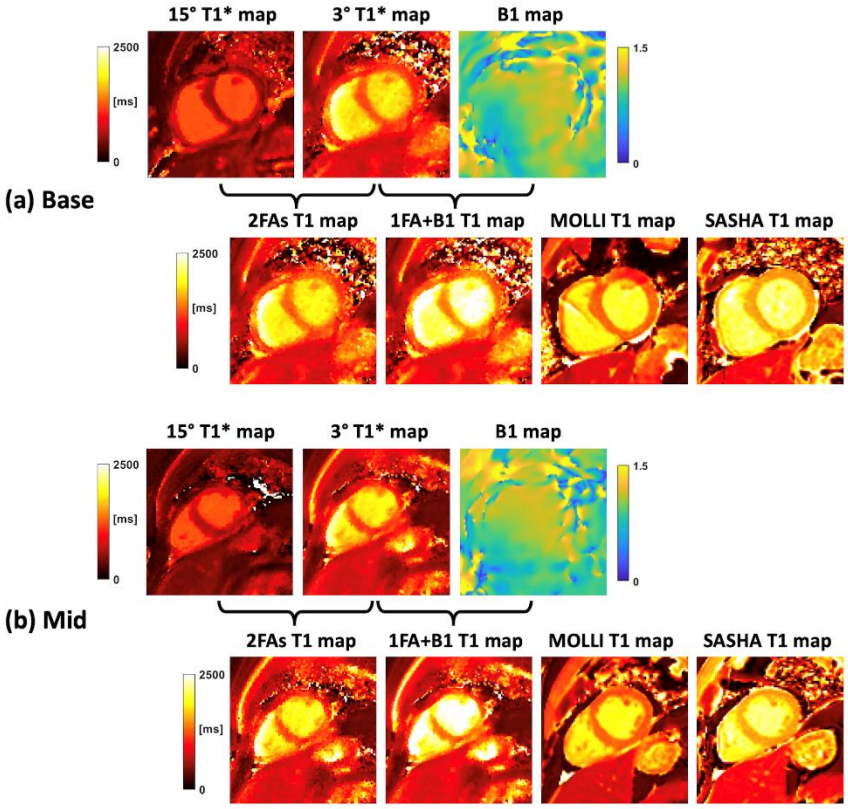

Figure 6.4 Healthy volunteer example. Short-axis basal (a) and middle (b) slices from one healthy volunteer are shown. As indicated by the bracket, 3° and 15° T_1^* maps are used to generate the 2FAs T_1 map, while 3° T_1^* and BS B1 maps are used to generate the 1FA+B1 T_1 map. MOLLI and SASHA T_1 maps are also shown as comparison.

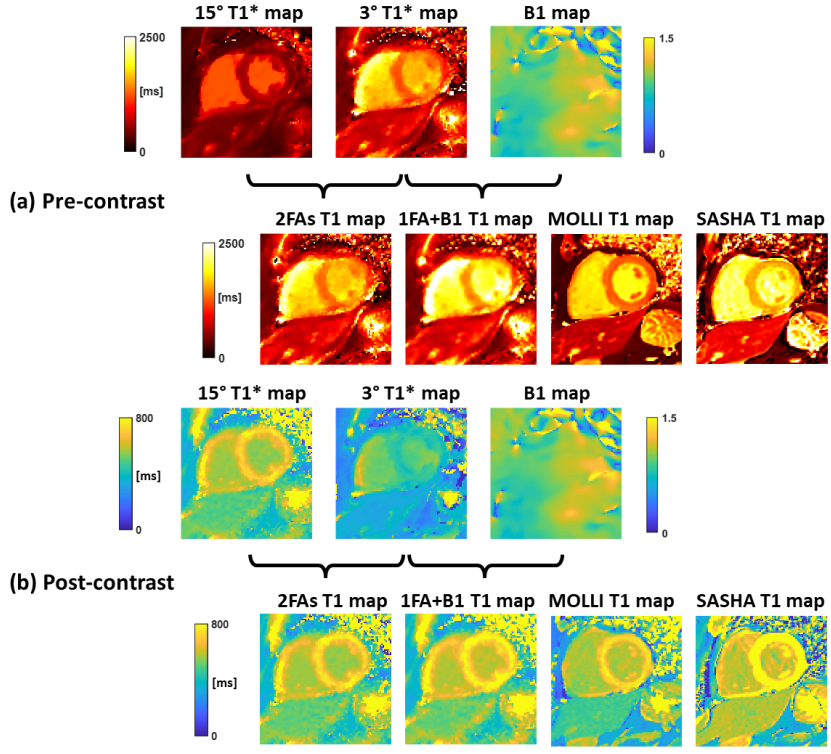

Figure 6.5 Patient example. Short-axis basal slices of pre-(a) and post-contrast (b) from one patient are shown. As indicated by the bracket, 3° and 15° T_1^* maps are used to generate the 2FAs T1 map, while 3° T_1^* and BS B1 maps are used to generate the 1FA+B1 T_1 map. MOLLI and SASHA T_1 maps are also shown as comparison.

Figure 6.6 compares the T_1 values for myocardium and blood pool among the four mentioned techniques for healthy volunteers. The myocardium T_1 values for 1FA+B_1^+ were more similar to those from SASHA T_1 maps, which are known to more closely match IR-SE as compared to MOLLI, which tends to underestimate T_1 values, especially in pre-contrast studies. However, the blood pool T_1 values from 2FA and 1FA+B_1^+ techniques might suffer from some inflow effects.

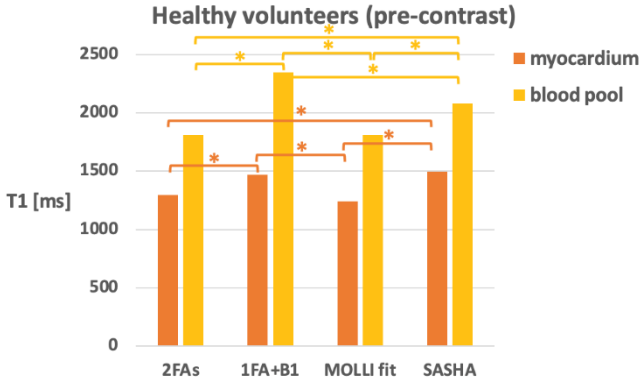

Figure 6.6 T_1 quantifications for healthy volunteers.

Similar comparisons are made on the patient group in Figure 6.7 for both pre- and post-contrast results. For pre-contrast results, although there is a significant difference in myocardial T_1 values among the techniques, 1FA+B_1^+ technique results get closer to SASHA results compared to 2FAs and MOLLI. For blood pool T_1 values, there is an over-estimate of T_1 values in 1FA+B_1^+ results, which might due to the inflow effects. For post-contrast results, similar results can be visualized.

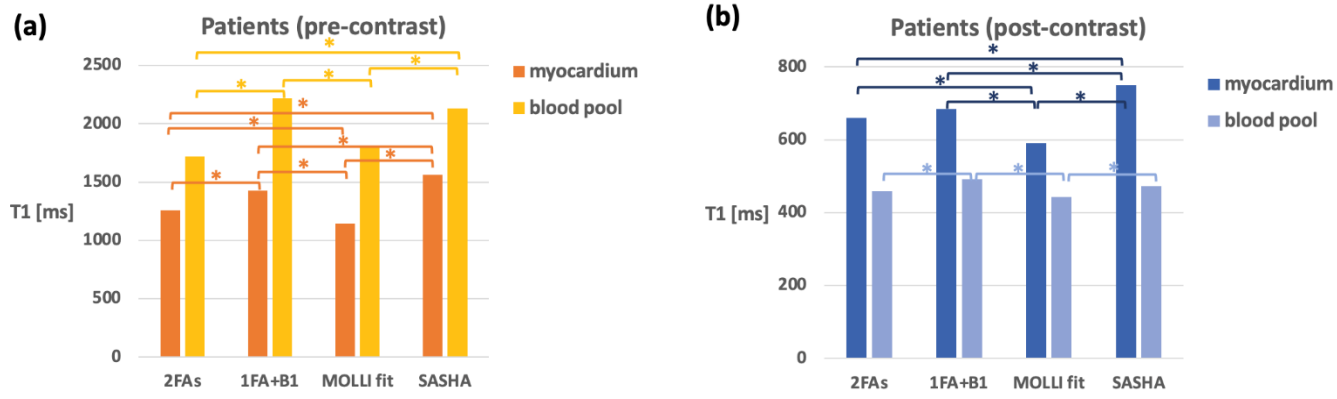

Figure 6.7 (a) Pre-contrast T_1 quantification for patients. (b) Post-contrast T_1 quantification for patients.

6.4 Discussion

We developed a strategy to acquire B_1^+ and T_1 maps in a free-breathing, continuous inversion-recovery spiral acquisition. This provides another method to measure T_1 using a continuous Look-Locker acquisition as compared to the dual excitation flip angle technique described in Chapter 5. For phantom results, both 1FA+B_1^+ and 2FAs techniques are more accurate than MOLLI by comparing to the gold-standard IR-SE. For in-vivo studies of both healthy volunteers and patients' groups, myocardial T_1 values from both 1FA+B_1^+ and 2FAs techniques were more similar to the standard breath-held SASHA technique than those from MOLLI, demonstrating increased accuracy in measuring T_1. In addition, 1FA+B_1^+ myocardial T_1 values are closer to SASHA than those of 2FAs. This might due to the separately acquired accurate B_1 maps of 1FA+B_1^+ technique. Furthermore, in terms of pre- and post-contrast acquisitions, at the same slice position, 1FA+B_1^+ technique only requires one acquisition of B_1^+ map. Lastly, in the future studies, we need to design a $10 \times 10 \times 8$ mm^3 spatial resolution B_1^+ mapping acquisition, to further improve SNR and shorten acquisition time.

However, there are also some disadvantages using 1FA+B_1^+ technique. Firstly, since we only acquired the data to generate small flip angle (3°) T_1^* map, unlike 2FAs strategy, 1FA+B_1^+ technique, due to the low flip angle, does not produce high-quality cine and LGE images during the acquisition. Moreover, for both 2FAs and 1FA+B_1^+ approaches the blood pool T_1 values are biased to different extents, which might be affected by in-flow effects in the blood pool region. 2FAs technique acquires the data to generate 3° and 15° T_1^* maps. Given that both images are sensitive to inflow effects, it appears that the bias in the blood pool may be partially mitigated when generating the final T_1 map. Therefore, the T_1 values in the blood pool of 1FA+B_1^+ technique might suffer more from inflow effects compared to 2FAs, especially for pre-contrast images.

Lastly, 1FA+B_1^+ technique requires a motion-correction strategy between B_1^+ and T_1^* maps. This is less reliable than 2FAs strategy, where image registration is performed on similar images.

6.5 Conclusion

In a single acquisition, a free breathing Bloch-Siegert shift B_1^+ map, and a self-gated B_1^+ and slice profile corrected T_1 map are acquired. This technique is compared to our prior dual-flip angle approach and yields more accurate T_1 values in the myocardium.

Chapter 7: Conclusions and future work

7.1 Overview of findings

The overall goal of this dissertation was to achieve an efficient and easily operated multi-contrast cardiac imaging technique. We first developed a respiratory motion correction strategy, which automatically detected the heart ROI, and corrected motion for under-sampled Cartesian first-pass perfusion imaging. After it was evaluated with numerical phantom and clinical patients, this simple and robust rigid motion compensation strategy greatly reduced motion artifacts and improved image quality for the standard k-t PCA and k-t SLR techniques in the setting of respiratory motion.

Next, we applied this strategy to spiral trajectory cine imaging. In this project, we designed a continuous golden-angle rotated spiral acquisition strategy (SPARCS) to acquire cine images without breath-holding and ECG-gating. We have implemented it with both 3T (spoiled-GRE readout) and 1.5T (bSSFP readout) scanners. This strategy was evaluated in both healthy volunteers and clinical patients. It successfully imaged cardiac function without the need for ECG-gating or breath-holding. With an 8-second data acquisition per slice, whole heart cine images with clinically acceptable spatial and temporal resolution and image quality can be acquired in less than 90 seconds of free-breathing acquisition.

Furthermore, to obtain cine images and T_1 maps in a single free-breathing acquisition, we developed a golden-angle spiral acquisition that cycles through a waiting period at the beginning followed by intermittent IR pulses. Here, T_1 maps were generated by dictionary learning reconstruction using the whole recovery curve, while cine images were reconstructed from the part where the signal has approached steady state. By testing in in-vivo subjects, T_1 values from the

proposed method were comparable to the standard MOLLI sequence, and the cine images show good image quality compared to standard clinical-used cine images.

In order to achieve the multi-contrast imaging under both free-breathing and no ECG-gating, we developed a free-breathing cardiac self-gated technique that provides cine images, B_1^+ and slice profile corrected T_1 maps, and LGE images from a single acquisition. For this project, we designed a continuous golden-angle gradient-echo spiral pulse sequence with an inversion RF pulse applied every four seconds. 3° and 15° flip angles were used for readouts after the first four and second four inversions (2FAs). Self-gating cardiac triggers were successfully extracted from heart image navigators and respiratory motion was corrected by rigid registration on each heartbeat. Cine images were reconstructed from the steady state portion of 15° readouts using L+S reconstruction. T_1 maps were fit using a projection onto convex sets approach from images reconstructed using slice profile corrected dictionary learning. LGE images were reconstructed from the signal changing portion of 15° readouts after last three IR pulses. This strategy was evaluated with a phantom and 14 human subjects. For phantom, it demonstrated good agreement with IR-SE. As expected, higher T_1 values were observed than MOLLI in human subjects.

Lastly, we developed a technique to acquire accurate B_1^+ and T_1 maps (1FA+B_1^+) in a free-breathing, cardiac self-gated, continuous Look-Locker, inversion-recovery acquisition and compared it to the 2FAs approach. During the first 2 seconds, off-resonance Fermi pulses were applied to generate a Bloch-Siegert shift B_1^+ map, while later data was acquired with an inversion RF pulse applied every four seconds to create T_1^* map. The final T_1 map was generated with the B_1^+ map and T_1^* map by using a look-up table to account for slice profile effects and yield more accurate T_1 values. This 1FA+B_1^+ and the previously mentioned 2FAs approaches were evaluated in phantom, healthy volunteers, and clinical patients. Both techniques showed good agreement

with IR-SE in phantom; however, 1FA+B_1^+ myocardial T_1 values were closer to SASHA than MOLLI and 2FAs.

7.2 Future directions

7.2.1 3D free breathing cardiac self-gated cine imaging

Compared to 2D imaging, 3D imaging can improve the SNR from volume averaging effects and provide opportunities to under-sample the k-space data along the slice direction with various approaches. Taking the advantage of the 2D SPARCS acquisition strategy, we can develop a 3D Stack-of-Spiral SPARCS sequence to further accelerate cine imaging with higher SNR. Figure 7.1 shows a preliminary result of 3D Stack-of-Spiral, golden-angle rotated continuous acquisition that was fully sampled in the slice direction. The sequence design is similar as the 2D SPARCS strategy in terms of spatial and temporal resolution, except it uses 3D acquisition. Each slice data was first generated by applying Fourier Transform on the slice direction. Then, for each slice, respiratory motion was corrected by rigid registration on the low-resolution images generated with the data from each heartbeat, and ECG was used to gate the cardiac motion. In order to extract cardiac self-gating signals from the data, some under-sampling strategy along the slice direction can be implemented. In that way, we can repeatedly acquire the center partition every certain number of outer partitions.

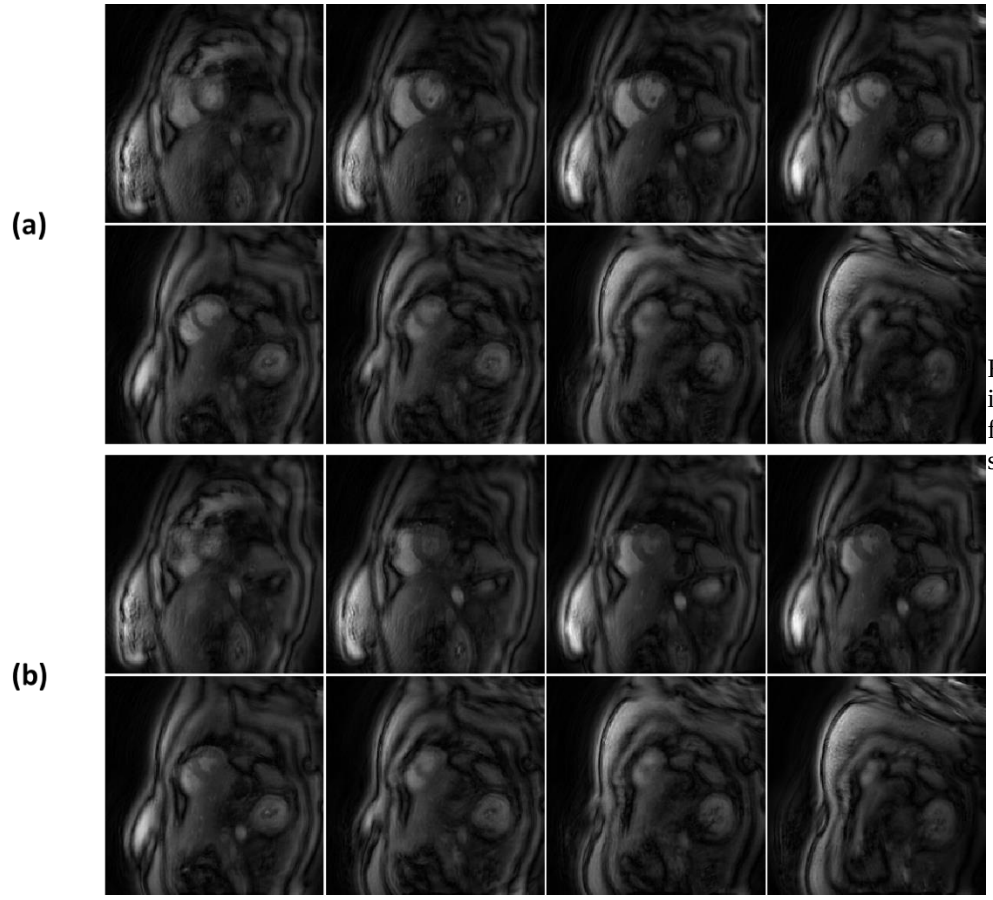

Figure 7.1 3D SPARCS images at end-diastolic frame (a) and end-systolic frame (b).

7.2.2 B1-corrected variable flip angle T_1 mapping

The variable flip angle (VFA) approach has been proposed previously [161] to perform T_1 mapping in the brain. Firstly, the SPGR signal can be written as:

$$S_{SPGR} = \frac{M_o(1-E_1)\sin\alpha}{1-E_1\cos\alpha}, \tag{7.1}$$

where $E_1 = e^{-TR/T1}$. Once we re-write this equation, we can form a linear model as:

$$\frac{S_{SPGR}}{\sin\alpha} = E_1\frac{S_{SPGR}}{\tan\alpha} + M_o(1-E_1), \tag{7.2}$$

Next, by keeping the TR constant and only varying the flip angle, we can use the linear regression model to solve for the two unknowns: T_1 and M_o. In order to compensate for the B_1 effect, instead of directly solving Equation 7.2, we firstly generated a look-up table of the SPGR signals with varying T_1 and B_1 values for each flip angle. Then a look-up table of the SPGR signal ratio between the two flip angles with various T_1 and B_1 can be calculated. Therefore, we can generate a T_1 map with two flip angle SPGR images and a B_1 map in a pixel-by-pixel fitting. Figure 7.2 shows a preliminary result of VFA T_1 mapping for a phantom. In this 2D case, the T_1 values from the VFA approach are in good agreement with MOLLI and SASHA results.

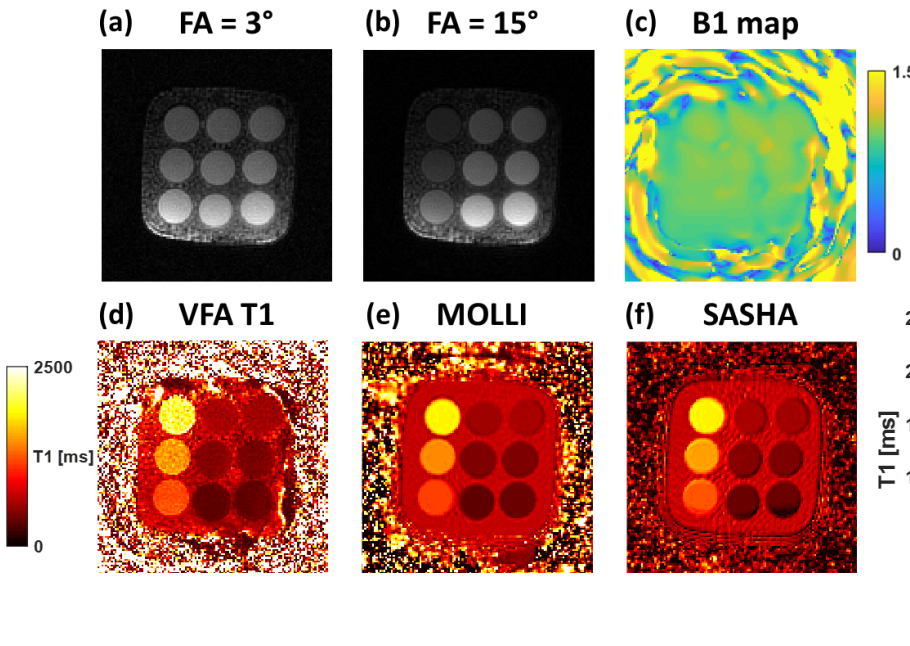

Figure 7.2 2D Phantom VFA T1 map. (a) SPARCS acquisition with flip angle = 3°. (b) SPARCS acquisition with flip angle = 15°. (c) Bloch-Siegert B1 map. (d) B1-corrected VFA T1 map. (e) MOLLI T1 map. (f) SASHA T1. (g) T1 comparison of 9 tubes across the 3 techniques.

7.2.3 Conclusion

The 2D SPARCS and CAT-SPARCS techniques developed in this dissertation provide the framework for further development of these applications in 3D or using SMS. The VFA technique may be a good choice for 3D self-gated imaging, because the slice profile effect of center slices may be less severe. The challenges to performing 3D self-gated imaging might lie in the design of the under-sampling pattern in the partition direction, in order to both obtain the self-gating signals

with enough temporal resolution and sufficient *k*-space data to reconstruct high-quality images throughout the 3D volume. While free breathing 3D imaging may present new challenges for respiratory motion correction, the benefit of 3D imaging is that it may be possible to correct through-plane motion, which cannot be corrected for 2D imaging. However, in order to achieve 3D motion correction, a more sophisticated motion correction strategy, rather than rigid motion correction, may need to be considered.

Appendix

First-author Journal Publications

1. **Zhou R**, Weller DS, Yang Y, Wang J, Jeelani H, Mugler JP, Salerno M. Dual excitation flip angle simultaneous Cine And T1 mapping using SPiral Acquisition with Respiratory and Cardiac Self-gating (CAT-SPARCS). Magn Reson Med. 2021; 86 (1); 82-96.
2. **Zhou R**, Yang Y, Mathew RC, Mugler JP, Weller DS, Kramer CM, Ahmed AH, Jacob M, Salerno M. Free-breathing cine imaging with motion-corrected reconstruction at 3T using SPiral Acquisition with Respiratory correction and Cardiac Self-gating (SPARCS). Magn Reson Med. 2019; 82 (2); 706-720.
3. **Zhou R**, Huang W, Yang Y, Chen X, Weller DS, Kramer CM, Kozerke S, Salerno S. Simple motion correction strategy reduces respiratory-induced motion artifacts for k-t accelerated and compressed-sensing cardiovascular magnetic resonance perfusion imaging. Journal of Cardiovascular Magnetic Resonance. 2018; 20 (1); 1-13.

Co-authored Journal Publications

1. Wang J, Yang Y, Weller DS, **Zhou R**, Sun C, Epstein FH, Meyer CH, Kramer CM, Salerno M. Ultra-high spatial resolution spiral first-pass myocardial perfusion imaging with whole-heart coverage at 3 T. Magn Reson Med. 2021.
2. Ahmed AH, **Zhou R**, Yang Y, Nagpal P, Salerno M, Jacob M. Free-breathing and ungated dynamic MRI using navigator-less spiral SToRM. IEEE Transactions on Medical Imaging. 2020; 39 (12); 3933-3943.

First-author Conference Publications

1. **Zhou R**, Weller DS, Yang Y, Wang J, Mugler J, Salerno M. Comparison of free-breathing self-gated continuous IR spiral T1 mapping: dual flip angle versus Bloch-Siegert B1-corrected techniques. ISMRM 29th Annual Meeting & Exhibition. 2021 May; Online Exhibition.
2. **Zhou R**, Weller DS, Yang Y, Wang J, Salerno M. Slice profile correction in 2D free-breathing spiral cardiac self-gated dual excitation flip-angle continuous Look-Locker T1 mapping. SCMR 24th Annual Meeting & Exhibition. 2021 Feb; Online Exhibition.
3. **Zhou R**, Weller DS, Yang Y, Wang J, Salerno M. Free-breathing continuous cine and T1 mapping acquisition using a motion-corrected dual flip angle inversion-recovery spiral technique at 3T. ISMRM 28th Annual Meeting & Exhibition. 2020 Aug; Online Exhibition.
4. **Zhou R**, Yang Y, Wang Z, Feng X, Meyer CH, Mugler JP, Weller DS, Salerno M. bSSFP and GRE based cine imaging using Spiral Acquisition with Respiratory correction and Cardiac Self-gating (SPARCS) at 1.5T. SCMR 23rd Annual Scientific Sessions. 2020 Feb; Orlando, FL, USA
5. **Zhou R**, Weller DS, Yang Y, Wang J, Mugler JP. Salerno M. Single Acquisition of Cine images and T1 Maps using a Free-breathing Respiratory Motion-corrected Spiral Technique at 3T. SCMR 23rd Annual Scientific Sessions. 2020 Feb; Orlando, FL, USA
6. **Zhou R**, Yang Y, Weller DS, Ahmed AH, Mugler JP, Jacob M, Salerno M. Inversion Recovery Cardiac and Respiratory Self-gated Simultaneous Acquisition of Cine and LGE Images Using a Golden-angle Spiral Pulse Sequence. ISMRM 27th Annual Meeting & Exhibition. 2019 May; Montreal, Canada.

7. **Zhou R**, Yang Y, Mathew R, Salerno M. Cardiac and Respiratory Self-Gated Motion-Corrected Free-breathing Spiral Cine Imaging. ISMRM 26th Annual Meeting & Exhibition; 2018 June; Paris, France.

8. **Zhou R**, Yang Y, Houten MJV, Kramer CM, Salerno M. Cardiac and Respiratory Self-Gated Motion-Corrected Free-breathing Spiral Cine Imaging. SCMR 21st Annual Scientific Sessions. 2018 Jan; Barcelona, Spain.

Co-authored Conference Publications

1. Wang J, Yang Y, **Zhou R**, Sun C, Jacob M, Weller DS, Epstein FH, Salerno M. High resolution spiral simultaneous multi-slice first-pass perfusion imaging with whole-heart coverage at 1.5T and 3T. ISMRM 28th Annual Meeting & Exhibition. 2020 Aug; Online Exhibition.

2. Jeelani H, Yang Y, **Zhou R**, Kramer CM, Salerno M, Weller DS. A myocardial T1-mapping framework with recurrent and u-net convolutional neural networks. IEEE 17th International Symposium on Biomedical Imaging (ISBI). 2020 Apr; Online Exhibition, 1941-1944.

3. Wang J, Yang Y, **Zhou R**, Jacob M, Weller DS, Salerno M. SMS Slice L1-SPIRiT: auto-calibrated image reconstruction for spiral simultaneous multi-slice first-pass perfusion imaging with 1.25 mm resolution and whole heart coverage at 3T. SCMR 23rd Annual Scientific Sessions. 2020 Feb; Orlando, FL, USA

4. Wang Z, Feng X, Yang Y, **Zhou R**, Salerno M, Meyer CH. High Resolution Real-time Cine with Whole Heart Coverage in half a minute. ISMRM 27th Annual Meeting & Exhibition. 2019 May; Montreal, Canada.

5. Ahmed AH, Mohsin Y, **Zhou R**, Yang Y, Salerno M, Jacob M. Navigator-less Spiral SToRM for Free breathing and Ungated Cardiac CINE MRI. SCMR 22nd Annual Scientific Sessions. 2019 Feb; Bellevue, WA, USA

6. Feng X, Yang Y, **Zhou R**, Robinson AA, Meyer CH, Salerno M. Fully automatic LV segmentation on myocardial first-pass perfusion images. SCMR 22nd Annual Scientific Sessions. 2019 Feb; Bellevue, WA, USA

Patents

1. **Zhou R**, Yang Y, Salerno M. Cardiac and Respiratory Self-Gated Motion-Corrected Free-Breathing Spiral Cine Imaging. US Patent Application 2019/0154785 A1

2. Salerno M, **Zhou R**, Weller DS, Mugler J. System and method for dual excitation flip angle simultaneous cine and T1 mapping using spiral acquisition with respiratory and cardiac self-gating (CAT-SPARCS). US Patent Application No. 63/149,979

Bibliography

1. Yancy, C. W. *et al.* 2013 ACCF/AHA guideline for the management of heart failure: A report of the American college of cardiology foundation/american heart association task force on practice guidelines. *J. Am. Coll. Cardiol.* **62**, e147–e239 (2013).
2. Mozaffarian, D. *et al. Heart disease and stroke statistics-2016 update a report from the American Heart Association*. *Circulation* vol. 133 (2016).
3. Benjamin, E. J. *et al. Heart Disease and Stroke Statistics—2018 Update: A Report From the American Heart Association*. *Circulation* (2018). doi:10.1161/CIR.0000000000000558.
4. Arena, R. *et al.* Assessment of functional capacity in clinical and research settings: A scientific statement from the American Heart Association committee on exercise, rehabilitation, and prevention of the council on clinical cardiology and the council on cardiovascular n. *Circulation* **116**, 329–343 (2007).
5. Pappano, A. J. & Wier, W. G. *Cardiovascular physiology, 10th edition*. (2013).
6. Liu, J. M. *et al.* Measurement of myocardial native T1 in cardiovascular diseases and norm in 1291 subjects. *J. Cardiovasc. Magn. Reson.* **19**, 1–10 (2017).
7. Puntmann, V. O. *et al.* Native T1 mapping in differentiation of normal myocardium from diffuse disease in hypertrophic and dilated cardiomyopathy. *JACC Cardiovasc. Imaging* **6**, 475–484 (2013).
8. Karamitsos, T. D. & Neubauer, S. T1 mapping and amyloid cardiomyopathy: How much better can it get? *Eur. Heart J.* **36**, 203–205 (2015).
9. Mongeon, F. P. *et al.* Quantification of extracellular matrix expansion by CMR in infiltrative heart disease. *JACC Cardiovasc. Imaging* **5**, 897–907 (2012).
10. Look, D. C. & Locker, D. R. Time saving in measurement of NMR and EPR relaxation

times. *Rev. Sci. Instrum.* **41**, 250–251 (1970).

11. Chow, K. *et al.* Saturation recovery single-shot acquisition (SASHA) for myocardial T1 mapping. *Magn. Reson. Med.* **71**, 2082–2095 (2014).
12. Messroghli, D. R. *et al.* Modified look-locker inversion recovery (MOLLI) for high-resolution T 1 mapping of the heart. *Magn. Reson. Med.* **52**, 141–146 (2004).
13. Look, D. C. & Locker, D. R. Nuclear spin-lattice relaxation measurements by tone-burst modulation. *Phys. Rev. Lett.* **20**, 987–989 (1968).
14. Chow, K. *et al.* Saturation Recovery Single-Shot Acquisition (SASHA) for Myocardial T 1 Mapping. *Magn. Reson. Med.* 2082–2095 (2014) doi:10.1002/mrm.24878.
15. Kim, R. J. *et al.* The use of contrast-enhanced magnetic resonance imaging to identify reversible myocardial dysfunction. *N. Engl. J. Med.* 1445–1453 (2000).
16. Gulati, A. *et al.* The prevalence and prognostic significance of right ventricular systolic dysfunction in nonischemic dilated cardiomyopathy. *Circulation* **128**, 1623–1633 (2013).
17. Kuruvilla, S. *et al.* Late gadolinium enhancement on cardiac magnetic resonance predicts adverse cardiovascular outcomes in nonischemic cardiomyopathy: A systematic review and meta-analysis. *Circ. Cardiovasc. Imaging* **7**, 250–257 (2014).
18. Robinson, A. A., Chow, K. & Salerno, M. Myocardial T1 and ECV Measurement: Underlying Concepts and Technical Considerations. *JACC Cardiovasc. Imaging* **12**, 2332–2344 (2019).
19. Brooks, J., Kramer, C. M. & Salerno, M. Markedly increased volume of distribution of gadolinium in cardiac amyloidosis demonstrated by T1 mapping. *J. Magn. Reson. Imaging* **38**, 1591–1595 (2013).
20. Karamitsos, T. D. *et al.* Noncontrast T1 mapping for the diagnosis of cardiac amyloidosis.

JACC Cardiovasc. Imaging **6**, 488–497 (2013).

21. Fontana, M. *et al.* Native T1 mapping in transthyretin amyloidosis. *JACC Cardiovasc. Imaging* **7**, 157–165 (2014).
22. Puntmann, V. O. *et al.* Native T1 and ECV of Noninfarcted Myocardium and Outcome in Patients With Coronary Artery Disease. *J. Am. Coll. Cardiol.* **71**, 766–778 (2018).
23. Fontana, M. *et al.* Prognostic value of late gadolinium enhancement cardiovascular magnetic resonance in cardiac amyloidosis. *Circulation* **132**, 1570–1579 (2015).
24. Rehwald, W. G., Fieno, D. S., Chen, E. L., Kim, R. J. & Judd, R. M. Myocardial magnetic resonance imaging contrast agent concentrations after reversible and irreversible ischemic injury. *Circulation* **105**, 224–229 (2002).
25. Fieno, D. S. *et al.* Contrast-enhanced magnetic resonance imaging of myocardium at risk: Distinction between reversible and irreversible injury throughout infarct healing. *J. Am. Coll. Cardiol.* **36**, 1985–1991 (2000).
26. Vöhringer, M., Mahrholdt, H., Yilmaz, A. & Sechtem, U. Significance of late gadolinium enhancement in Cardiovascular Magnetic Resonance Imaging (CMR). *Herz Kardiovaskuläre Erkrankungen* **32**, 129–137 (2007).
27. Kramer, C. M. The Role of CMR in Cardiomyopathies. *J Nucl Med* **56**, 39–45 (2015).
28. Salerno, M. & Beller, G. A. Noninvasive assessment of myocardial perfusion. *Circ. Cardiovasc. Imaging* **2**, 412–424 (2009).
29. Wolff, S. D. *et al.* Myocardial first-pass perfusion magnetic resonance imaging: A multicenter dose-ranging study. *Circulation* **110**, 732–737 (2004).
30. Vasanawala, S. S. *et al.* Practical parallel imaging compressed sensing MRI: Summary of two years of experience in accelerating body MRI of pediatric patients. *Proc. - Int. Symp.*

Biomed. Imaging 1039–1043 (2011) doi:10.1109/ISBI.2011.5872579.

31. Levine, E., Daniel, B., Vasanawala, S., Hargreaves, B. & Saranathan, M. 3D Cartesian MRI with compressed sensing and variable view sharing using complementary poisson-disc sampling. *Magn. Reson. Med.* **77**, 1774–1785 (2017).

32. Zhou, R. *et al.* Simple motion correction strategy reduces respiratory-induced motion artifacts for k-t accelerated and compressed-sensing cardiovascular magnetic resonance perfusion imaging. *J. Cardiovasc. Magn. Reson.* **20**, 1–13 (2018).

33. Mansfield, P. Multi-planar image formation using NMR spin echoes. *J Phys C Solid State Phys* **10**, 55–58 (1977).

34. Salerno, M., Sica, C. T., Kramer, C. M. & Meyer, C. H. Optimization of spiral-based pulse sequences for first-pass myocardial perfusion imaging. *Magn. Reson. Med.* **65**, 1602–1610 (2011).

35. Feng, X., Salerno, M., Kramer, C. M. & Meyer, C. H. Non-Cartesian balanced steady-state free precession pulse sequences for real-time cardiac MRI. *Magn. Reson. Med.* **75**, 1546–1555 (2016).

36. Meyer, C. H. & Hu, P. Spiral parallel magnetic resonance imaging. in *28th IEEE EMBS Annual International Conference* 369–371 (2006).

37. Tan, H. & Meyer, C. H. Estimation of k -space trajectories in spiral MRI. *Magn Reson Med* **61**, 1396–1404 (2012).

38. Feng, X. Dynamic MRI: Techniques and Applications. (2012).

39. Fessler, J. A. On NUFFT-based gridding for non-Cartesian MRI. *J Magn Reson.* **188**, 191–195 (2007).

40. Firmin, D. & Keegan, J. Navigator echoes in cardiac magnetic resonance. *J. Cardiovasc.*

Magn. Reson. **3**, 183–193 (2001).

41. Jung, B., Zaitsev, M., Hennig, J. & Markl, M. Navigator gated high temporal resolution tissue phase mapping of myocardial motion. *Magn. Reson. Med.* **55**, 937–942 (2006).

42. Peters, D. C., Nezafat, R., Eggers, H., Stehning, C. & Manning, W. J. 2D free-breathing dual navigator-gated cardiac function validated against the 2D breath-hold acquisition. *J. Magn. Reson. Imaging* **28**, 773–777 (2008).

43. Abd-Elmoniem, K. Z. *et al.* Free Breathing Single Navigator Gated Cine Cardiac Magnetic Resonance at 3 Tesla : Feasibility Study in Patients. *J Comput Assist Tomogr.* **35**, 382–386 (2011).

44. Moghari, M. H., Barthur, A., Amaral, M. E., Geva, T. & Powell, A. J. Free-breathing whole-heart 3D cine magnetic resonance imaging with prospective respiratory motion compensation. *Magn. Reson. Med.* **189**, 181–189 (2017).

45. Stehning, C., Bornert, P., Nehrke, K., Eggers, H. & Stuber, M. Free-breathing whole-heart coronary MRA with 3D radial SSFP and self-navigated image reconstruction. *Magn. Reson. Med.* **54**, 476–480 (2005).

46. Lai, P., Bi, X., Jerecic, R. & Li, D. A Dual-Projection Respiratory Self-Gating Technique for Whole-Heart Coronary MRA. *Magn. Reson. Med.* **62**, 731–738 (2009).

47. Lai, P., Bi, X., Jerecic, R. & Li, D. A respiratory self-gating technique with 3D-translation compensation for free-breathing whole-heart coronary MRA. *Magn. Reson. Med.* **62**, 731–738 (2009).

48. Usman, M. *et al.* Motion corrected compressed sensing for free-breathing dynamic cardiac MRI. *Magn. Reson. Med.* **70**, 504–516 (2013).

49. Pang, J. *et al.* Whole-heart coronary MRA with 100% respiratory gating efficiency: Self-

navigated three-dimensional retrospective image-based motion correction (TRIM). *Magn. Reson. Med.* **71**, 67–74 (2014).

50. Usman, M., Ruijsink, B., Nazir, M. S., Cruz, G. & Prieto, C. Free breathing whole-heart 3D CINE MRI with self-gated Cartesian trajectory. *Magn. Reson. Imaging* **38**, 129–137 (2017).

51. Liu, J. *et al.* Respiratory and cardiac self-gated free-breathing cardiac CINE imaging with multiecho 3D hybrid radial SSFP acquisition. *Magn. Reson. Med.* **63**, 1230–1237 (2010).

52. Pang, J. *et al.* ECG and navigator-free four-dimensional whole-heart coronary MRA for simultaneous visualization of cardiac anatomy and function. *Magn. Reson. Med.* **72**, 1208–1217 (2014).

53. Batchelor, P. G. *et al.* Matrix description of general motion correction applied to multishot images. *Magn. Reson. Med.* **54**, 1273–1280 (2005).

54. Rao, A. *et al.* Comparison of cardiac motion across subjects using non-rigid registration. *Med. Image Comput. Comput. Interv. — MICCAI 2002* **2488**, 722–729 (2002).

55. Rueckert, D., Lorenzo-valdt, M., Chandrashekara, R. & Mohiaddin, R. Non-rigid registration of cardiac MR: application to motion modelling and atlas-based segmentation. in *Proceedings IEEE International Symposium on Biomedical Imaging* 6–9 (IEEE, 2002). doi:10.1109/ISBI.2002.1029299.

56. Royuela-Del-Val, J., Cordero-Grande, L., Simmross-Wattenberg, F., Martin-Fernandez, M. & Alberola-Lopez, C. Nonrigid groupwise registration for motion estimation and compensation in compressed sensing reconstruction of breath-hold cardiac cine MRI. *Magn. Reson. Med.* **75**, 1525–1536 (2016).

57. Crowe, M. E. *et al.* Automated rectilinear self-gated cardiac cine imaging. *Magn. Reson. Med.* **52**, 782–788 (2004).

58. Buehrer, M., Curcic, J., Boesiger, P. & Kozerke, S. Prospective self-gating for simultaneous compensation of cardiac and respiratory motion. *Magn. Reson. Med.* **60**, 683–690 (2008).

59. Larson, A. C. *et al.* Self-Gated Cardiac Cine MRI. *Magn. Reson. Med.* **51**, 93–102 (2004).

60. Han, F., Rapacchi, S. & Hu, P. Prospective cardiac motion self-gating. *Quant Imaging Med Surg* **2**, 215–226 (2017).

61. Bonanno, G., Hays, A. G., Weiss, R. G. & Schär, M. Self-gated golden angle spiral cine MRI for coronary endothelial function assessment. *Magn. Reson. Med.* **00**, 1–11 (2017).

62. Odille, F. *et al.* Model-based reconstruction for cardiac cine MRI without ECG or breath holding. *Magn. Reson. Med.* **63**, 1247–1257 (2010).

63. Brau, A. C. S. & Brittain, J. H. Generalized self-navigated motion detection technique: Preliminary investigation in abdominal imaging. *Magn. Reson. Med.* **55**, 263–270 (2006).

64. Uribe, S. *et al.* Whole-heart cine MRI using real-time respiratory self-gating. *Magn. Reson. Med.* **57**, 606–613 (2007).

65. Larson, A. C. *et al.* Preliminary investigation of respiratory self-gating for free-breathing segmented cine MRI. *Magn. Reson. Med.* **53**, 159–168 (2005).

66. Pruessmann, K. P., Weiger, M., Scheidegger, M. B. & Boesiger, P. SENSE: Sensitivity encoding for fast MRI. *Magn. Reson. Med.* **42**, 952–962 (1999).

67. Griswold, M. A. *et al.* Generalized Autocalibrating Partially Parallel Acquisitions (GRAPPA). *Magn. Reson. Med.* **47**, 1202–1210 (2002).

68. Lustig, M. & Pauly, J. M. SPIRiT: Iterative self-consistent parallel imaging reconstruction from arbitrary k-space. *Magn. Reson. Med.* **64**, 457–471 (2010).

69. Lustig, M. & Donoho, D. Compressed sensing MRI. *IEEE Signal Process. Mag.* 72–82 (2008).

70. Candès, E. J. & Recht, B. Exact matrix completion via convex optimization. *Found. Comput. Math.* **9**, 717–772 (2009).

71. Otazo, R., Candès, E. & Sodickson, D. K. Low-rank plus sparse matrix decomposition for accelerated dynamic MRI with separation of background and dynamic components. *Magn. Reson. Med.* **73**, 1125–36 (2015).

72. Doneva, M. *et al.* Compressed Sensing Reconstruction for Magnetic Resonance Parameter Mapping. *Magn. Reson. Med.* **1120**, 1114–1120 (2010).

73. Ravishankar, S. & Bresler, Y. MR image reconstruction from highly undersampled k-space data by dictionary learning. *IEEE Trans. Med. Imaging* **30**, 1028–1041 (2011).

74. Zhu, Y. *et al.* Integrated motion correction and dictionary learning for free-breathing myocardial T1 mapping. *Magn. Reson. Med.* **81**, 2644–2654 (2019).

75. Ma, D. *et al.* Magnetic resonance fingerprinting. *Nature* **495**, 187–192 (2013).

76. Hamilton, J. I. *et al.* MR Fingerprinting for Rapid Quantification of Myocardial T1, T2, and Proton Spin Density. *Magn. Reson. Imaging* **1458**, 1446–1458 (2017).

77. Qi, H. *et al.* Free-running simultaneous myocardial T1/T2 mapping and cine imaging with 3D whole-heart coverage and isotropic spatial resolution. *Magn. Reson. Imaging* **63**, 159–169 (2019).

78. Christodoulou, A. G. *et al.* Magnetic resonance multitasking for motion-resolved quantitative cardiovascular imaging. *Nat. Biomed. Eng.* **2**, 215–226 (2018).

79. Crawley, A. P. & Henkelman, R. M. A comparison of one-shot and recovery methods in T1 imaging. *Magn. Reson. Med.* **7**, 23–34 (1988).

80. Atkinson, D. J., Burstein, D. & Edelman, R. R. First-pass cardiac perfusion: evaluation with ultrafast MR imaging. *Radiology* **174**, 757–762 (1990).

81. Angiography, C., J. Schwitter, MD; D. Nanz, PhD; S. Kneifel, MD; K. Bertschinger, MD; M. Büchi, M. & P.R. Knüsel, MD; B. Marincek, MD; T.F. Lüscher, MD; G.K. von Schulthess, MD, P. Assessment of Myocardial Perfusion in Coronary Artery Disease by Magnetic Resonance. *Circulation* **103**, 2230–2235 (2001).

82. Watkins, S. *et al.* Validation of magnetic resonance myocardial perfusion imaging with fractional flow reserve for the detection of significant coronary heart disease. *Circulation* **120**, 2207–2213 (2009).

83. Salerno, M. *et al.* Adenosine stress cardiovascular magnetic resonance with variable-density spiral pulse sequences accurately detects coronary artery disease initial clinical evaluation. *Circ. Cardiovasc. Imaging* **7**, 639–646 (2014).

84. Kellman, P. & Arai, A. E. Imaging Sequences for First Pass Perfusion—A Review. *J. Cardiovasc. Magn. Reson.* **9**, 525–537 (2007).

85. Kellman, P., Epstein, F. H. & McVeigh, E. R. Adaptive sensitivity encoding incorporating temporal filtering (TSENSE). *Magn. Reson. Med.* **45**, 846–852 (2001).

86. Breuer, F. A., Kellman, P., Griswold, M. A. & Jakob, P. M. Dynamic autocalibrated parallel imaging using temporal GRAPPA (TGRAPPA). *Magn. Reson. Med.* **53**, 981–985 (2005).

87. Tsao, J., Boesiger, P. & Pruessmann, K. P. k-t BLAST and k-t SENSE: Dynamic MRI With High Frame Rate Exploiting Spatiotemporal Correlations. *Magn. Reson. Med.* **50**, 1031–1042 (2003).

88. Pedersen, H., Kozerke, S., Ringgaard, S., Nehrke, K. & Won, Y. K. K-t PCA: Temporally constrained k-t BLAST reconstruction using principal component analysis. *Magn. Reson. Med.* **62**, 706–716 (2009).

89. Plein, S. *et al.* Dynamic contrast-enhanced myocardial perfusion MRI accelerated with k-t

SENSE. *Magn. Reson. Med.* **58**, 777–785 (2007).

90. Manka, R. *et al.* Clinical feasibility of accelerated, high spatial resolution myocardial perfusion imaging. *JACC Cardiovasc. Imaging* **3**, 710–717 (2010).

91. Jogiya, R. *et al.* Three-dimensional balanced steady state free precession myocardial perfusion cardiovascular magnetic resonance at 3T using dual-source parallel RF transmission: initial experience. *J. Cardiovasc. Magn. Reson.* **16**, (2014).

92. Lustig, Michael and Donoho, David L and Santos, Juan M and Pauly, J. M. Compressed sensing MRI. *Signal Process. Mag. IEEE* **25**, 72–82 (2008).

93. Adluru, G. *et al.* Acquisition and reconstruction of undersampled radial data for myocardial perfusion magnetic resonance imaging. *J. Magn. Reson. Imaging* **29**, 466–473 (2009).

94. Otazo, R., Kim, D., Axel, L. & Sodickson, D. K. Combination of compressed sensing and parallel imaging for highly accelerated first-pass cardiac perfusion MRI. *Magn. Reson. Med.* **64**, 767–776 (2010).

95. Sharif, B. *et al.* All-systolic non-ECG-gated myocardial perfusion MRI: Feasibility of multi-slice continuous first-pass imaging. *Magn. Reson. Med.* **74**, 1661–1674 (2015).

96. Feng, L., Sodickson, D. K. & Otazo, R. Rapid free-breathing dynamic contrast-enhanced MRI using motion-resolved compressed sensing. in *2015 IEEE 12th International Symposium on Biomedical Imaging (ISBI)* 889–892 (IEEE, 2015). doi:10.1109/ISBI.2015.7164013.

97. Plein, S. *et al.* High spatial resolution myocardial perfusion cardiac magnetic resonance for the detection of coronary artery disease. *Eur. Heart J.* **29**, 2148–2155 (2008).

98. Chen, X., Salerno, M., Yang, Y. & Epstein, F. H. Motion-compensated compressed sensing for dynamic contrast-enhanced MRI using regional spatiotemporal sparsity and region

tracking: Block low-rank sparsity with motion-guidance (BLOSM). *Magn. Reson. Med.* **72**, 1028–1038 (2014).

99. Smriti, R., Stredney, D., Schmalbrock, P. & Clymer, B. D. Image Registration Using Rigid Registration and Maximization of Mutual Information. in *MMVR13 (The 13th Annual Medicine Meets Virtual Reality Conference)* (2005).

100. Walsh, D. O., Gmitro, A. F. & Marcellin, M. W. Adaptive reconstruction of phased array MR imagery. *Magn. Reson. Med.* **43**, 682–690 (2000).

101. Cai, J.-F., Candes, E. J. & Shen, Z. A singular value thresholding algorithm for matrix completion. *Soc. Ind. Appl. Math.* **20**, 1956–1982 (2010).

102. Avants, B. B., Tustison, N. & Song, G. Advanced Normalization Tools (ANTS). *Insight J.* 1–35 (2009).

103. Jung, H., Sung, K., Nayak, K. S., Kim, E. Y. & Ye, J. C. K-t FOCUSS: A general compressed sensing framework for high resolution dynamic MRI. *Magn. Reson. Med.* **61**, 103–116 (2009).

104. Jung, H., Ye, J. C. & Kim, E. Y. Improved k-t BLAST and k-t SENSE using FOCUSS. *Phys. Med. Biol.* **52**, 3201–3226 (2007).

105. Wissmann, L., Santelli, C., Segars, W. P. & Kozerke, S. MRXCAT: Realistic numerical phantoms for cardiovascular magnetic resonance. *J. Cardiovasc. Magn. Reson.* **16**, 63 (2014).

106. Wang, Z., Bovik, A. C., Sheikh, H. R. & Simoncelli, E. P. Image quality assessment: From error visibility to structural similarity. *IEEE Trans. Image Process.* **13**, 600–612 (2004).

107. Asif, M. S., Hamilton, L., Brummer, M. & Romberg, J. Motion-adaptive spatio-temporal regularization for accelerated dynamic MRI. *Magn. Reson. Med.* **70**, 800–812 (2013).

108. Yang, Y. *et al.* Motion-corrected compressed-sensing enables robust spiral first-pass perfusion imaging with whole heart coverage. in *Journal of Cardiovascular Magnetic Resonance* vol. 16 (2014).

109. Keltner, J. R., Roos, M. S., Brakeman, P. R. & Budinger, T. F. Magnetohydrodynamics of blood flow. *Magn. Reson. Med.* **16**, 139–149 (1990).

110. Polson, M. J. R., Barker, A. T. & Gardiner, S. The effect of rapid rise-time magnetic fields on the ECG of the rat. *Clin. Phys. Physiol. Meas.* **3**, 231–234 (1982).

111. Shetty, A. N. Suppression of Radiofrequency Interference in Cardiac Gated MRI: A Simple Design. *Magn. Reson. Med.* **8**, 84–88 (1988).

112. Damji, A. A., Snyder, R. E., Ellinger, D. C., Witkowski, F. X. & Allen, P. S. RF interference suppression in a cardiac synchronization system operating in a high magnetic field NMR imaging system. *Magn. Reson. Imaging* **6**, 637–640 (1988).

113. Uribe, S. *et al.* Four-dimensional (4D) flow of the whole heart and great vessels using real-time respiratory self-gating. *Magn. Reson. Med.* **62**, 984–992 (2009).

114. Xue, Y. *et al.* Automatic coil selection for streak artifact reduction in radial MRI. *Magn. Reson. Med.* **67**, 470–476 (2012).

115. Feng, L. *et al.* RACER-GRASP: Respiratory-weighted, aortic contrast enhancement-guided and coil-unstreaking golden-angle radial sparse MRI. *Magn. Reson. Med.* **00**, (2017).

116. Klaas P. Pruessmann, Weiger, M., Peter, B. & Boesiger, P. Advances in Sensitivity Encoding With Arbitrary k-Space Trajectories. *Magn. Reson. Med.* **651**, 638–651 (2001).

117. Yang, Y., Kramer, C. M., Shaw, P. W., Meyer, C. H. & Salerno, M. First-pass myocardial perfusion imaging with whole-heart coverage using L1-SPIRiT accelerated variable density spiral trajectories. *Magn. Reson. Med.* **76**, 1375–1387 (2016).

118. Bland, J. M. & Altman, D. G. Statistical Methods for Assessing Agreement Between Two Methods of Clinical Measurement. *Lancet* **327**, 307–310 (1986).

119. Moghari, M. H., Komarlu, R., Annese, D., Geva, T. & Powell, A. J. Free-Breathing Steady-State Free Precession Cine Cardiac Magnetic Resonance with Respiratory Navigator Gating. *Magn. Reson. Med.* **73**, 1555–1561 (2015).

120. Chow, K., Yang, Y., Shaw, P., Kramer, C. M. & Salerno, M. Robust free-breathing SASHA T1mapping with high-contrast image registration. *J. Cardiovasc. Magn. Reson.* **18**, 1–14 (2016).

121. Xue, H. *et al.* Phase-sensitive inversion recovery for myocardial T1 mapping with motion correction and parametric fitting. *Magn. Reson. Med.* **69**, 1408–1420 (2014).

122. Moody, W. E. *et al.* Variability in cardiac MR measurement of left ventricular ejection fraction, volumes and mass in healthy adults: Defining a significant change at 1 year. *Br. J. Radiol.* **88**, (2015).

123. Malayeri, A. A., Johnson, W. C., Macedo, R., Lima, J. A. C. & Bluemke, D. A. Cardiac Cine MRI: Quantification of the Relationship Between Fast Gradient Echo and Steady-State Free Precession for Determination of Myocardial Mass and Volumes. *J Magn Reson Imaging* **28**, 60–66 (2008).

124. Noll, D. C., Pauly, J. M., Meyer, C. H., Nishimura, D. G. & Macovskj, A. Deblurring for non-2D fourier transform magnetic resonance imaging. *Magn. Reson. Med.* **25**, 319–333 (1992).

125. Nayak, K. S., Cunningham, C. H., Santos, J. M. & Pauly, J. M. Real-Time Cardiac MRI at 3 Tesla. *Magn. Reson. Med.* **51**, 655–660 (2004).

126. Harrison, A. *et al.* Rapid ungated myocardial perfusion cardiovascular magnetic resonance:

Preliminary diagnostic accuracy. *J. Cardiovasc. Magn. Reson.* **15**, 1–10 (2013).

127. Sudarski, S. *et al.* Free-breathing Sparse Sampling Cine MR Imaging with Iterative Reconstruction for the Assessment of Left Ventricular. *Radiology* **282**, (2017).

128. Sado, D. M. *et al.* Cardiovascular magnetic resonance measurement of myocardial extracellular volume in health and disease. *Heart* **98**, 1436–1441 (2012).

129. Moon, J. C. *et al.* Myocardial T1 mapping and extracellular volume quantification: A Society for Cardiovascular Magnetic Resonance (SCMR) and CMR Working Group of the European Society of Cardiology consensus statement. *J. Cardiovasc. Magn. Reson.* **15**, 1–12 (2013).

130. Tran-Gia, J., Stäb, D., Wech, T., Hahn, D. & Köstler, H. Model-based Acceleration of Parameter mapping (MAP) for saturation prepared radially acquired data. *Magn. Reson. Med.* **70**, 1524–1534 (2013).

131. Kecskemeti, S. *et al.* MPnRAGE: A technique to simultaneously acquire hundreds of differently contrasted MPRAGE images with applications to quantitative T 1 mapping. *Magn. Reson. Med.* **75**, 1040–1053 (2016).

132. Wang, X. *et al.* Model-based T1 mapping with sparsity constraints using single-shot inversion-recovery radial FLASH cardiovascular magnetic resonance. *J. Cardiovasc. Magn. Reson.* **79**, 730–740 (2018).

133. Tamir, J. I. *et al.* Computational MRI With Physics-Based Constraints: Application to Multicontrast and Quantitative Imaging. *IEEE Signal Process. Mag.* **37**, 94–104 (2020).

134. Zhou, R. *et al.* Free-breathing cine imaging with motion-corrected reconstruction at 3T using SPiral Acquisition with Respiratory correction and Cardiac Self-gating (SPARCS). *Magn. Reson. Med.* 1–15 (2019) doi:10.1002/mrm.27763.

135. Aharon, M., Elad, M. & Bruckstein, A. K -SVD: An Algorithm for Designing Overcomplete Dictionaries for Sparse Representation. *Signal Process. IEEE Trans.* **54**, 4311–4322 (2006).

136. Weller, D. S., Ramani, S. & Fessler, J. A. Augmented lagrangian with variable splitting for faster non-cartesian L1-SPIRiT MR image reconstruction. *IEEE Trans. Med. Imaging* **33**, 351–361 (2014).

137. Weing, S. *et al.* Temporally Resolved Parametric Assessment of Z-Magnetization Recovery (TOPAZ): Dynamic Myocardial T 1 Mapping Using a Cine Steady-State Look-Locker Approach. *Magn. Reson. Med.* **2100**, 2087–2100 (2018).

138. Becker, K. M., Schulz-Menger, J., Schaeffter, T. & Kolbitsch, C. Simultaneous high-resolution cardiac T1 mapping and cine imaging using model-based iterative image reconstruction. *Magn. Reson. Med.* **81**, 1080–1091 (2019).

139. Qi, H. *et al.* Free-running 3D whole heart myocardial T_1 mapping with isotropic spatial resolution. *Magn. Reson. Med.* mrm.27811 (2019) doi:10.1002/mrm.27811.

140. Ma, D. *et al.* Slice profile and B1 corrections in 2D magnetic resonance fingerprinting. *Magn. Reson. Med.* **78**, 1781–1789 (2017).

141. Heule, R., Pfeuffer, J., Meyer, C. H. & Bieri, O. Simultaneous B1 and T1 mapping using spiral multislice variable flip angle acquisitions for whole-brain coverage in less than one minute. *Magn. Reson. Med.* **81**, 1876–1889 (2019).

142. Captur, G. *et al.* A T1 and ECV phantom for global T1 mapping quality assurance: The T1 mapping and ECV standardisation in CMR (T1MES) program. *J. Cardiovasc. Magn. Reson.* **18**, 1–4 (2016).

143. Deichmann, R., Haase, A. & Hubland, A. Quantification of Tl Values by SNAPSHOT-FLASH NMR Imaging. *J. Magn. Reson.* **612**, 608–612 (1992).

144. Varga-Szemes, A. *et al.* Myocardial late gadolinium enhancement: Accuracy of t1 mapping-based synthetic inversion-recovery imaging. *Radiology* **278**, 374–382 (2016).

145. Sacolick, L. I., Wiesinger, F., Hancu, I. & Vogel, M. W. B1 mapping by Bloch-Siegert shift. *Magn. Reson. Med.* **63**, 1315–1322 (2010).

146. Kellman, P., Arai, A. E., Mcveigh, E. R. & Aletras, A. H. Phase-Sensitive Inversion Recovery for Detecting Myocardial Infarction Using Gadolinium-Delayed Hyperenhancement. *Magn. Reson. Med.* **383**, 372–383 (2002).

147. Heidenreich, J. F. *et al.* T1- and ECV-mapping in clinical routine at 3 T: Differences between MOLLI, ShMOLLI and SASHA. *BMC Med. Imaging* **19**, 1–9 (2019).

148. Roujol, S. *et al.* Accuracy, precision, and reproducibility of four T1 mapping sequences: A headto-head comparison of MOLLI, ShMOLLI, SASHA, and SAPPHIRE. *Radiology* **272**, 683–689 (2014).

149. Piechnik, S. K. *et al.* Shortened Modified Look-Locker Inversion recovery (ShMOLLI) for clinical myocardial T1-mapping at 1.5 and 3 T within a 9 heartbeat breathhold. *J. Cardiovasc. Magn. Reson.* **12**, (2010).

150. Zhou, R. *et al.* Single Acquisition of Cine Images and T1 Maps using a Free-breathing Respiratory Motion-corrected Spiral Technique at 3T. in *SCMR 23rd Annual Scientific Sessions* (2020).

151. Shaw, J. L. *et al.* Free-breathing, non-ECG, continuous myocardial T_1 mapping with cardiovascular magnetic resonance Multitasking. *Magn. Reson. Med.* 1–14 (2018) doi:10.1002/mrm.27574.

152. Zhou, R. *et al.* Inversion Recovery Cardiac and Respiratory Self-gated Simultaneous Acquisition of Cine and LGE Images Using a Golden-angle Spiral Pulse Sequence. in

ISMRM 2019 (2019).

153. Xue, H. *et al.* Phase-sensitive inversion recovery for myocardial T1 mapping with motion correction and parametric fitting. *Magn. Reson. Med.* **69**, 1408–1420 (2013).

154. Bammer, R., Aksoy, M. & Liu, C. Augmented generalized SENSE reconstruction to correct for rigid body motion. *Magn. Reson. Med.* **57**, 90–102 (2007).

155. Liu, S. *et al.* Diffuse myocardial fibrosis evaluation using cardiac magnetic resonance T1 mapping: sample size considerations for clinical trials. *J. Cardiovasc. Magn. Reson.* **14**, 90 (2012).

156. Jr, A. N. A. *et al.* Myocardial T1 mapping and extracellular volume quantification in patients with left ventricular non-compaction cardiomyopathy. *Eur. Hear. J. - Cardiovasc. Imaging* 1–8 (2018) doi:10.1093/ehjci/jey022.

157. Yarnykh, V. L. Optimal radiofrequency and gradient spoiling for improved accuracy of T1 and B1 measurements using fast steady-state techniques. *Magn. Reson. Med.* **63**, 1610–1626 (2010).

158. Stikov, N. *et al.* On the accuracy of T1 mapping: Searching for common ground. *Magn. Reson. Med.* **73**, 514–522 (2015).

159. Zhou, R. *et al.* Free-breathing continous cine and T1 mapping acquisition using a motion-corrected dual flip angle inversion-recovery spiral technique at 3T. in *ISMRM 2020* (2020).

160. Lesch, A., Schlöegl, M., Holler, M., Bredies, K. & Stollberger, R. Ultrafast 3D Bloch–Siegert B1+-mapping using variational modeling. *Magn. Reson. Med.* **81**, 881–892 (2019).

161. Deoni, S. C. L., Rutt, B. K. & Peters, T. M. Rapid combined T1 and T2 mapping using gradient recalled acquisition in the steady state. *Magn. Reson. Med.* **49**, 515–526 (2003).